UNIVERSITY OF CALGARY

The Fractal Nature of Geologic Structures in Borehole Image Logs and Outcrop

by

Kristoffer William Vickerman

A THESIS

SUBMITTED TO THE FACULTY OF GRADUATE STUDIES

IN PARTIAL FULFILMENT OF THE REQUIREMENTS FOR THE

DEGREE OF MASTER OF SCIENCE

DEPARTMENT OF GEOSCIENCE

CALGARY, ALBERTA

August 2010

Abstract

Borehole image logs from a well in British Columbia are used to draw cross-sections of mesoscopic fold and fault structures and Alberta Rocky Mountains and Foothills outcrop measurements from similar mesoscopic structures are used to generate synthetic borehole image logs. Instead of the simple fractal relationship between fold axis orientations of higher and lower order folds implied in standard presentations of “Pumpelly’s Rule”, mesoscopic structures show variations in structural type and orientation just as megascopic structures do on a scale proportionate to the respective fold’s amplitude and wavelength. Individual mesoscopic fold axis trends have an average difference of +/- 11.2 degrees when compared to the megascopic trend and mesoscopic plunge magnitudes have an average difference of +/- 5.5 degrees. Combining bedding data from a minimum of three mesoscopic structures reduces this difference to +/- 6.1 degrees in trend and +/- 2.1 degrees of plunge.

Acknowledgements

I would like to thank my loving wife, Tona Laerz for her support over the years and her patient labours as my field assistant. I thank my family and friends for encouraging me to finish this project even when I despaired that I would ever be able to complete it. I would also like to thank Talisman Energy Inc. for making it easier for me to use their publicly released borehole image data and last I would like thank my employer, HEF Petrophysical Consulting Inc., for encouraging this research and allowing me the use of their data and workstations. Finally, I give thanks to Dr. Deborah Spratt for the faith to take on a non-geologist working a full-time job as a graduate student, for her patience with how long she had me as a student and for her advice and help in revising the text and figures in this thesis.

Table of Contents

List of Tables

List of Figures and Illustrations

List of Symbols, Abbreviations and Nomenclature

Symbol	Definition
Deg	Degrees
mm	millimetres
cm	centimetres
m	metres
km	kilometres
3-D	Three-dimensional
2-D	Two-dimensional
B.C.	British Columbia
S_1	First eigenvalue of direction cosine matrix
S_2	Second eigenvalue of direction cosine matrix
S_3	Third eigenvalue of direction cosine matrix
MWD	Measurement while drilling

CHAPTER 1: MESOSCOPIC STRUCTURE ANALYSIS

The science of structural geology could be defined as the study of how earth processes produce the geological geometries we see in nature and how to categorize those geometries, while describing a method by which an earth scientist can predict the extent of valuable resources that are found in the earth within structurally deformed rock, and layered or foliated rock in particular. This method always involves taking measurements of one kind or of one scale and interpreting then extrapolating or interpolating those measurements to gain an understanding of the broader geologic picture. These measurements could take the form of a compass and clinometer on a bedding surface on an outcrop, or a seismic reflection event, or an electrical resistivity boundary measured by a well-logging tool that is being pulled up through a wellbore, but there is always some difference between what is being directly measured (a discrete bedding plane inclination or a time-position of a sonic wave-velocity boundary or the sum of an array of electrical resistivity changes) and the desired product, be it a surface map to explain the position of various surface outcroppings, a subsurface map to delineate the possible reserves in a gas field, a drill-target location in a potential oil field on a 2-D seismic line or a refined understanding of exactly what a given wellbore has encountered.

The different methods for measuring structural surfaces have led to a nomenclature to describe the various scales of those measurements. Surface and subsurface structures in a mountain chain or an interpreted seismic line, amounting to hundreds or thousands of metres in extent, are very large in scale and thus are classified as megascopic scale. When working in the megascopic scale, a geologist typically is operating with maps and cross-sections that are compressed at a 1:1000 to 1:50000 scale or more. Fine features such as the trace length of discrete fractures, discrete bedding differentiation, or observing minor structural perturbations is a level of complexity that cannot be included in a megascopic scale interpretation. These smaller features are all contained within (and overprinted by) folds and faults that have amplitudes and displacements measured in tens of metres if not kilometres and are thus are not depicted when working at this scale.

Similarly, features such as a hand sample's precise grain composition or the presence of micron-scale fractures in a thin-section, or the complexity of precisely knowing the open aperture and three dimensional geometry of a fracture network in an outcrop or in a well core is information that is achieved by looking at a much smaller, microscopic, scale. When studying features at the micron to centimetre to decimetre scales, one might describe those features with a granularity that is similar to the scale being studied (i.e. core descriptions are often given to the centimetre if not millimetre-scale). While it may be interesting that a certain measurement was taken from a sample or an outcrop from the side of a vertically dipping bed in the mountains as opposed to an outcropping of horizontal bedding from a prairie river valley, the actual observation of features at the microscopic scale can and often does happen without fully contextualizing the larger scale features in which these observations occur. This lack of context can cause problems when a small feature (such as the presence of a mud bed in a well core) is extrapolated so as to represent a larger scale feature (like a low energy, stagnant water period) when it is possible that the bed in question represents a small feature that is not representative of the larger context (the mud bed in this example could be a rip-up clast that is just larger than the core diameter and was intersected through a form of reverse serendipity).

Any measurement that is taken between the microscopic (up to decimetre) and megascopic (tens of metres or more) scales is in-between sized, called mesoscopic scale. It is in this scale range that the majority of actual structural measurements are taken. At an outcrop, bedding (or fracture) measurements are often done by placing something flat like a clipboard on the surface to give a better “average” measurement in an attempt to eliminate “roughness”, or measurement locales are selected on perfectly planar bedding avoiding zones with local undulations in what are rarely perfectly planar surfaces. A subsurface borehole measurement of bedding is usually taken three or four times every metre from an elliptical intersection trace whose long axis is usually in the decimetre scale. Even seismic reflections occur because of a sonic velocity change in a bed on the order of several (to several tens of) metres and thus the individual trace reflections may be thought of as coming from a mesoscopic scale feature, even though they are summed and studied in the megascopic scale.

The Dale-Pumpelly Principle – a fractal relationship

In their contribution to the Monographs of the United States Geological Survey in 1894 (Pumpelly et al., 1894), Raphael Pumpelly and T. Nelson Dale first introduced the notion that the orientation of higher-order (smaller) folds is generally close to that of lower-order (larger) folds of the same generation. This idea, along with the observation that cleavage/bedding intersection lines, boudin lines and extension fracture/bedding intersections also follow the megascopic structural fold axis, is usually called "Pumpelly's Rule."

It is also interesting that we know this theory as "Pumpelly's Rule", when the observation was made in Dale's section of their United States Geological Survey Monograph, so I prefer to call it the Dale-Pumpelly Principle. This idea has been employed by structural geologists in field research since the early 20th Century because the axial planes and fold hinges of high-order mesoscopic folds can sometimes be easier to measure than those of lower-order megascopic folds. Further, understanding the distribution of mesoscopic folds in a study area can significantly contribute to the understanding of the overall (megascopic) structural setting.

Benoît Mandelbrot coined the term "fractal" in 1975 (Mandelbrot, 1977) and to paraphrase the Merriam-Webster definition, it describes a curve or shape for which any chosen part is similar in shape to a given larger or smaller part. The Dale-Pumpelly Principle describes what today would be called a fractal relationship, where geologic structures of all scales can and do form concurrently and whose geometries, expressed in terms of fold axis trends and plunges, are similar.

This principle has not been statistically tested and quantified in scientific journals to any great degree. This lack of critical examination is itself a reason to study these relationships, but the ultimate goal of this research is to be able to apply this principle to make structural predictions or to further structural understanding that can be used in the process of exploring for oil and gas, using borehole image technology.

In order to investigate the Dale-Pumpelly Principle and to gather more robust data for testing the similarities between mesoscopic structures seen in outcrop and potentially similar structures seen in the subsurface, a rigorous investigation of such structures was undertaken in an outcrop and subsurface borehole image log study. Outcrops were studied at several locations in the Alberta Rocky Mountains and their Foothills in the summer of 2007 (see Chapter 3).

Borehole image logs

Borehole image logging is a down-hole wireline measurement of very fine changes in the petrophysical characteristics of the rock (such as microresistivity, density, natural gamma ray emissions or sonic reflectivity). It uses those changes in physical properties, along with a measurement of the wellbore deviation and the tool's orientation, to determine the true dip of the intersected bedding, fractures and other features (Schlumberger, 1986). Since a geological bed can be thought of as an approximate plane, that plane will intersect a cylindrical borehole at different depths around the borehole's circumference if the bed is not horizontal, resulting in a sinusoidal trace if the borehole's surface were to be unrolled. A dipmeter or borehole image log's pads (or measurement field) reach out to the borehole wall to measure the different depths of intersection of those resistivity changes and from those different depths of intersection, the bedding dip may be calculated.

Since the first dipmeter log was recorded in the 1930's by Schlumberger, the technology has advanced significantly. Now, instead of a single resistivity measurement on each of three pads as was recorded in the 1930's, there are arrays of dozens of resistivity buttons measured on four, six or eight pads that go by a number of trade names depending on the logging company that produces them. These arrays of resistivity (or other physical measurements) are then converted into a synthetic colour "image" of the cylinder of the borehole, as seen from the inside, unrolled into a plane. These borehole images are shown with interpreted bedding and fracture sinusoids over the 0-360 degree range of azimuth as well as a tadpole representation of the dip measurement.

Further advancements in borehole imaging technology have lead to the development of acoustic imaging tools. These use ultrasonic pulses that are sent out in a 360 degree arc through the drilling mud and are reflected back by the different strata on the borehole wall. These acoustic imagers have an advantage in that they do not require an electrically conductive water based mud like standard resistivity image logs do, but they have several problems, not the least of which is that their vertical resolution is poorer (a result of the time needed to send and receive discrete sonic pulses through the borehole fluid) (Cheung, 1999). The biggest problem with acoustic imaging tools is that there often is insufficient contrast in the return signal amplitude to distinguish different beds or fractures. Further, these tools are very sensitive to the condition of the borehole wall (because the reflection dispersion from an uneven surface overwhelms the subtle differences in sonic reflection amplitude of bedding and fractures). They are also sensitive to the presence of mud filtrate cake, which is a viscous material that forms on the borehole wall when drilling mud is pressed into permeable formations, filtering out solids that were suspended in the drilling mud. The mud cake then reflects the sonic signal, masking the bedding, sedimentary textures and fractures that are clearly measured in electrical images.

Until recent years, the only borehole imaging option available in oil based mud systems was to use an acoustic imaging tool with or without a dipmeter equipped with scraping blades. This option works well for many applications, with the data from the dipmeter used for structural dip and the acoustic images used primarily for fracture determination, to refine the structural interpretation and to measure the borehole breakout direction to determine the wellbore stress field orientations. In the last ten years, several different logging companies have developed oil-based resistivity imaging tools with multiple buttons on each pad capable of operating in oil-based environments as well as measurement while drilling (MWD) density, gamma-ray and resistivity imaging tools (Weller et al., 2005). These tools have added another option for data acquisition but they are not without their own problems. Oil based electrical image logs are very sensitive to roughness in the borehole wall and to drilling mud salinity because the electric signal from the image tool is lost whenever there is poor contact between the pads and the formation. MWD tools tend to be coarse in resolution and require the bit to be spinning, which is not always the case.

Figure 1-1 is a block diagram of a borehole image tool in action, the resulting appearance of a schematic image log derived from that block diagram and an example resistivity image log from a natural gas well in northeast British Columbia, Canada.

In the image log example shown here, and in all subsequent real borehole image logs, the resistivity response has been mapped to a colour scale where the lighter yellows and whites are zones that are electrically resistive and the darker browns and blacks are electrically conductive. This measurement is very shallow (less than 1 cm from the tool)

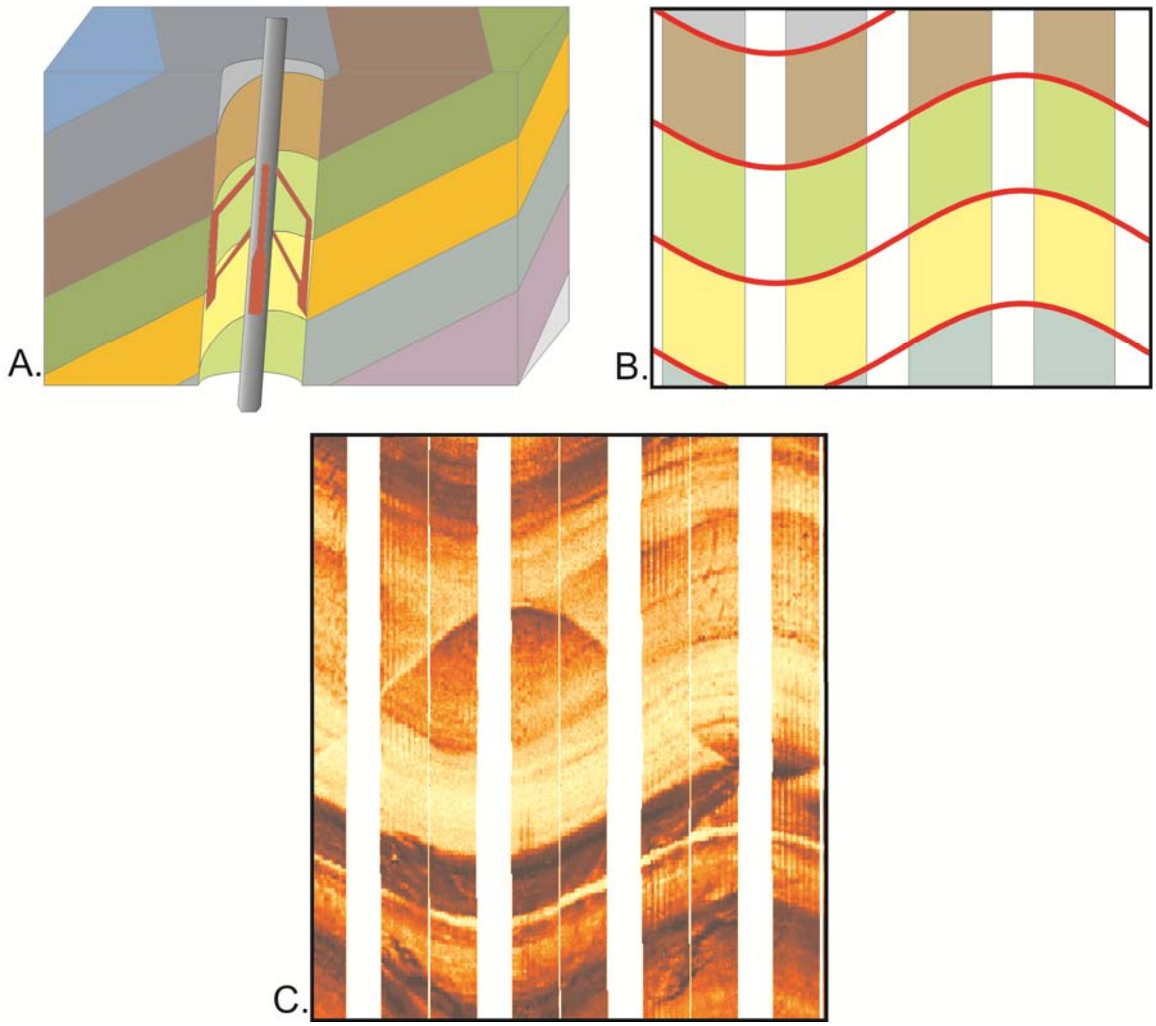

Figure 1-1: Borehole image log acquisition block diagram and example
The top left image (A) is a block diagram of a 4-pad borehole image logging tool as it intersects inclined bedding. Image B shows how those bedding planes would look in an unrolled (sinusoidal) image log and image C shows an interval from a real resistivity image log showing the typical light yellow to black colour palette (corresponding to high and low resistivity, respectively).

thus it is entirely contained within the drilling mud-invaded zone. This means that while open aperture features such as fractures, vugs or intergranular porosity may once have contained a resistive fluid like oil or gas, that fluid is washed away in the drilling process and replaced by conductive drilling mud, making those features dark on resistivity image logs.

Borehole images in petroleum exploration

The reality of modern petroleum exploration in complex structures is that while seismic surveys are useful in finding exploration targets, the fold limbs and faults are often much too steep, too fine, or are too complicated to resolve. Often, wells are drilled that target a certain reservoir unit that looks to be in an uplifted and therefore favourable position without knowing the vergence of (sense of shear direction on) the faults or folds that led to the uplifted position. Seismic velocity anisotropy (as well as stress-induced anisotropy) causes features to be imaged in an incorrect lateral position or at the wrong depth because of inaccurate depth migration. These errors are unavoidable because petroleum exploration always requires one well to be the first drilled into a certain potential target before sonic velocities can be obtained for depth migration and before knowing for certain whether a given reflector is what it is expected (or hoped) to be. This leads to wells being drilled to what seems to be the best structural position available when those structures may be very different from what the seismic image implies.

The current industry use of borehole image and dipmeter logs is to constrain the averaged orientations of bedding and fractures, with the goal of determining a number of things:

the true dip of fold limbs on a megascopic scale; the location of fold hinges; the orientation and location of faults; the location, aperture and orientation of open and mineral-filled fractures; the local fold plunge for planning horizontal wells (usually in a crestal or back-limb position, parallel to the fold hinge); and a number of fine sedimentary textures such as interbedding patterns, suspended clasts, bioturbation, ripples and fine crossbedding. Currently, useful outcrop-scale features such as mesoscopic folds, bedding/cleavage intersections, extension fracture/bedding intersections and centimetre-scale faults are visible in many foothills borehole images but these important clues for structural understanding are ignored while features of a similar scale are studied by sedimentologists in image logs acquired in the Canadian Oil Sands, perhaps because sedimentologists are used to working with tiny features like trace fossils or thin soil horizons in their interpretations.

This is a bypassed opportunity to better understand subsurface structures, thus a method needs to be developed to resolve these features. Then, if the statistical relationship between these mesoscopic features and the megascopic structures in which they are contained were understood, one could make predictions based on one or a handful of these features that could guide further development of a given well or reservoir. Another part of my interest in looking at mesoscopic structures in general is to relate those structures that are observed in outcrop and to better understand how they would look in the subsurface if they were observed by borehole imaging logs. By making comparisons between features measured in the field and those observed in a borehole image log, an image log interpreter can do a better job of understanding and explaining the complex features that are sometimes seen in these logs. This is done by converting outcrop measurements to imaginary borehole images and by converting real borehole image data to correctly scaled cross-sections, then comparing the two.

Method for measuring mesoscopic structures in outcrop

The first half of this study involved taking careful measurements of a variety of mesoscopic structures in outcrop. Measuring mesoscopic structures in geologic outcrops presents challenges that are not present when making standard outcrop measurements for the purpose of formation mapping and for drawing megascopic cross-sections, where a geologist can carefully select the best bed outcroppings of the most planar beds to do their mapping from. The first difficulty is in taking the measurements themselves. Mesoscopic structures are often fissile and have bedding plane curvatures that can make it difficult to position a compass accurately on them. To try to mitigate these problems, most of the measurements in this study were taken by placing a planar, non-magnetic plastic board on the measured bed or fault surface. This reduced the scatter of repeated measurements of the same feature greatly as it represented a somewhat larger average sample and allowed measurements where only a small crack of the bedding plane was present by jamming the board into a bedding plane-parallel crack.

The greatest challenge was in recording the three-dimensional (3-D) position of each measurement accurately enough to draw a mesoscopic cross-section that may only be a couple of metres on a side. At this scale, the position of the dip and strike measurement points needed to be known to within a centimetre or two in order to have a positional error bar of less than 2%. To accomplish this level of precision, each measurement point's location was carefully calculated relative to a number of known reference frames. These references included a rectangular grid apparatus that my wife and I built out of rigid PVC drain pipe with nylon cording stretched into a 20 cm grid. The apparatus was then positioned next to the outcrop and the centre of each bedding measurement was recorded relative to the nylon cord grid within an accuracy of +/- 1 cm. Finally, I measured the orientation of the grid plane itself as well as the rake of the cord lines on that plane so that each dip and strike measurement's 3-D orientation could be calculated later.

This method worked well for those structures that were easily accessible with a flat base to the outcrop such as the minor folds near Cascade Mountain and near Elbow Falls (see Chapter 2). At those two sites, photographs were taken of the structure with and without the grid in place and the dip and dip direction measurements were then taken and their locations were recorded with respect to their position within the grid.
Unfortunately, the Grid apparatus was only directly usable in those two outcrop locations. The other two were either too steep, in the case of the Powderface Trail structure, or were on too large a scale, as in the case of the Canmore outcrop (See Chapter 2). Since the goals are the same, the positioning of each measurement was still carefully recorded using methods appropriate to each location. For the Powderface Trail outcrop, a measuring tape was strung out separately for both folds in two straight lines (whose trends and plunges were measured) and each dip and dip direction measurement was recorded relative to that measuring tape and then computed to get a location in 3-D space.

This method, when combined with the difficult condition of the outcrop, led to some error in the positioning (on the order of +/- 2 cm). To minimize the error, the measurements were taken close to the measuring tape and thus are located more or less on a single line that crossed the folds.

The Canmore outcrop is in fantastic condition, has excellent access and is a fine example of a good variety of the types of structures that are the topic of this study. It is of such a scale that I decided to position my measurements by noting where each surface I was measuring was on a foldout digital photograph montage. This montage was taken from across the road in a preliminary outing to the outcrop and was compared to a second montage taken with rocks placed conspicuously on the sidewalk at a 2 metre interval, so as to provide an absolute scale so that the effects of parallax could be removed and a more accurate position could be obtained. This led to a positional accuracy on the range of approximately +/- 4 cm in the plane of the outcrop.

The measured exposures were all cliff faces of some sort and relatively planar, so I conducted a measurement of the strike and dip of the cliff faces so as to be able to compute 3-D positions for each of the measurements by comparing back to the reference grid, line or photograph. This amounts to another approximation of position but since the inclinations of each slope were relatively planar and close to vertical, it results in an error on the decimetre scale in and out of the plane of the structure, which is unavoidable and, given the fact that the measured structures were in road cuts that were close to dip sections, the errors were mostly parallel to the projection direction and the projection distances to the cross-section planes are relatively small. In the case of the measurements taken from the grid, the grid plane's dip and strike were measured and the grid was positioned such that the measurement distance between it and the rock face was kept to a minimum.

Each outcrop was divided into logical structural domains (where there was more than one measurable mesoscopic feature), typically centered on a single anticline or syncline. The dip data from each domain were then loaded into the program Lithotect, where each domain's fold axis was determined. These dip data were projected down-plunge onto a plane perpendicular to the fold axis and a line drawing cross-section was constructed in CorelDraw by interpreting dip isogons (shapes that enclose an area of equal dip bounded by faults or fold hinge traces), and subsequently interpreting bed shapes. This was done in CorelDraw because the features were too complicated for any more automated projection programs like that contained within Lithotect itself. The cross-sections could not be balanced in a classical sense because they were usually bounded by ductile, fissile shale or coal beds that tended to be effectively plastically deformed to accommodate compression in the more competent strata. Further, there were several instances where the measurements from a single deformed bed did not project well when compared to parallel beds (due to different plunge measurements in the bedding near to and far away from the core of the folds. In these instances, a judgement call was made and fold structural elements were inferred or the interpretation was smoothed somewhat to accommodate the incongruous measurements). This kind of compromise is pretty common in structural interpretations at the megascopic scale, so because the ultimate goal was to gain a representative line drawing, I felt that it was appropriate at the mesoscopic scale as well.

Converting outcrop measurements to synthetic borehole images

To better understand how mesoscopic structures would appear when observed by a borehole image log, I took the line-drawing cross-sections and intersected those structures from different angles with imaginary cylindrical boreholes that are parallel to the plane of section. Then, I took those imaginary boreholes and determined how the bedding would intersect the cylinder and then unrolled the imaginary cylinder to make a synthetic borehole image log. The goal was to build a set of examples so that the complex sorts of structures that are seen in subsurface logs could be referenced through analogy and thus we can understand what types and what scales of structures can be measured accurately in image logs.

I created a novel procedure to transform a cross-section into a synthetic-borehole image log. This method is fairly simple in its constituent steps but looks difficult when one just looks at the final result (Compare Figure 1-2, Step A to Step D). The steps are laid out in Figures 1-2 through 1-4, steps A through S, below. All the transformations in these steps were done in CorelDraw because it readily allows for known rotations, extensions, and deformations in vertical and horizontal axes, but this could be done in any vector drawing software or (if one were masochistic) could be done by hand.

In Figure 1-2 Step A we can see a line drawing of a simple kink fold (bedding is marked in orange, the fold hinge planes (kink planes) are dashed black and the imaginary

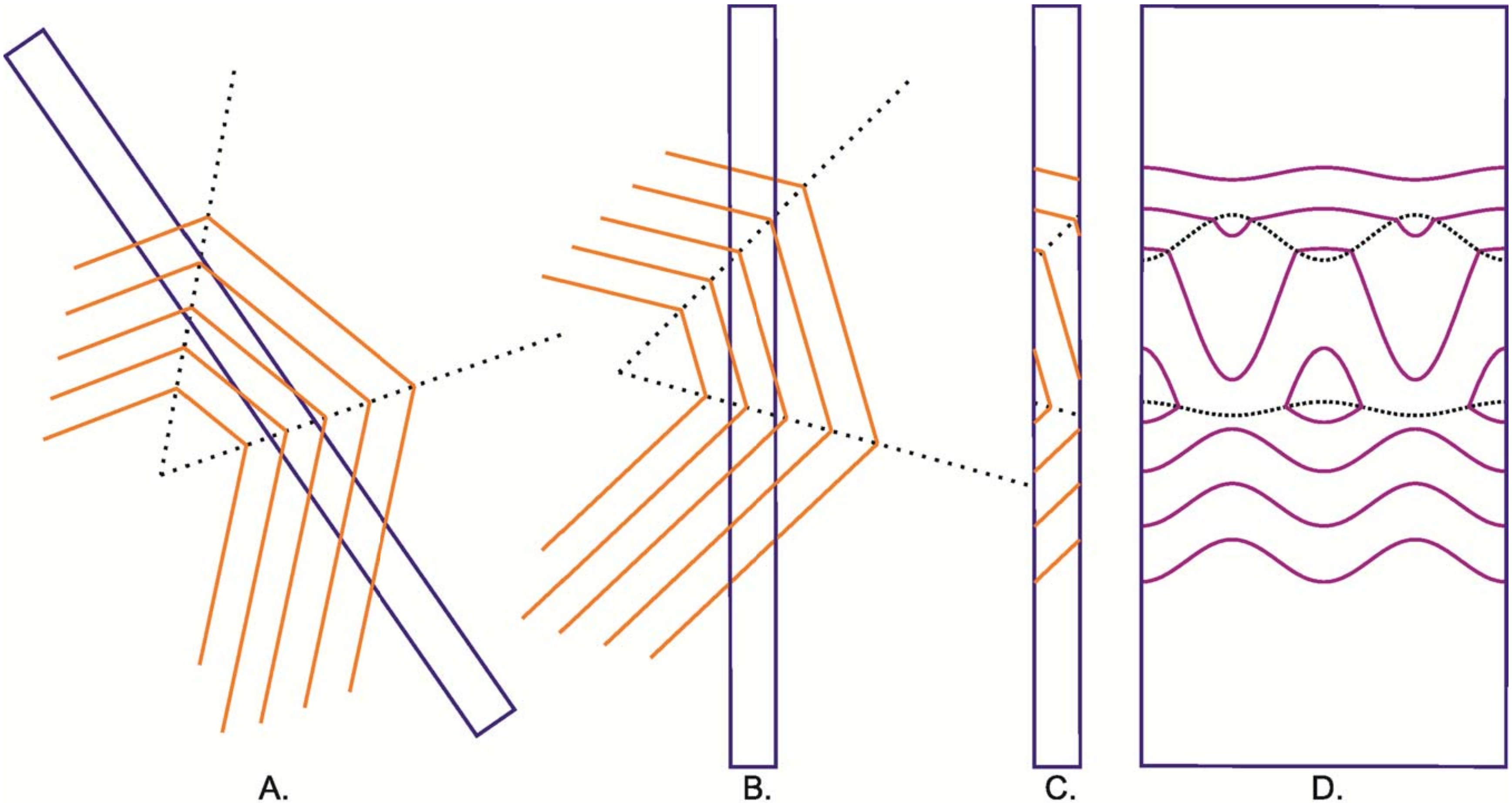

Figure 1-2: Converting outcrop measurements to a synthetic borehole image
Step A shows an imaginary wellbore (blue rectangle) intersecting a fold (beds in orange, hinge planes dotted black). Step B shows that same image rotated so that the borehole is vertical. Step C shows the extra features trimmed back. Step D shows the resulting synthetic borehole image log, which has its bedding sinusoids marked in purple and fold hinges in dotted black.

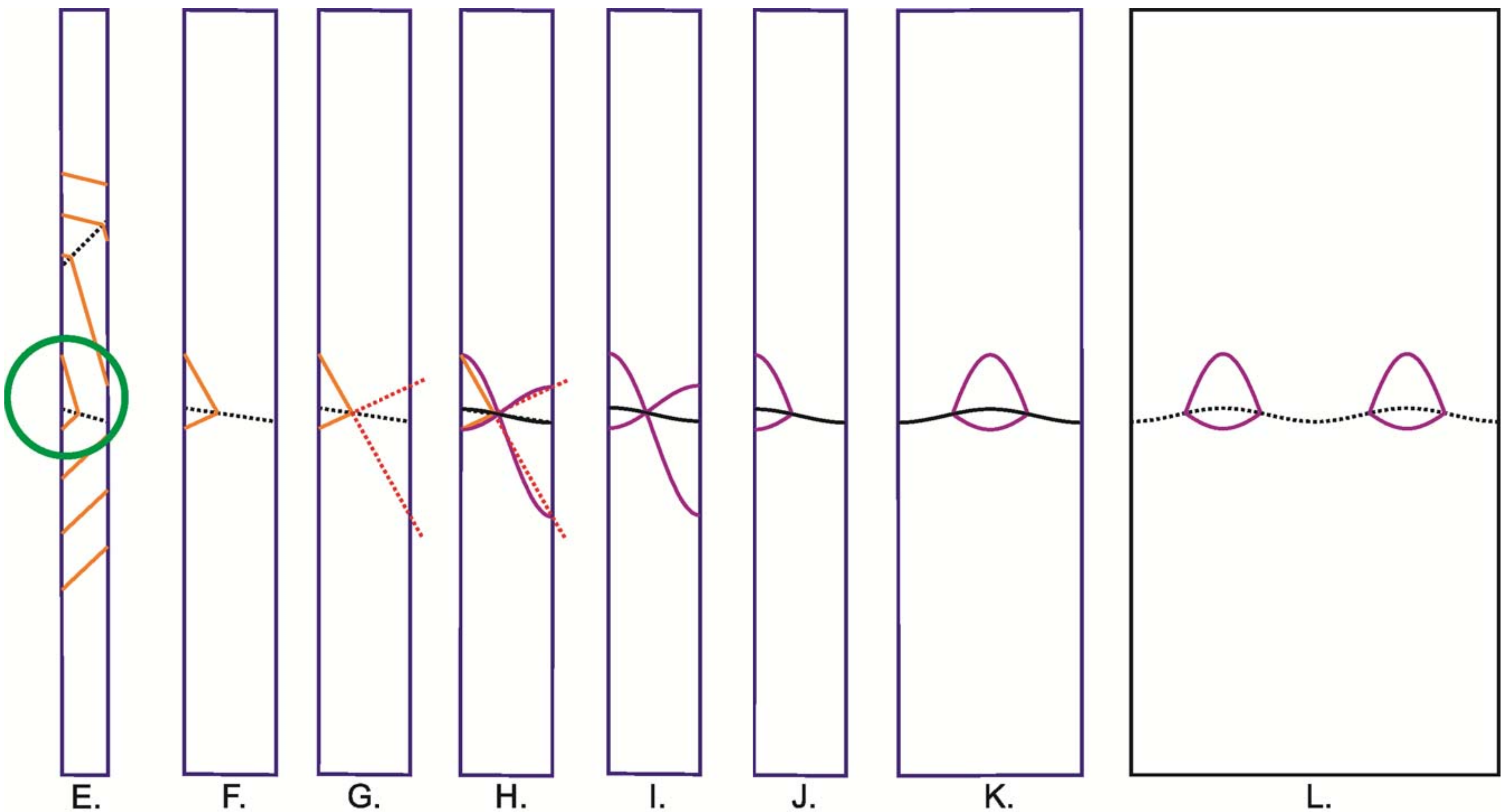

Figure 1-3: Converting outcrop measurements to a synthetic borehole image (expanded procedure)
The encircled features (step E) are isolated to simplify the transformation. The horizontal scale is expanded (F), the lines are extended to the edge of the borehole (G), the solid purple and black half sinusoids that correspond to the features are overlain (H). The sinusoids are shown without the projection lines (I), they are then trimmed back (J) – leaving the sinusoidal version of Step F. The half sinusoids are mirrored to yield a full sinusoid (K) and repeated for the final double sinusoid image (L).

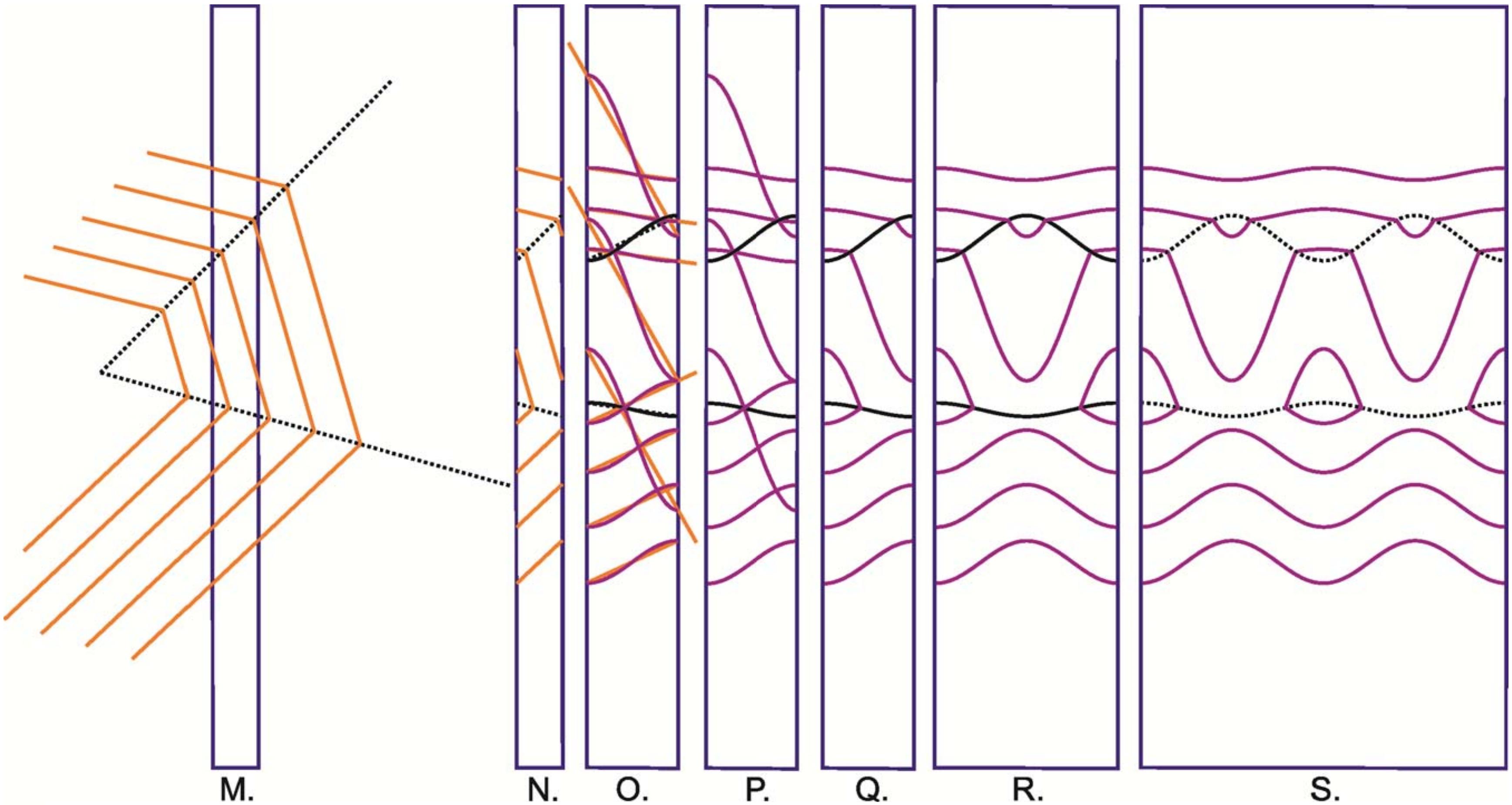

Figure 1-4: Converting outcrop measurements to a synthetic borehole image (full example)
Repeating the process from Figure 1-2 and 1-3, the cross-section is rotated so the borehole is vertical (M), the extraneous features are cropped back (N), features are projected and corresponding half sinusoids are added (O), the cross-section lines are removed (P), the extra portion of the sinusoids are trimmed back (Q), they are mirrored (R) and doubled to make a double sinusoid (S). To make the bedding and faults clearer, the hinge planes are shown dotted in the final synthetic borehole image.

wellbore intersection is shown as a dark blue rectangle whose orientation has been chosen arbitrarily). In step B, the line drawing is rotated such that the wellbore is vertical and thus would be positioned in log measured depth reference space like a borehole image log would be. In step C, the bedding and hinge lines are trimmed back to where they would intersect the edge of the borehole. Step D shows the final image as it would be displayed in the real outcrop to synthetic borehole translation in Chapter 2.

In Figure 1-3 Step E a small portion of the cross-section data (a folded bed that does not cross the entire wellbore and the fold's hinge plane) is circled to isolate the method on a simple part of the structure before repeating the steps to complete the process. Step F shows just the isolated feature, with the horizontal axis expanded to make it easier to see. This distortion does not affect the final synthetic borehole image because the horizontal axis on a borehole image is a display of 360 degrees of circumference and it is not customary to use a precise angle-to-circumference scale for image log presentations. In step G, the bedding lines (and any other lines in the drawing such as faults, fractures or hinge planes) are extended so that they intersect both sides of the imaginary borehole. This is done so that in Step H we can place a half sinusoid on the drawing so that the peak and trough of the sinusoid segment correspond to the projected or observed intersection points. Step I shows those half sinusoids without the cross-section guide lines and Step J shows those sinusoid portions trimmed back so that the projected parts that corresponded to the extensions in Step H are gone. Step J is now half of an unrolled (sinusoidal) borehole view of that fold feature. In Step K that feature is copied and inverted (mirrored) along a vertical edge to produce a single 0-360 degree synthetic-borehole image and in Step L, the image is copied again to produce the double image that will be presented in subsequent chapters in order to make it easier to see the planes of symmetry.

In Figure 1-4 this process is repeated for all of the features in the example cross-section. Step M is the full measured-depth rotated line drawing; Step N shows the trimmed lines as they intersect the imaginary wellbore; Step O shows the extended bedding (etc.) planes with their corresponding half sinusoids; Step P shows the half sinusoids without the extended bedding, fault and fold hinge lines; Step Q shows the half-sinusoids after they have been trimmed back as appropriate; Step R shows Step Q's image mirrored and copied and Step S shows the final doubled synthetic borehole image log. For all the cross-sections in Chapter 2, only the overlain imaginary wellbores (Step A), the trimmed back and rotated wellbores (Step C) and the final synthetic logs (Step D in Figure 1-2) are shown because there was no need to vary this procedure and thus no need to reproduce every step repeatedly.

There is one significant approximation embedded in this method. The cross-section is assumed to be on a correctly selected right-section plane (the true profile of a cylindrical structure on a plane perpendicular to the fold axis, as viewed parallel to the generatrix) so that there is little enough dip into or out of the section that it can be assumed to be zero (i.e. the structure is reasonably cylindrical and all the features are contained within that one plane). If the out-of-plane dip is significant, then the imaginary borehole intersection points will not be at the apexes of the half sinusoids but will intersect on either side of the peak or trough of the sinusoid. The resulting synthetic borehole images would not have a single plane of symmetry as the rotational azimuths of the sinusoids would shift from side to side as the dip ratio (the variance from the dip section) changes. There is an example of a feature of this sort among the real borehole image log examples (see Chapter 3), where the fold feature changes on opposite sides of the wellbore.

The second approximation is that all the boreholes are drawn such that they are parallel to (in) the right-section plane but I will show that this approximation is not particularly significant. Once we accept the first approximation (the structure is reasonably cylindrical and the projection plane is correctly chosen), a borehole drawn parallel to the projection plane will intersect the same features in the same order as one that has the same apparent dip on the projection plane but that goes into or out of the plane of section. The intersections will merely be stretched over a longer measured depth and thus while they would have steeper apparent intersection angles (and longer sinusoids), the shape of the borehole image log would be closely related. I have tried to illustrate this principle in Figure 1-5, which shows an isometric drawing of a simple dipping bedding plane intersected by a borehole (the vertical cylinder on the left) parallel to the right-section plane and a second borehole (the inclined cylinder on the right) that intersects that bedding plane at an oblique angle out of the plane of the cross-section. One could imagine for instance that if the boreholes were cut by a fault plane striking parallel to bedding, the resultant truncated bedding plane would be observed by both boreholes as half-ellipses (and half-sinusoids in an unrolled borehole view), just at different depths and different apparent dips. A depiction of how the example image from Figure 1-2

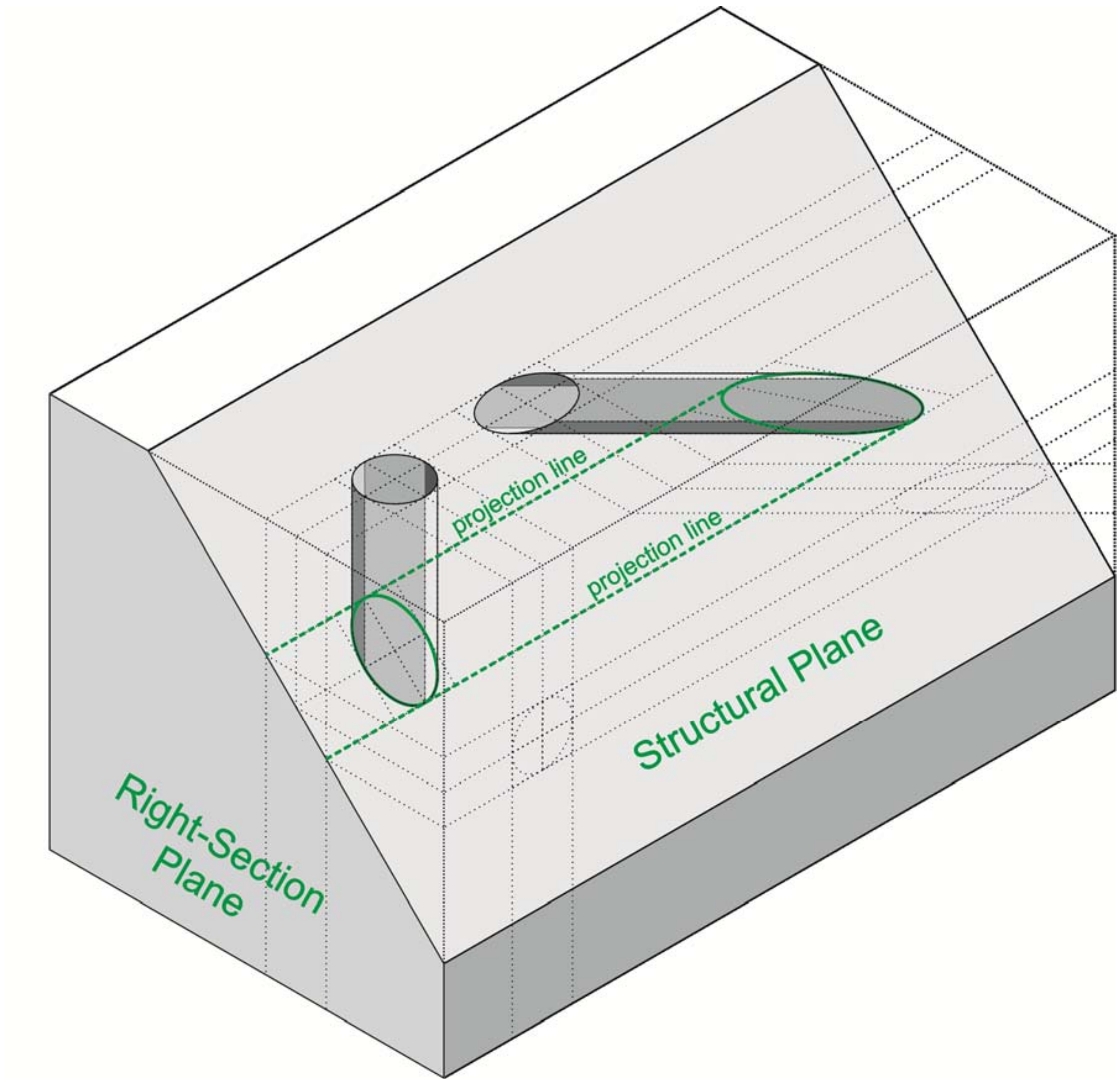

Figure 1-5: Projecting boreholes out of the structural plane
This isometric drawing shows a simple dipping bedding plane intersected by a borehole (the vertical cylinder on the left) that is parallel to the right-section plane. The second borehole (the inclined cylinder on the right) would project onto the right-section plane identically to the first borehole but it is inclined at an oblique angle out of the plane of the cross-section. The point of this diagram is to show that a cylinder that is parallel to the cross-section plane intersects the same features as the inclined one, just with a smaller intersection ellipse (highlighted in green on both cylinders) and thus a smaller apparent dip on the well log. One could imagine that if the boreholes were cut by a vertical fault plane striking parallel to bedding, the resultant truncated bedding plane would be observed by both boreholes as half-ellipses (and half-sinusoids in an unrolled borehole view), just at different depths and different apparent dips.

would be distorted by increasing the angle between the borehole and the right-section plane is shown in Figure 1-6. Now, because the rotational position of the original borehole (i.e. its apparent dip in the projection plane) is arbitrary and there is no significant difference (other than a stretching of scale) between an in-plane borehole and any of its corresponding out-of-plane cohorts, this method works for a borehole of any orientation.

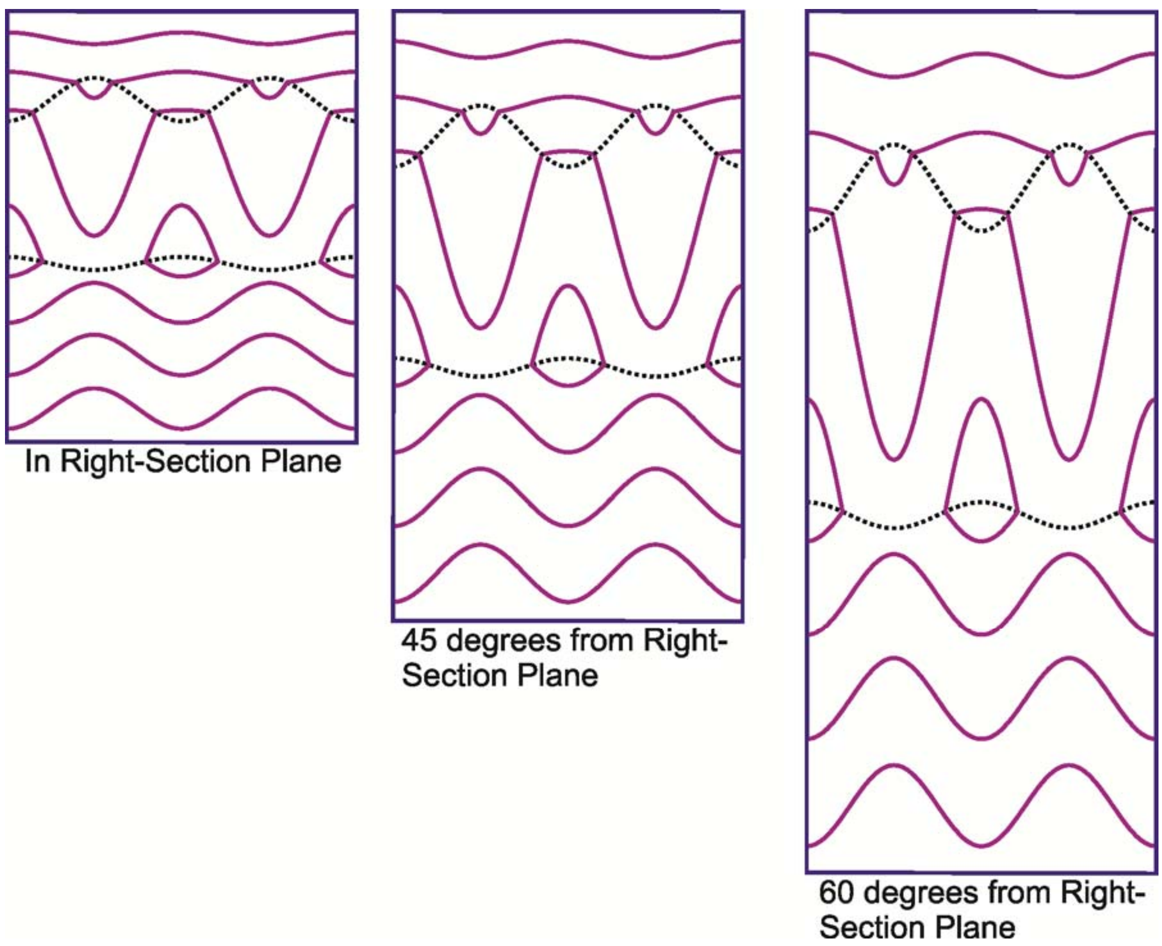

Figure 1-6: In-plane versus out-of-plane synthetic-borehole image logs
The example image from Figure 1-2 would be progressively stretched by increasing the angle between the borehole and the right-section plane. Since the changes between these synthetic borehole image logs are the result of a uniaxial distortion that is trivial to undo, they are not significant and thus this method is universally applicable.

Measuring mesoscopic structures in subsurface borehole image logs

While all of the measurements taken in borehole image logs are mesoscopic in scale, the usual goal is to understand the overall (megascopic) structural picture. This means that finely measuring the bedding in small-scale structures introduces undesired complexity in the output structural data (raw measurement values as well as presentations like wellbore cross-sections and other summary plots). Thus, smaller structural features are treated as curiosities to be summed up by notations that mark them as “Shear Features” and the bedding orientations of minor structural or stratigraphic perturbations are not measured as a matter of course. Data are instead entered into vector averaging or stereonet programs or other displays like dip azimuth scatter curvature plots to obtain what is considered to be the “significant” dip measurements, i.e. the megascopic dip trend.

The procedure for measuring mesoscopic structures is not particularly difficult when compared to standard borehole image log interpretation. Standard borehole image interpretation is done by using software programs to fit sinusoidal traces to the predominantly planar features that are common in these logs such as fractures or bedding. The interpretation software takes the known borehole orientation, caliper measurements, and sinusoid position, apparent dip and rotational azimuth and calculates a true dip and dip azimuth for each interpreted event. The process is similar for measuring mesoscopic structures except that the measured features are not planar and can be observed to bend within the area of the wellbore. Typically, mesoscopic structures have lateral extents in the axial direction that are wider than the cylinder of the borehole (i.e. the fold plunges do not change rapidly enough to be visible in wellbores that are between 10 and 50 cm in diameter). This means that they will be observed twice in each borehole image log and there will be a plane of symmetry in the bedding features. By using this plane of symmetry, one can fit sinusoidal trace segments along a curved surface to approximate the curve as a series of short planes.

Drawing to-scale cross-sections using complex borehole image data

The previously described method for converting outcrop measurements to synthetic borehole image logs can be inverted to convert a borehole image log into a cross-sectional line-drawing either parallel to the wellbore in the apparent dip direction or in a right-section plane. This process is shown in Figures 1-7 and 1-8, steps A through G.

Figure 1-7 Step A shows a 5 metre interval from an uninterpreted electrical borehole image from the case study well (Talisman et al. Bullmoose D-77-D/93-P-3). In this interval, the borehole intersects both limbs and the nearly flat (apparent dip) hinge of an uncomplicated open fold. Beds are seen to bend in and out of the image between 4671.5 and 4673.5 metres, forming a distorted circle where the beds do not extend across the entire borehole. In step B, the image is overlain by a number of green double sinusoids. These sinusoids are placed at the clearest contrast boundaries between high and low resistivity bedding planes. Because the features are not all planar (and thus do not represent full sinusoids in the borehole image), a single folded bedding plane may be intersected by several of these sinusoids, each representing a segment of the bedding dip. Also on step B, there are two dark coloured vertical lines that pass approximately through the peaks and troughs of the interpreted bedding sinusoids. These lines are drawn exactly

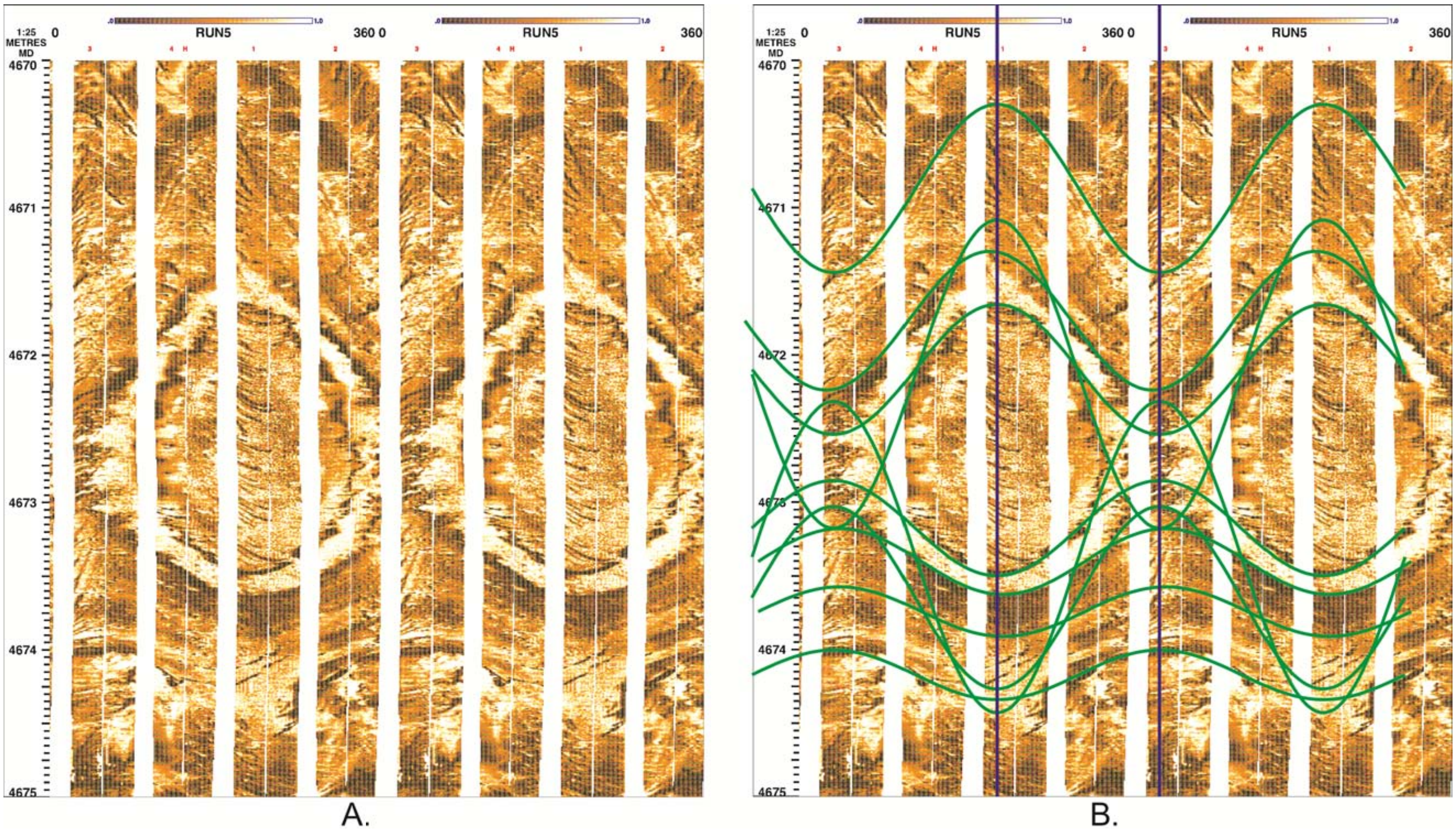

Figure 1-7: Converting complex borehole image log measurements to a cross-sectional view (part 1)
Step A shows a borehole image log from the Case Study Well for an interval with a simple fold whose limbs cut through the borehole. Step B shows that image superimposed with green double sinusoids that are aligned to represent the interpreted bedding segments. A pair of dark blue lines are drawn through the sinusoids' apexes 180° apart representing the cross-section plane.

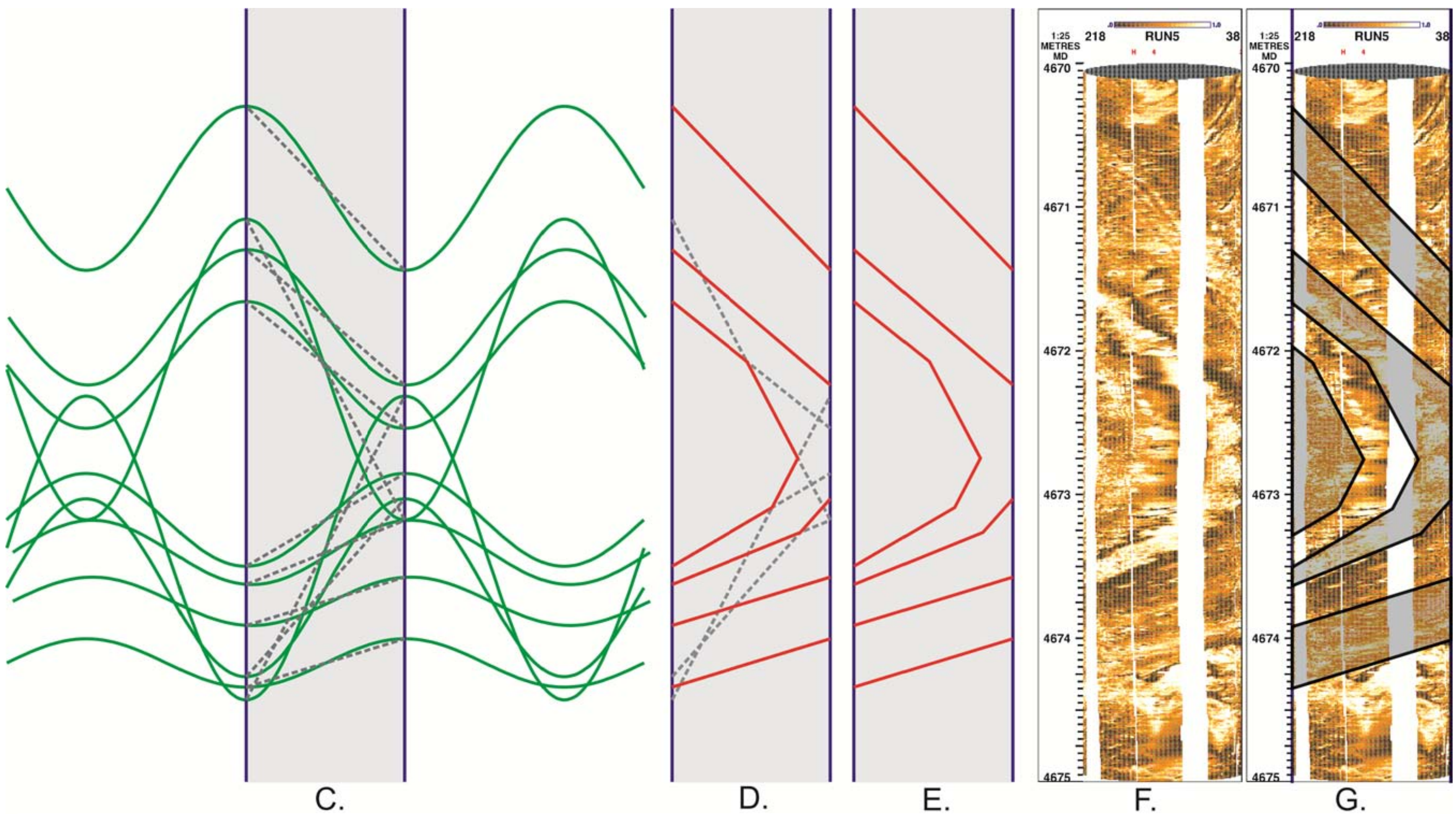

Figure 1-8: Converting complex borehole image log measurements to a cross-sectional view (part 2)
Step C shows the image log removed and dashed grey lines connecting the sinusoid-borehole intersections. Step D shows the portion that corresponds to the interpreted bedding segments highlighted in red. Step E is the final cross-sectional version of the interpreted bedding. Steps F and G are a side-on view of the borehole image log with the final cross-section for comparison.

180 degrees apart (half the width of a single full sinusoid and thus one quarter of the presented double image width) and represent the intersection lines for a borehole-parallel plane of section that the measured features will be projected onto. For the images in Chapter 3, only the relevant portions of the original sinusoids are shown with the portions that do not land on a bedding surface being trimmed away.

Figure 1-8 Step C shows the sinusoids and the intersection lines from Figure 1-7 Step B without the borehole image. The interval between the intersection lines has been shaded light grey, representing the plane of section, while the points of intersection between the sinusoids and the edge of the grey box are connected by straight dashed lines. These lines connect the highest and lowest points where the sinusoid features intersect the wellbore and thus can be mapped as a bedding plane in the eventual cross-section. If all of the features in the image were to be exactly in the same structural plane (i.e. the structure is perfectly cylindrical and the projection plane is correctly oriented), there would be a single plane of section that would pass exactly through the peaks and troughs of the sinusoids. It is difficult to see, but in the example the sinusoids are not exactly bisected by the plane of section. Still, there is no need to do any geometric correction because the dashed lines connecting the intersection points (rather than the sinusoids' apexes) correspond to the apparent dip line in the plane of section. This becomes obvious because if the pair of 180 degree lines were drawn through the peak and trough, they would give the true dip (maximum apparent dip) and if it were instead drawn through the inflection points, they would result in flat dip (minimum apparent dip), and all the intermediate bedding heights are governed by a sine wave. Step D has the sinusoids removed and the segments of the dashed apparent dip lines that correspond to the folded bedding have been traced in a solid red colour. Step E shows the final bedding cross-section without these guide lines. As with any cross-section, the bedding planes can be interpolated, projected and extended away from the primary measurement (using dip isogons for instance) so as to give a fuller picture of the structure. This kind of interpolation and extrapolation is done in the case study images where the structures are not mostly contained within the cylinder of the borehole.

For comparison, Step F (Figure 1-8) shows a cylindrical side-on view of the image data rotated into the plane of section and shown from the same side as the cross-section. Step G shows how that image corresponds very well when overlain by shaded shapes generated from the interpolated cross-section from Step E.

Once the borehole-parallel cross-section is generated, it should be resized so that the horizontal axis (which represents the diameter of the wellbore, a known dimension) is at the same scale as the vertical axis (which is also known from the image log's measured depth on the left of the borehole image log). This will correct any distortions in the dip lines so that they truly represent the orientations of those features in the plane of section. This step is done for all of the section drawings generated from borehole images in Chapter 3.

If one wanted to view the cross-section in the right-section plane rather than in a plane that is parallel to that segment of borehole in the apparent dip direction, the geometric conversion is simple. Keeping the horizontal axis unchanged (as it is already parallel to the right-section plane because it is through the best-fit peaks and troughs of the sinusoids – i.e. through their “true dips”), just compress the vertical axis by multiplying it by $\cos\Theta$ where Θ equals the minimum angle between the wellbore segment and the right-section plane and rotate it by the apparent wellbore deviation in that projection plane.

Rotating the wellbore cross-sections into the right-section plane may be useful for some applications where one needs to know the precise geometry to measure contorted bed thicknesses (perhaps in a mining setting) but the focus of this study is in the scales and types of structures that can be observed by borehole image logs and because all of the distortions are linear along the vertical axis before rotation, this final step was not done for the measurements in Chapter 3.

Statistical analysis of mesoscopic data

In the following chapters, individual mesoscopic structures’ bedding and fault plane orientations have been measured with the goal of comparing their calculated fold axis orientations (using direction cosine matrix eigenvectors) to their associated megascopic fold axes. Mesoscopic structures by their nature are difficult to measure and thus it is rare that a single minor fold will have enough measurable bedding surfaces to exceed the rule of thumb that says that one needs thirty bedding measurements ($n = 30$) to obtain a significant data set. This fact cannot be avoided if one wants to study these structures, nor would a “significant” result be reasonably obtained by repeating measurements on the same surfaces just to exceed $n = 30$ measurements. Having smaller sample numbers does not mean that statistical comparisons should not be made, just that they should be done with a certain amount of caution.

The first step in attempting to understand the statistical relationship between mesoscopic and megascopic structures should include an investigation into whether the individual structure's bedding pole data plots as a cylindrical girdle (i.e. similar in shape to a great circle) or as a cluster. There are two fairly simple tests for structural data described by Woodcock and Naylor (1983) that involve comparing the ratios of the direction cosine matrix eigenvalues (S_1, S_2, and S_3).

The first test parameter is the "Shape Parameter" K [where $K = \ln(S_1/S_2)/\ln(S_2/S_3)$], which describes whether the orientation data set is a cluster or a girdle. K ranges in value from zero (for uniaxial girdles) to infinite (for uniaxial clusters), with values $K < 1$ being girdles and $K > 1$ being clusters.

The second test parameter is the "Strength Parameter" C [where $C = \ln(S_1/ S_3)$], which describes the tightness of the girdle or cluster. C ranges in value from zero (for uniformly distributed random orientations) to infinite for perfect girdles or single point clusters, with values $C < 3$ being weak (scattered) and $C > 3$ being strong (tight).

In addition to quantifying the shape of the orientation data, it is prudent to group individual mesoscopic structure measurements together to test whether groups of structures follow the Dale-Pumpelly Principle better than individual mesoscopic structures. For the outcrop locations where there are two or more structural domains measured, all of the domains will be grouped together for a single bedding pole stereonet display and a fold axis calculation. For the subsurface borehole image log data (where $n = 12$ on average for each individual structure), those individual structures will be grouped into groups of three consecutive measurement intervals (or in smaller groups where the groups contain multiple sets of folds) for an aggregate stereonet display and fold axis calculation, such that $n > 30$.

CHAPTER 2: MESOSCOPIC STRUCTURES IN OUTCROP

Four field locations were chosen in the Alberta Rocky Mountains and Foothills that allow easy access to a variety of exposed mesoscopic structures for study.

Case Study 1: Elbow Falls

The outcrop is of fine grained, finely laminated Jurassic sandstones and shales of the Fernie Formation that are structurally located on the East flank of the Moose Mountain Anticline on Alberta Highway 66, up the hill east of the turnoff to Range Road 62A (50.867525° North Latitude, 114.751854° West Longitude). Figure 2-1 shows the outcrop's position marked with a red X on a segment of the geological surface map, combined from two 1:63360 scale map sheets (Beach, 1942a, 1942b). The outcrop location is surrounded by a 3 km radius circle with a representative sample of 40 strikes and dips (highlighted with white symbols) that were taken from the map and were used to generate a stereonet to estimate the megascopic fold axis.

The outcrop overlies a coaly section that forms the westernmost edge of the outcrop and is likely a fault-glide plane which provides a basal detachment surface that leads to the formation of a series of undulating mesoscopic folds, faults and bedding-plane slip near the base of the cliff. The surface immediately above the coal contact has broad but very open folds (150-160 degree interlimb angle) so these structures, while readily visible from across the highway, do not provide a statistically significant spread of bedding measurements with which to determine a reliable fold axis. This left three measurable fold structures, which were treated as separate structural domains. Each station was photographed from a tripod with and without the grid apparatus for later reference.

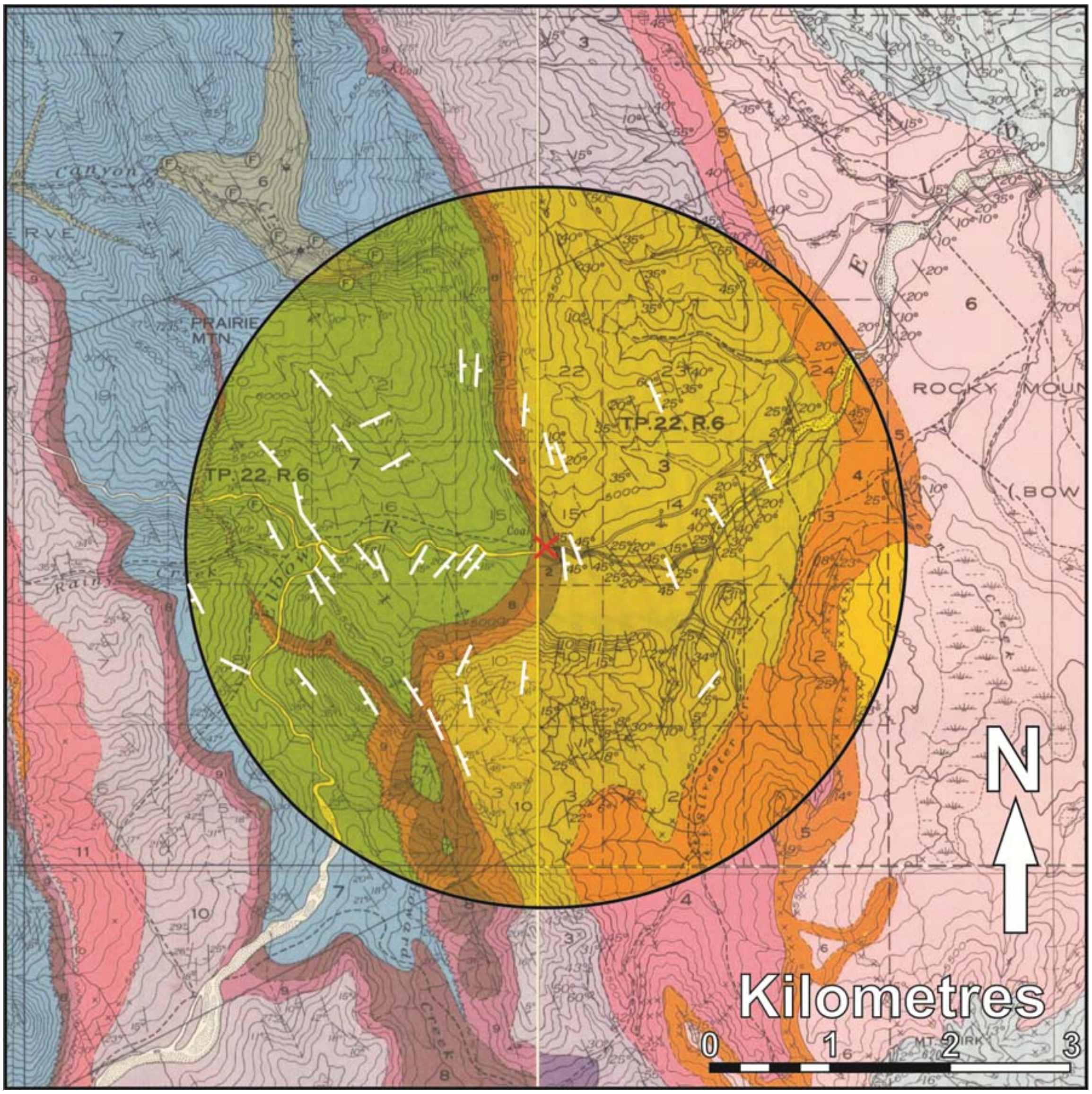

Figure 2-1: Megascopic geologic context for Elbow Falls case study
The Elbow Falls outcrop location is marked by a red X in the centre of a yellowed 3 km radius circle at the centre of this 9x9 km geologic surface map (modified from Beach, 1942a, 1942b). The strike symbols for the map measurements that were used for megascopic context are highlighted in white. (At this scale, all of the outcrop domains fall within the width of the X.)

Using the grid device for positioning the measurements provided a challenge in that each measurement was taken relative to a plane that was inclined against the outcrop and that was not levelled. That required taking the measured positions relative to the grid and first rotating them to a new coordinate system that was positioned relative to horizontal on the grid plane, and then projecting those coordinates into 3-D space, N-S E-W and Vertical (X,Y,Z). There are two corrections involved that were resolved individually. The first step was to take the rotated horizontal grid-plane coordinates and project them onto 3-D coordinates on a vertical plane that strikes the same as the horizontal grid plane, with values relative to true North and Vertical. The next step was to add a correction factor for the horizontal (X-Y or N-S E-W axis values) and vertical (Z-axis) to correct for the tilt of the measurement plane.

Each dip domain's data were plotted on a stereonet (Figure 2-2A, B and C) and the combined data from all three domains were plotted as Figure 2-2D. The megascopic map data were plotted as Figure 2-2E. The measurements are tabulated below (Table 2-1).

Table 2-1: Elbow Falls fold orientations

Location	n	Stereonet Name (Figure 2-2)	Trend (Degrees)	Plunge (Degrees)	K	C
Station 1	13	A	145.2	13.9	0.34	3.65
Station 2	12	B	143.5	7.4	0.10	3.49
Station 3	9	C	160.2	0.8	0.99	2.31
All outcrop data	34	D	145.9	8.5	0.32	2.78
Megascopic map data	40	E	154.8	5.1	0.53	3.81

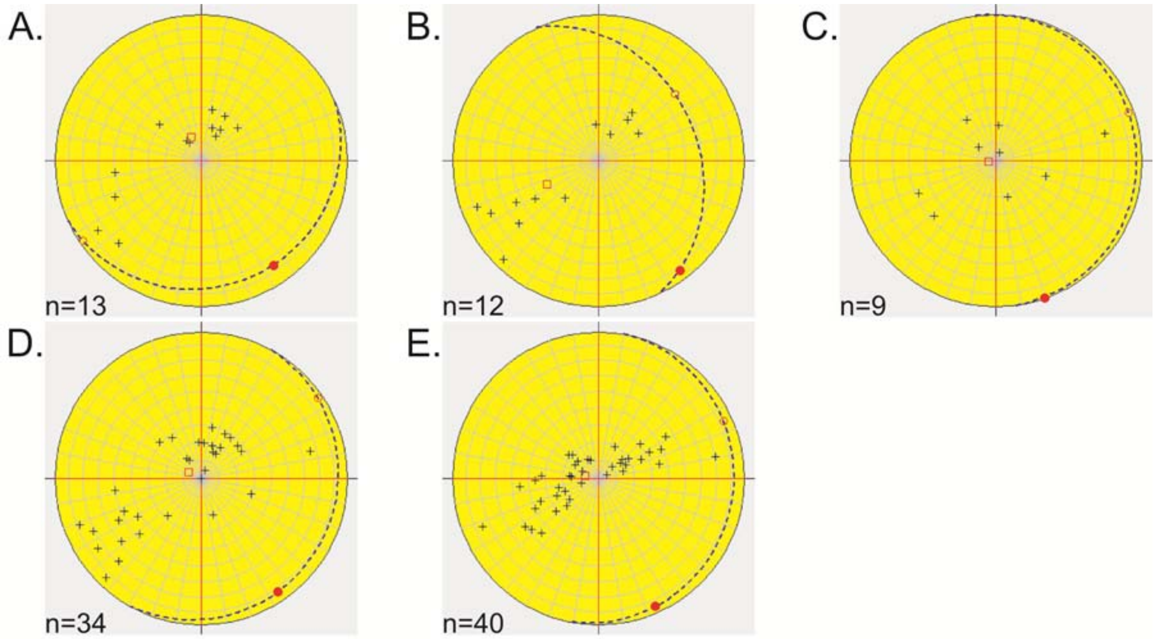

Figure 2-2: Elbow Falls stereonets
Poles to bedding are marked with black crosses in these lower hemisphere stereonets. The red dot indicates the third eigenvector-calculated fold axis and the dashed black line is the trace of the plane perpendicular to the first eigenvector. Stereonets A, B and C correspond to Stations 1, 2 and 3. Stereonet D is the sum of all the outcrop data and Stereonet E is derived from the megascopic map data.

Accompanying each photograph (and subsequent photographs in this chapter) are the dip data as projected (as fat and short red lines) in Lithotect onto a down-plunge projection plane, then interpreted as a structural line drawing. The line drawings have the interpreted bedding planes marked in orange, measured fault surfaces in purple, poles to bedding marked in cyan, and dip isogon boundaries marked in either dotted black (for bedding measurement bisectors) or green (for interpreted or inferred local fold hinge lines). Parallel bedding planes are interpolated between measurements to make a fuller synthetic borehole image later. The synthetic boreholes are drawn underneath the line drawings as shaded pastel rectangles. As the orientations of these synthetic boreholes are entirely arbitrary, they were chosen to encounter the “interesting” parts of the structures in question at a variety of angles. The scale of the projected drawings is in millimetres and the photographed grid has 20 centimetre squares.

Station 1 (Figure 2-3) shows an open kink-folded anticline with a narrow hinge zone only 40 cm wide at a maximum. The interbedded sands and shales have a variety of bed thicknesses from 1 to 15 cm. A single light grey synthetic wellbore is drawn intersecting the fold and its resulting synthetic borehole image (also shaded light grey) is drawn in Figure 2-6, Borehole A.

Station 2 (Figure 2-4) is an open kink-folded syncline (positioned immediately to the West of Station 1) with a narrow hinge zone only 20 cm wide at the maximum. The bedding averages 4 cm in thickness, with the exception being a more massive tan coloured sandstone at the base. It appears that this fold is bounded by a detachment fault at the base which accommodates the folding. A single light yellow synthetic wellbore is drawn intersecting the fold and its resulting synthetic borehole image (also shaded light yellow) is drawn in Figure 2-6, Borehole B.

Station 3 (Figure 2-5) is a complex structure that is difficult to characterize. It is an antiformal structure in thinly interbedded argillaceous beds that appear to be rotated between bounding faults above and below that separate the interbedded unit from more massive sandstones surrounding it. The hinge zone narrows from 40 cm at the top to less than 10 cm at the base, and is composed of undulating cm-scale folds in places. Two synthetic wellbores (shaded in purplish grey and greenish grey) are drawn intersecting the

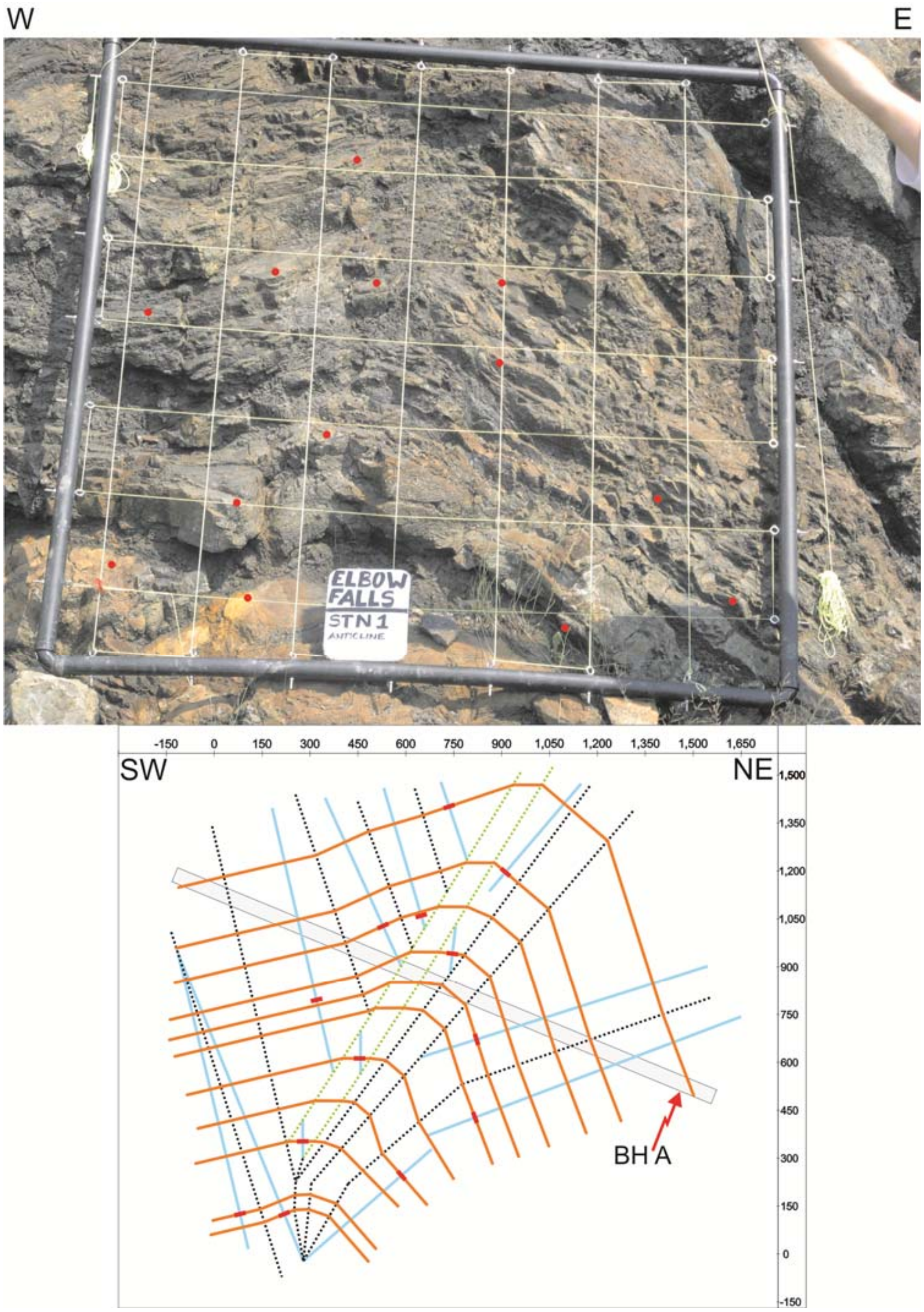

Figure 2-3: Elbow Falls Station 1
Station 1 is an open kink-folded anticline with a narrow hinge zone. Below the photograph (whose grid spacing is 20 cm) is a down-plunge projected cross-section of the bedding measurements which are marked with red bars in the cross-section and red dots on the photograph. The interpreted bedding is marked in orange, normals to bedding are marked in cyan and dip bisector isogon boundaries are dotted black and interpreted isogons are dotted green. BH A (the light grey rectangle) is the single synthetic borehole that was drawn through this fold. The cross-section's scale is in millimetres.

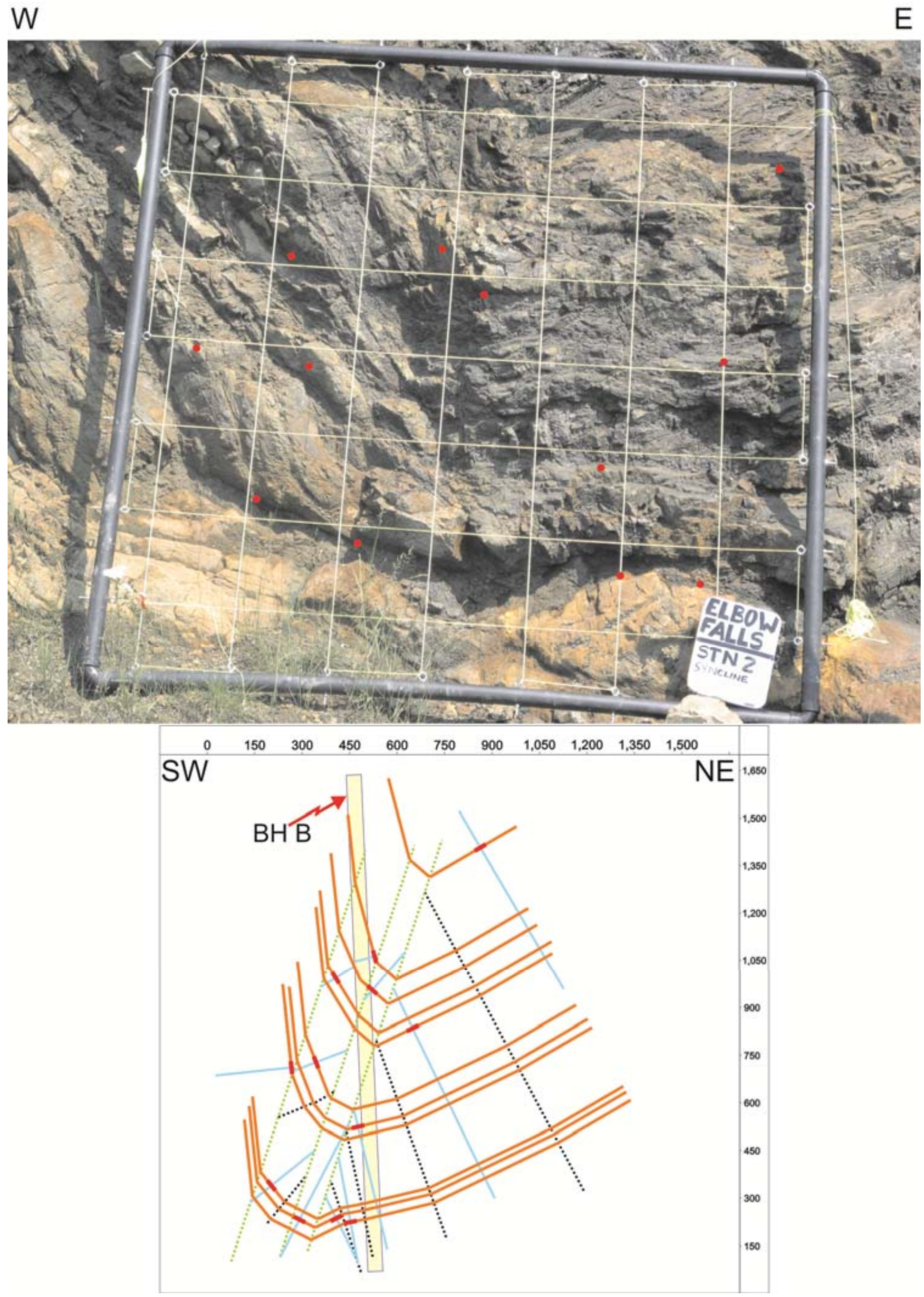

Figure 2-4: Elbow Falls Station 2

Station 2 is an open kink-folded syncline positioned immediately to the west of Station 1. Below the photograph (whose grid spacing is 20 cm) is a down-plunge projected cross-section of the bedding measurements which are marked with red bars in the cross-section and red dots on the photograph. The interpreted bedding is marked in orange, normals to bedding are marked in cyan and dip bisector isogons boundaries are dotted black and interpreted isogons are dotted green. BH B (the yellow rectangle) is the single synthetic borehole that was drawn through this fold. The cross-section's scale is in millimetres.

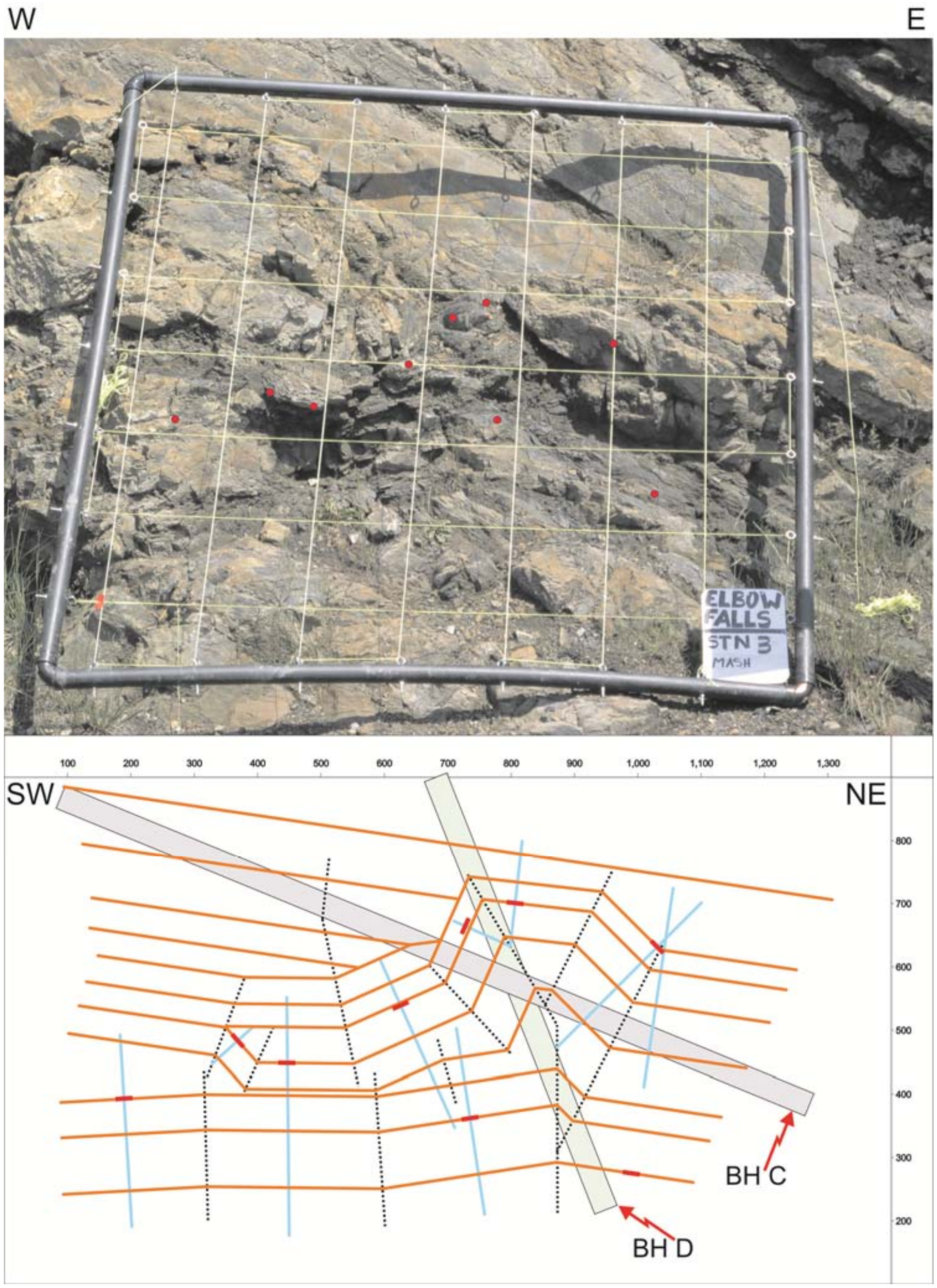

Figure 2-5: Elbow Falls Station 3
Station 3 is a complex fault-bounded antiform. Below the photograph (whose grid spacing is 20 cm) is a down-plunge projected cross-section of the bedding measurements which are marked with red bars in the cross-section and red dots on the photograph. The interpreted bedding is marked in orange, normals to bedding are marked in cyan and dip bisector isogon boundaries are dotted black. BH C and BH D (purplish grey and light green rectangles) are the synthetic boreholes that were drawn through this fold. The cross-section's scale is in millimetres.

fold, their resulting synthetic borehole images (also shaded in purplish grey and greenish grey respectively) are drawn in Figure 2-6, Boreholes C and D.

Bedding poles for Stations 1 and 2 form fairly tight girdles (evidenced by their low K and high C values) but Station 3 does not (Figure 2-2, Table 2-1), being barely on the girdle side of the $K < 1$ line with $C < 3$, indicating generally scattered orientations. This is not really surprising because the bedding in Station 3 is much more fissile and measurement planes were in pretty poor shape. I do not think that this was due to slump in the outcrop itself but is more a reflection of the nature of the folding in such a tight fold generating almost fluid motion in the shaly beds as well as reflecting generally poor bed condition due to fracturing and weathering.

Interestingly, each domain has a fairly significant deviation in its plunge directions and magnitudes (Table 2-1). While Stations 1 and 2 are almost identical in plunge trend, a 6.6 degree variation in plunge magnitude is a very significant number if one were to try to use either of these mesoscopic folds to predict a megascopic structural direction for any practical industrial application such as that involved in planning a horizontal well. Station 3 was very different than the other two stations, having a 15 degree variation in the structural trend from the other two.

The synthetic borehole image logs are shown in Figure 2-6. The outcrop-generated synthetic borehole images use the same convention as the cross-sections they are derived from where dip isogon boundaries (fold hinge traces or fault planes) are dotted black or

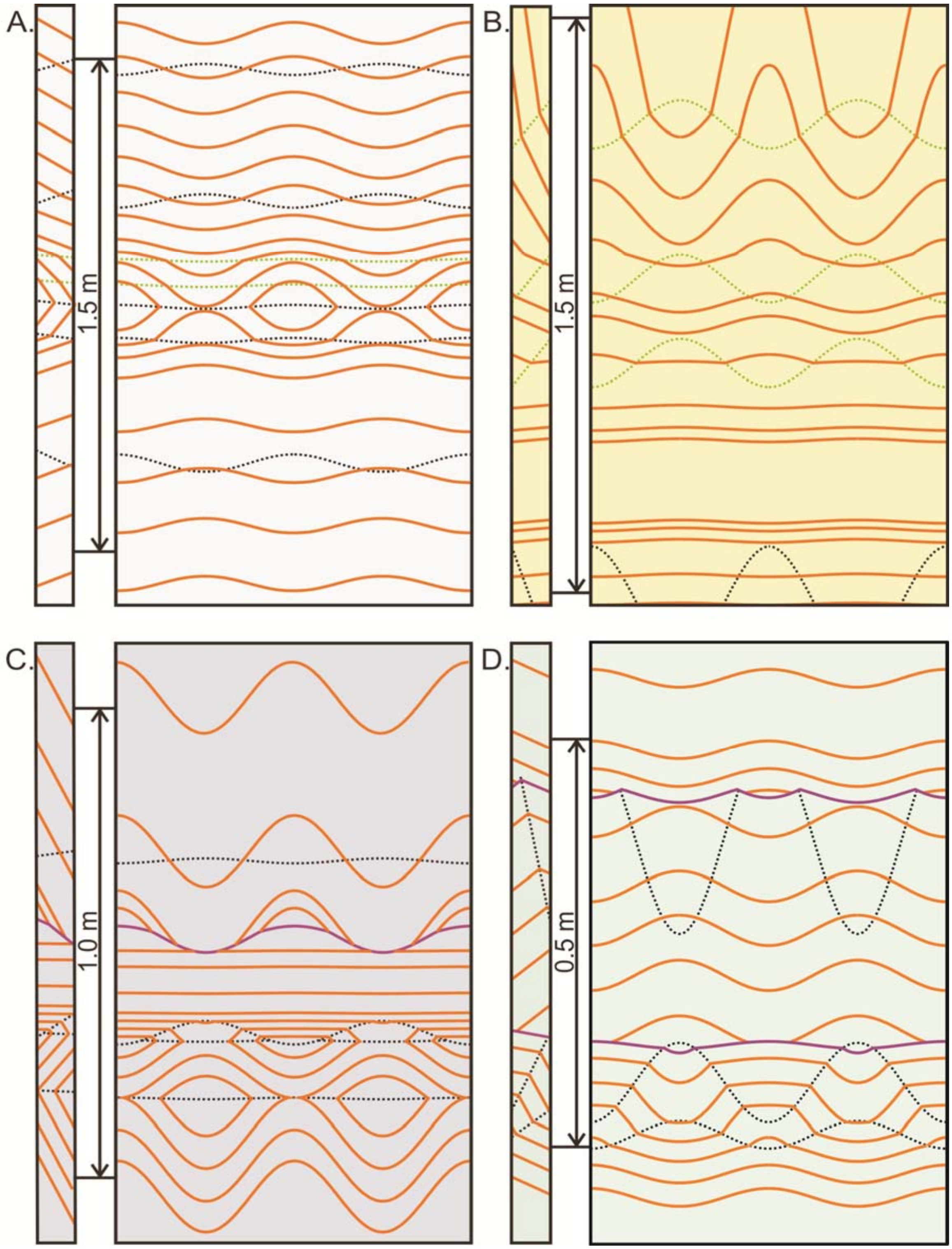

Figure 2-6: Elbow Falls synthetic boreholes
The four synthetic borehole images (A, B, C and D) are displayed doubled (horizontal scale 0-720°) and are shown next to their corresponding slices of cross-section data. Bedding is orange, faults are purple and dip isogon boundaries are dotted black or green.

green, measured faults are purple and beds are orange. Additional parallel bed sinusoids have been added where needed to make the borehole image clearer.

The first synthetic borehole (Figure 2-6 A) shows a “circle” pattern in the centre with the bedding troughs flipping direction as the wellbore cuts through the hinge of this fold. This is a result of the beds folding in and out of the borehole in a more or less symmetrical manner and is characteristic of an intersection through the core of a fold on a line perpendicular to the fold hinge.

The second synthetic borehole (Figure 2-6 B) shows a transition from long sinusoids at the top to flatter sinusoids at the base, with a subtle reversal in trough direction. Again this results from the bedding folding in and out of the borehole but in contrast to the previous example, the wellbore starts close to parallel to one of the fold limbs and ends close to perpendicular to the other limb, so the borehole is steeply inclined relative to the fold hinge plane.

The third synthetic borehole (Figure 2-6 C) has some complexity not seen in the other two images. First, near the centre, there is an inferred fault plane marked in purple with partial sinusoidal bedding truncating against it on both sides. In the bottom half of the image, there are a pair of fold hinge patterns, the upper one being an asymmetrical intersection (flat apparent dips to inclined apparent dips, meaning an oblique angle between the borehole and the fold hinge) and the lower being a more symmetrical intersection (apparent dips are similar but inverted, meaning a perpendicular angle between the borehole and the fold hinge plane). The fold hinge “circles” switch sides of the borehole, because one is a synform and the other is an antiform.

The fourth synthetic borehole (Figure 2-6 D) shows two inferred faults (one in the top quarter and another in the bottom third), where bedding truncates against a surface or other bedding. There are a couple of fold hinge planes in the lower third of the image but no “circle” pattern because the folds are open and the beds do not switch dip direction in the cross-section and the borehole intersection is not perpendicular to the fold hinge planes.

Case Study 2: Powderface Trail

The outcrop is of fine grained sandstones and shales of the lower Cretaceous Blairmore Formation, and is structurally situated in a hanging wall duplex above the Jumpingpound Mountain fault system, on the Powderface Trail about 200 m south of the trail’s southernmost crossing of Jumpingpound Creek, Alberta (50.977588° North Latitude, 114.953299° West Longitude). Figure 2-7 shows the outcrop’s position marked with a red X on a segment of the 1:63360 scale geological surface map (Beach, 1942b). The outcrop location is surrounded by a 3 km radius circle with a representative sample of 40 strikes and dips (highlighted with white symbols) that were taken from the map and were used to generate a stereonet to estimate the megascopic fold axis.

The Powderface Trail outcrop has a somewhat more difficult access than the other case study sites. It is at the top of a steep scree slope and is a small broad syncline-anticline

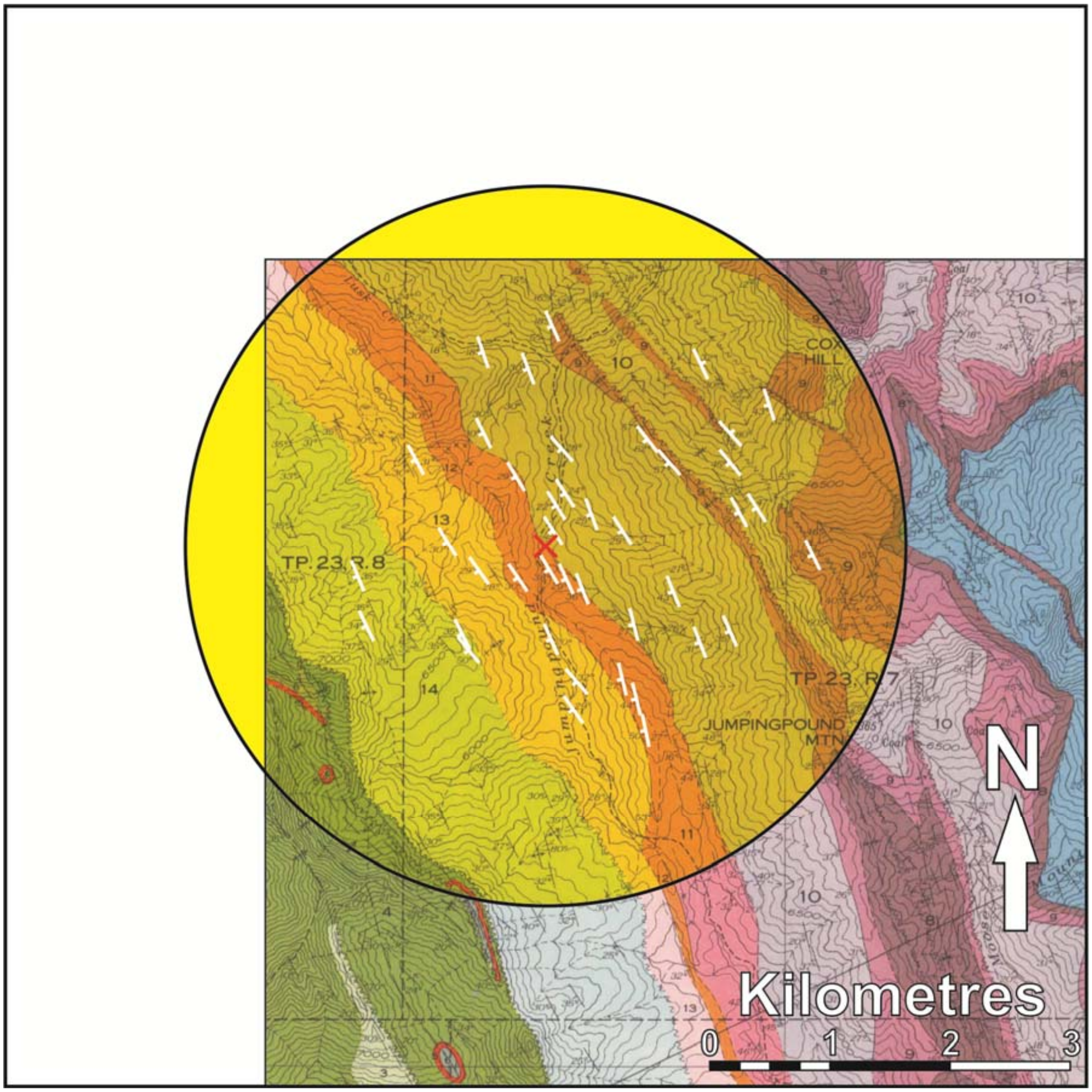

Figure 2-7: Megascopic geologic context for Powderface case study
The Powderface Trail outcrop location is marked by a red X in the centre of a yellowed 3 km radius circle at the centre of this 9x9 km geologic surface map (modified from Beach, 1942b). The strike symbols for the map measurements that were used for megascopic context are highlighted in white. (At this scale, both of the outcrop domains fall within the width of the X.)

pair in weathered mudstone with some sandier layers. While the beds are mostly fissile, there is good access to a 10 cm thick sandstone bed whose under hang forms an easily accessed planar surface that provides an excellent place to make measurements across the entire fold pair.

Because the measurements were taken relative to a known line on a near-vertical cliff face, they were projected onto a vertical plane that intersected that line by first correcting the vertical offsets to reflect the plunge of the reference line, then being projected onto a N-S, E-W, vertical coordinate system (X,Y,Z) with no correction necessary for the tilt of the outcrop or measurement axis. Each fold (the anticline and the syncline) was treated as a separate structural domain.

Each dip domain’s data were plotted on a stereonet (Figure 2-8A and B) and the combined data from the two domains were plotted as Figure 2-2C. The megascopic map data were plotted as Figure 2-8D. The measurements are tabulated below (Table 2-2).

Table 2-2: Powderface fold orientations

Location	n	Stereonet Number (Figure 2-8)	Trend (Degrees)	Plunge (Degrees)	K	C
Station 1	6	A	341.0	3.7	0.82	4.01
Station 2	3	B	333.8	2.8	0.09	10.15
All outcrop data	9	C	335.1	4.2	0.62	4.55
Megascopic map data	41	D	325.8	3.9	1.17	3.81

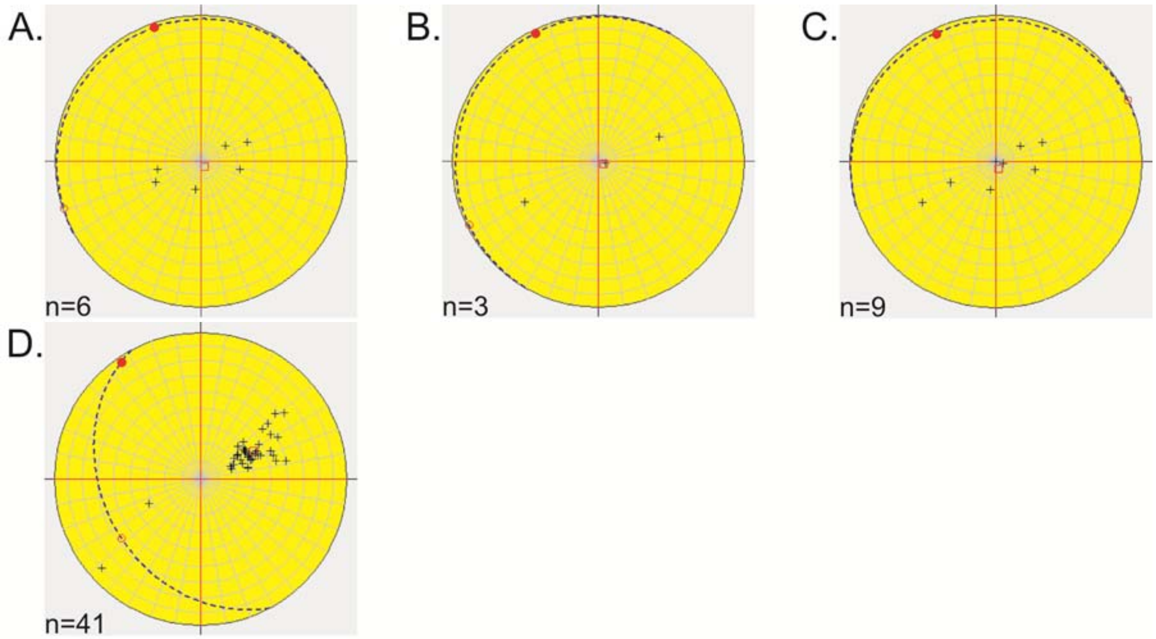

Figure 2-8: Powderface Trail stereonets
Poles to bedding are marked with black crosses in these lower hemisphere stereonets. The red dot indicates the third eigenvector-calculated fold axis and the dashed black line is the trace of the plane perpendicular to the first eigenvector. Stereonets A and B correspond to Stations 1 and 2. Stereonet C is the sum of all the outcrop data and Stereonet D is derived from the megascopic map data.

The data are pretty sparse (as there was only one bedding surface that could be reliably measured) but Station 1 forms a moderately tight girdle while Station 2 has only 3 measurement points with a near perfect fit through the data, but not a large enough sample size to conclude that this is due to anything but chance.

The two domains have modest plunges (2.8 versus 3.7 degrees) and the differences in their fold trends are not significant as the raw data were measured to +/- 1 degree. Despite that, each domain is projected individually to its own cross-section (Figure 2-9) using the same line colour conventions as outlined in the Elbow Falls outcrop. Because the two folds are not significantly different in shape from those seen in the Elbow Falls

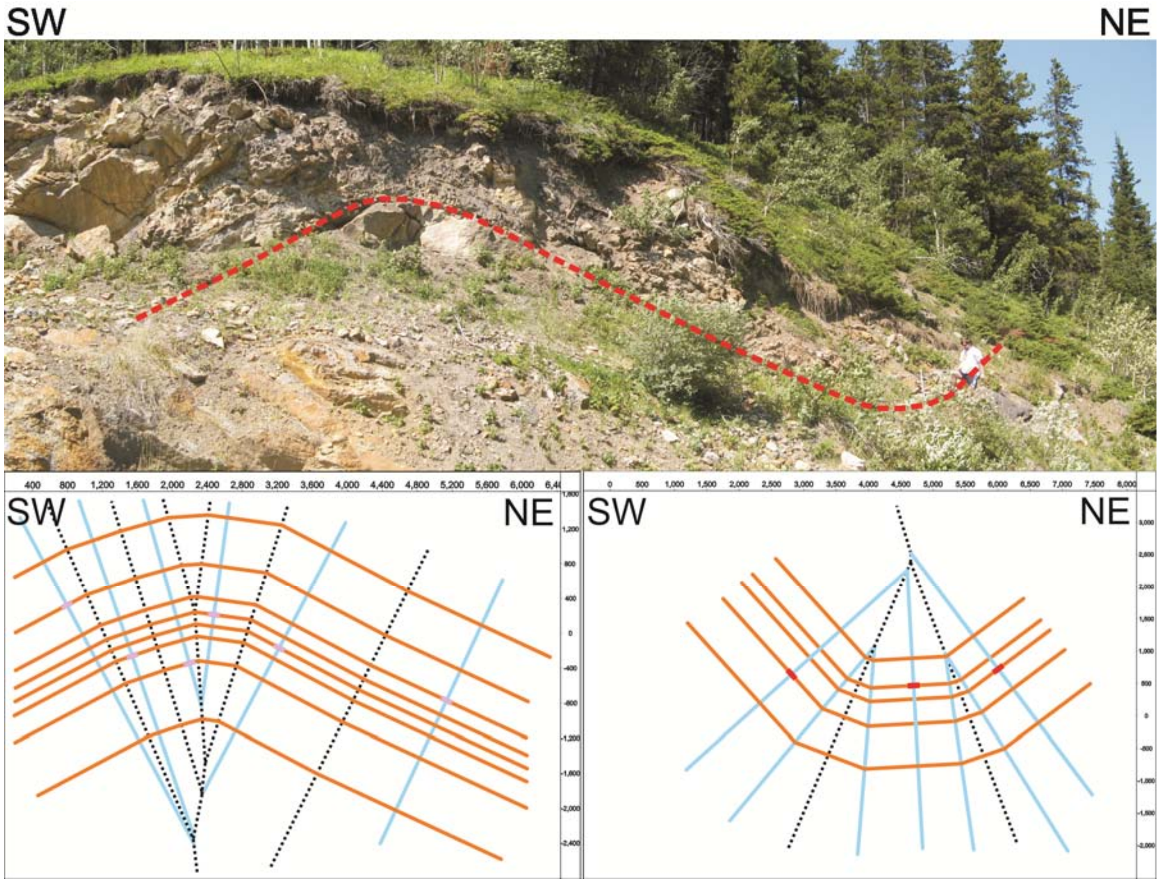

Figure 2-9, Powderface Trail outcrop and cross-sections
The Powderface Trail outcrop is an anticline-syncline pair. Below the photograph (which shows a dashed red line indicating the approximate shape of the folded bedding) is a down-plunge projected cross-section of the bedding measurements. The interpreted bedding is marked in orange, normals to bedding are marked in cyan and dip bisector isogons are dotted black. The cross-sections' scales are in millimetres.

Outcrop, Stations 1 and 2, there was nothing to gain by drawing another set of synthetic boreholes through these cross-sections.

Case Study 3: Cascade

The outcrop is interbedded siltstones and shales of the Jurassic Fernie Formation that are structurally situated in the duplexed and overturned west limb of the Mount Allan Syncline on the North side of the Trans-Canada highway, about 300 m east of the

Banff/Lake Minnewanka overpass, east of Cascade Mountain (51.207912 North Latitude, 115.526052° West Longitude). Figure 2-10 shows the outcrop's position marked with a red X on a segment of the geological surface map, combined from two 1:50000 scale map sheets (Price and Mountjoy, 1970, 1972). The outcrop location is surrounded by a 3 km

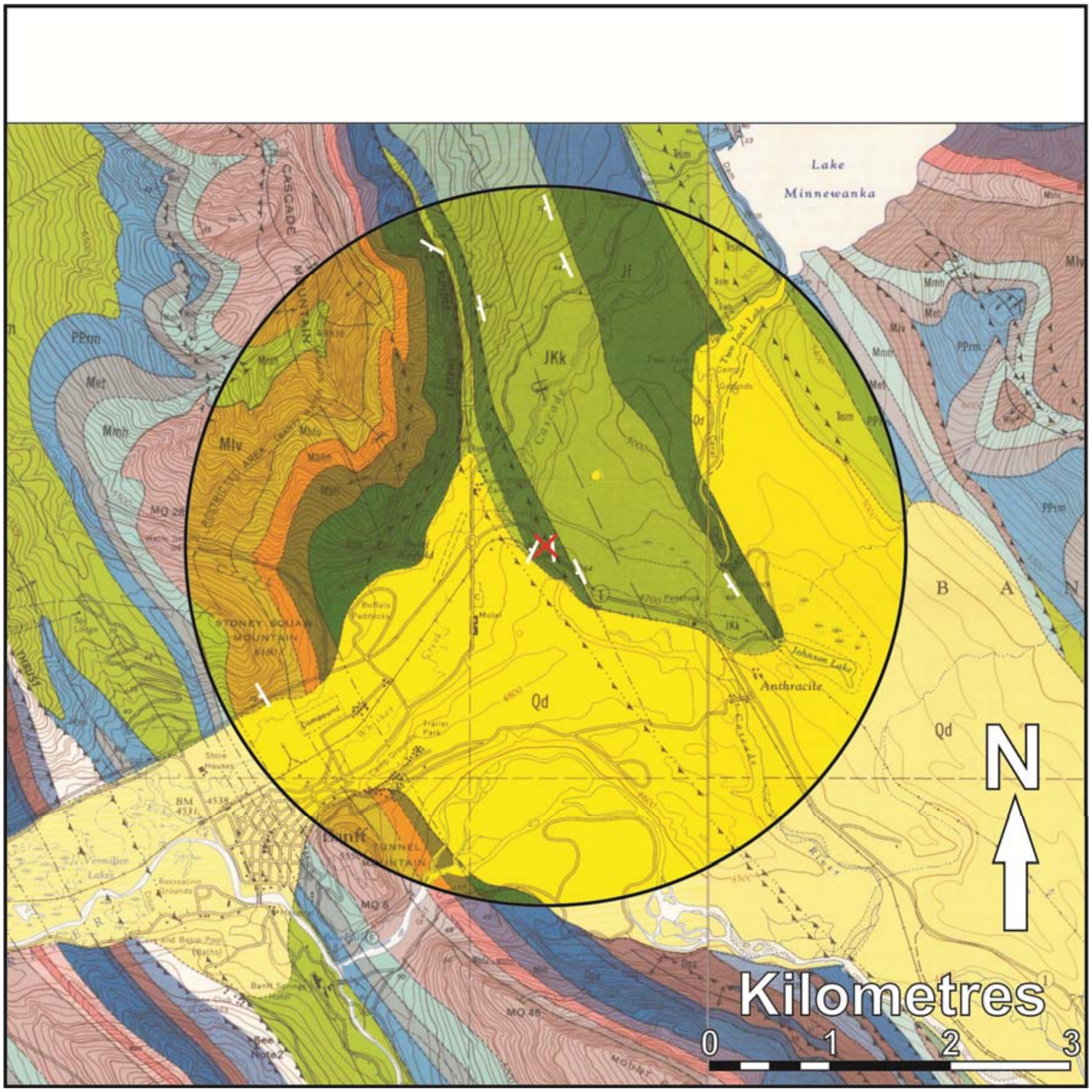

Figure 2-10: Megascopic geologic context for Cascade case study
The Cascade outcrop location is marked by a red X in the centre of a yellowed 3 km radius circle at the centre of this 9x9 km geologic surface map (from Price and Mountjoy, 1970, 1972). The strike symbols for the map measurements that were used for megascopic context are highlighted in white.

radius circle with the nine strikes and dips in that circle (highlighted with white symbols) that were used to generate a stereonet to estimate the megascopic fold axis.

The access is easy, being in the road cut of the highway at the top of a small scree slope that has likely been expanded because of the large number of geologists who stop there to look around. Unfortunately, the most dramatic parts of the folds are near the top of the cliff and are therefore inaccessible without significant safety gear and climbing skill that I do not possess, so only the one fold that is exposed near the base of the cliff face was measured.

The positioning of the measurements was done in the same way as the Elbow Falls measurements (using the grid apparatus) so the same corrections were necessary: rotation to a horizontal coordinate system in the plane of the measurement grid, projection of that plane onto a vertical plane whose strike was parallel to the grid's strike in N-S, E-W and vertical (X,Y,Z) coordinates and then correcting the X-Y and Z axis error for the tilt of the reference plane's coordinate system.

Bedding data were plotted on a stereonet (Figure 2-11A) and the megascopic map data were plotted as Figure 2-11B. The megascopic map data without one SE dipping outlier were plotted as Figure 2-112C as well as Cant and Stockmal's (1999) nearby measurements (Figure 2-11D). The measurements are tabulated below (Table 2-3).

Table 2-3: Cascade fold orientations

Location	n	Stereonet Number (Figure 2-11)	Trend (Degrees)	Plunge (Degrees)	K	C
Station 1	8	A	202.9	12.1	0.11	2.23
Megascopic map data	9	B	167.1	8.0	7.69	2.64
Megascopic map data without SE dip	8	C	158.6	4.5	0.89	3.61
Cant and Stockmal (1999)	≥17	D	319.2	37.4	-	-

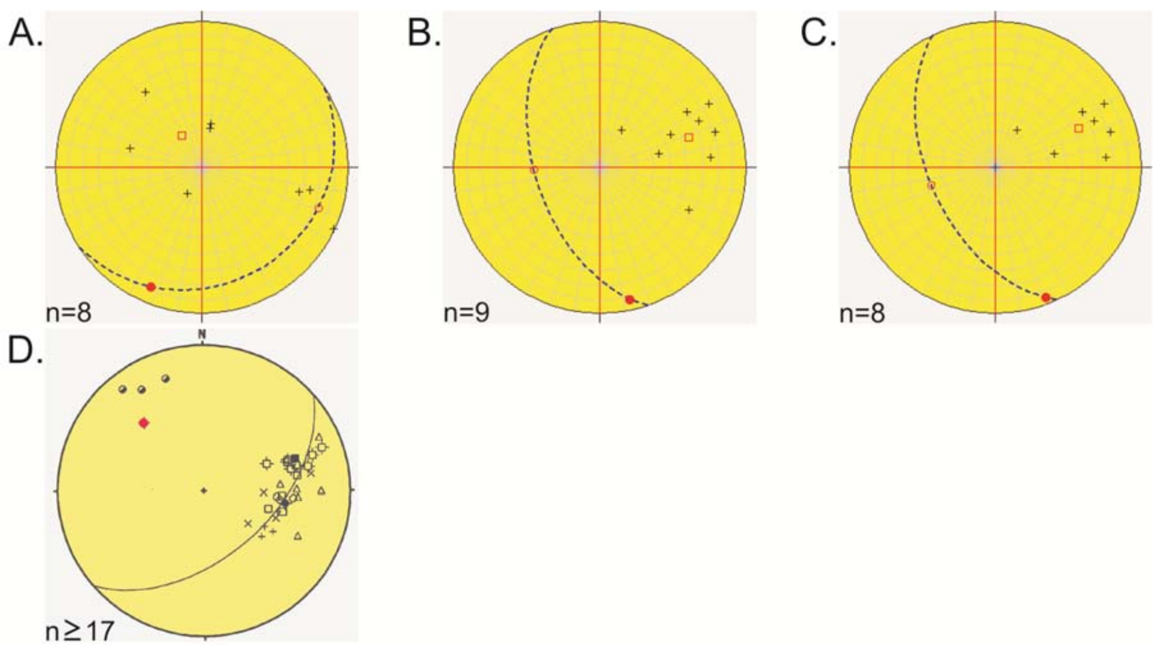

Figure 2-11: Cascade stereonets
Poles to bedding are marked with black crosses in the first two lower hemisphere stereonets. The red dot indicates the third eigenvector-calculated fold axis and the dashed black line is the trace of the plane perpendicular to the first eigenvector. Stereonet A is from the field measurements, Stereonets B and C are derived from the megascopic map data with and without an outlier dip and Stereonet D is modified from Cant and Stockmal (1999), showing a variety of measurements divided by dip panel with a solid line representing the best-fit great circle perpendicular to the fold axis. As in the other stereonets, the fold axis is highlighted with a red dot.

The fold is projected down plunge onto a cross-section (Figure 2-12), using the same line colour conventions as outlined in the Elbow Falls outcrop. Two synthetic boreholes are indicated in pale yellow and pale grey rectangles and the resulting synthetic borehole images are drawn as Figure 2-13, Boreholes A and B.

The fold's bedding is composed of fine grained sandstone surrounded by shattered shales that, in places, have been contorted such that primary bedding is impossible to discern visually, much less measure, and has no apparent geometric relation to the twisted sandstone unit it surrounds. Rather the surrounding shale seems to be a malleable mass that moved around in a plastic (almost fluid-like) deformation to accommodate the folding in the more competent units. The sandstone bedding is extremely contorted here, with the main sandy bed being internally broken up, twisted and rotated into sheared sub-folds (crenulations) as small as 20 cm in wavelength.

This fold has a significant amount of scatter in its bedding pole data ($C < 3$) but it is a strong girdle ($K << 1$). It has a structural trend that is at odds with the megascopic structural trend. It is difficult to know whether this incongruence is a result of local rotational shearing in the structure itself due to an underlying lateral ramp structure, rotation into an unmapped strike-slip tear fault or rotation on an obliquely oriented fault plane. This incongruous direction was noted on Price and Mountjoy's (1972) map as a steep bed measurement whose dip and dip directions are 57°/295°NW. This outlier dip is far enough off the girdle as to give a K value of 7.69 (a broad cluster) when it is included and 0.89 (a loose girdle) when it is not included (see Table 2-3, Figure 2-11).

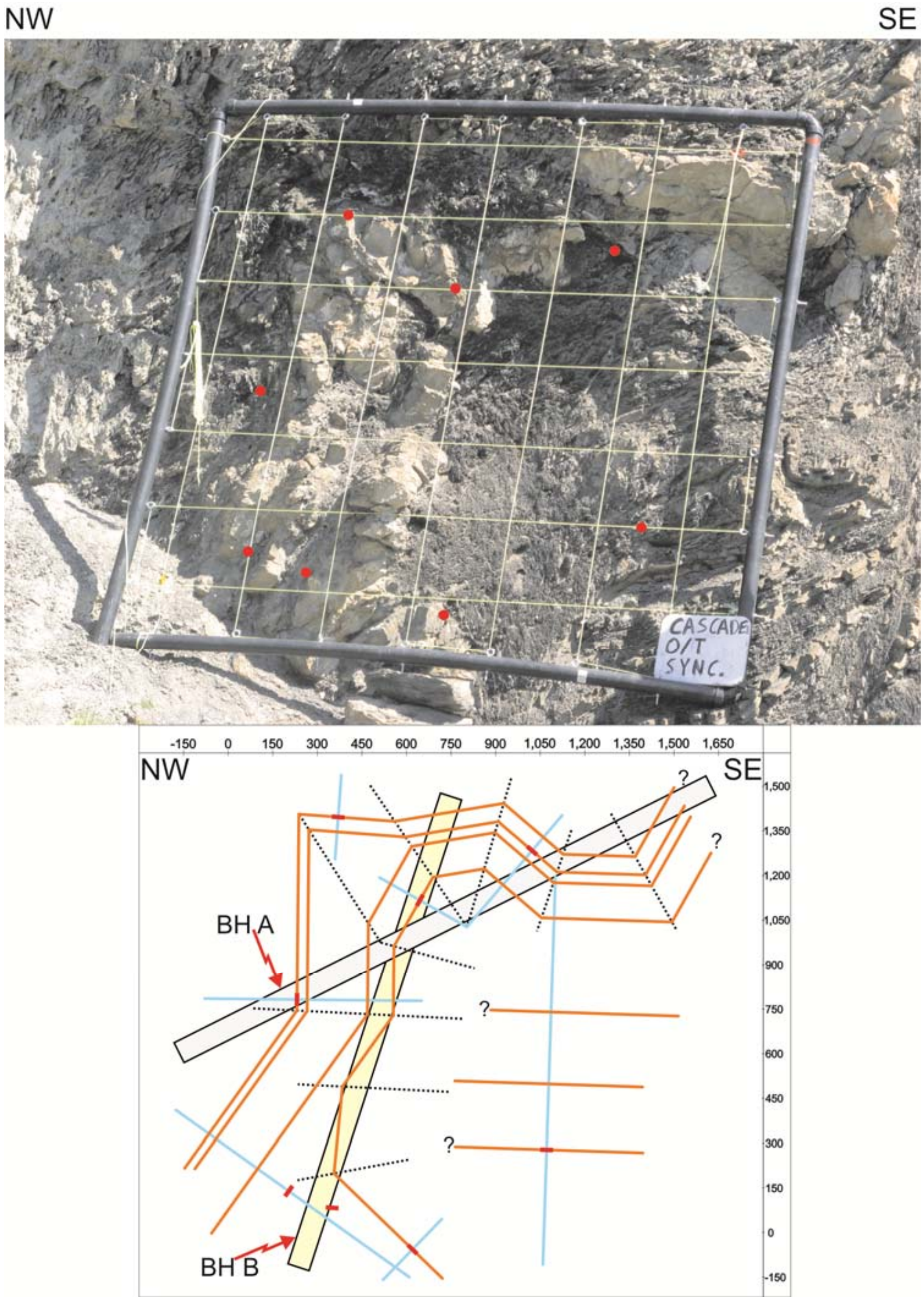

Figure 2-12: Cascade outcrop and cross-sections

The Cascade structure is a crenulated antiform bound by shale whose bedding is difficult to discern. Below the photograph (whose grid spacing is 20 cm) is a down-plunge projected cross-section of the bedding measurements which are marked with red bars in the cross-section and red dots on the photograph. The interpreted bedding is orange, normals to bedding are marked in cyan and dip bisector isogon boundaries are dotted black. BH A and BH B (the light grey and light yellow rectangles) are the synthetic boreholes that were drawn through this fold. The cross-section's scale is in millimetres.

The majority of the measurements were taken from the top or bottom of a sandy bed where it contacted the surrounding fissile shale and there were few slickensides on these surfaces so I do not believe that systematic misidentification of the measured bedding could have taken place such that the structural trend could have been rotated 35 degrees from the megascopic trend. This leads me to conclude that the structure itself is likely measured correctly but is quite incongruous when compared to the megascopic structural regime.

Cant and Stockmal (1999) did some structural and stratigraphic measurements of the entire Fernie Formation outcrop along Highway #1, dividing the outcrop into four panels that were bound by significant faults. The minor fold I measured was on the eastern edge of their Panel 2 and they observed that Panel 3 (the one immediately to the East) had an anomalous structural orientation noting: “Bedding attitude is quite uniform across Panel 3 ... mean orientation is 209.2°/42.7°1 (a ca. 30° clockwise change in strike from Panel 2)” and thus had anomalous paleocurrent directions as well. They concluded: "Because the nature of motion along the faults which bound Panel 3 is unknown (i.e. the path by which Panel 3 was rotated to its present "anomalous" orientation), paleocurrent measurements cannot be rotated back to a pre-deformational attitude about any meaningful axis."

The minor fold I measured also has a > 30° clockwise change in strike from Panel 2 (comparing stereonets A and C from Figure 2-11) so I would be inclined to reach a different conclusion than Cant and Stockmal (1999) did. Because the minor fold immediately adjacent to the fault between Panels 2 and 3 approximates the structural rotation observed in Panel 3, it is reasonable to conclude that this fold is a fault-drag structure associated with that boundary fault. This minor fold thus is likely a result of motion on a fault whose orientation is oblique to the megascopic structural plane and thus could be taken as a snapshot of the deformational axis for their Panel 3.

Whether this fold is related to the nearby fault or not, this mesoscopic structure's orientation represents a failure in using a single mesoscopic fold to predict the megascopic fold axis per the Dale-Pumpelly Principle, because it is clearly affected by something local that is oblique to the megascopic trend.

The two synthetic borehole image logs are shown in Figure 2-13 using the same line colour conventions as explained in the Elbow Falls Case Study. B. The first synthetic borehole (Figure 2-13A) shows a pair of fold core "circles" that are positioned on opposite sides of the wellbore, indicating that one is a synform and the other is an antiform and that the borehole intersection is close enough to perpendicular to the fold hinge plane to see both limbs. The second synthetic borehole (Figure 2-13B) shows a threesome of fold core circles, two on one side and one on the other side of the wellbore. This arises because while the measured structure is an overturned syncline, the core of the structure has bedding crenulations that locally fold the bedding into an antiform. Comparing these two synthetic borehole images, the fold hinge circles have different shapes as a result of how tight the folds are. The first image has wide, squat "circles" because the folds are tight whereas the second image has longer "circles" because the crenulations are more open.

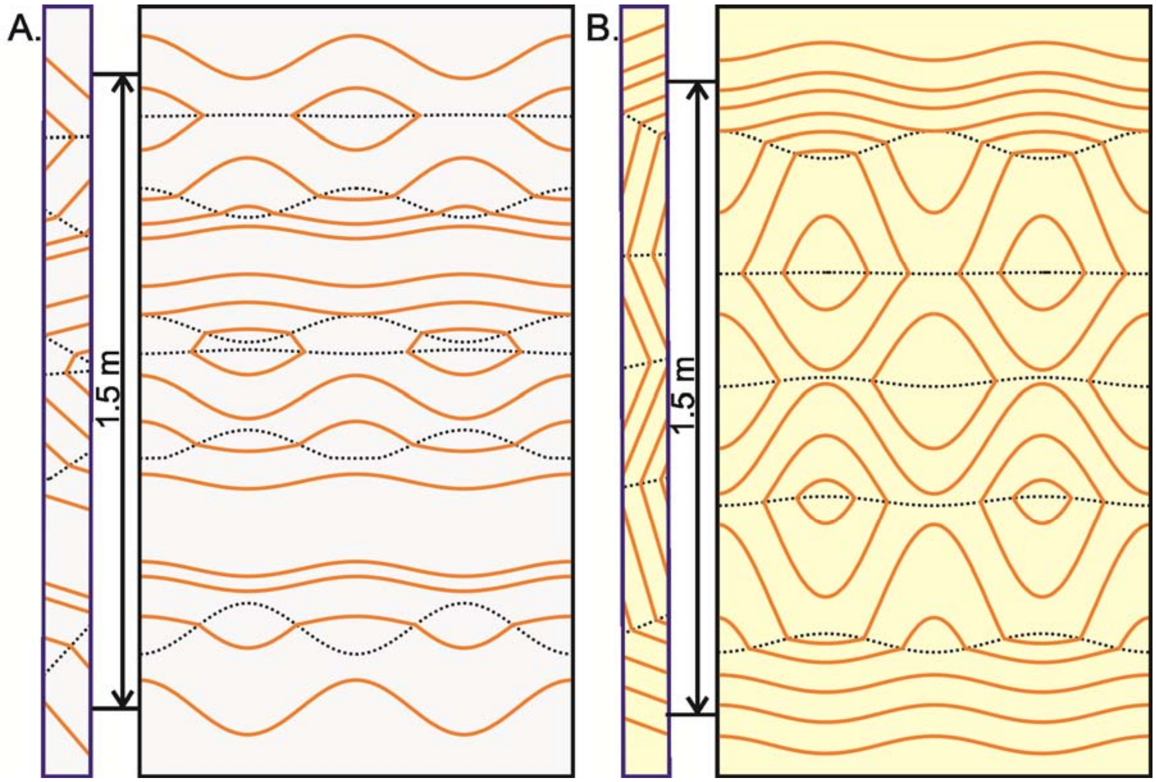

Figure 2-13: Cascade synthetic boreholes
Each of the synthetic borehole images (A and B) are displayed doubled (horizontal scale 0-720°) and are shown next to their corresponding slices of cross-section data. Bedding is orange, faults are purple and dip isogon boundaries are dotted black or green.

Case Study 4: Canmore Nordic Centre

The outcrop is interbedded carbonaceous sandstones and shales of the Kootenay Formation that are structurally below the Rundle Thrust, located at the intersection of Three Sister's Drive and Spray Lakes Road in the town of Canmore, Alberta (51.077221° North Latitude, 115.365297° West Longitude). Figure 2-14 shows the outcrop's position marked with a red X on a segment of the 1:50000 scale geological surface map (Price and Mountjoy, 1970). The outcrop location is surrounded by a 3 km radius circle with the 34 strikes and dips in that circle (highlighted with white strike symbols) that were used to generate a stereonet to estimate the megascopic fold axis.

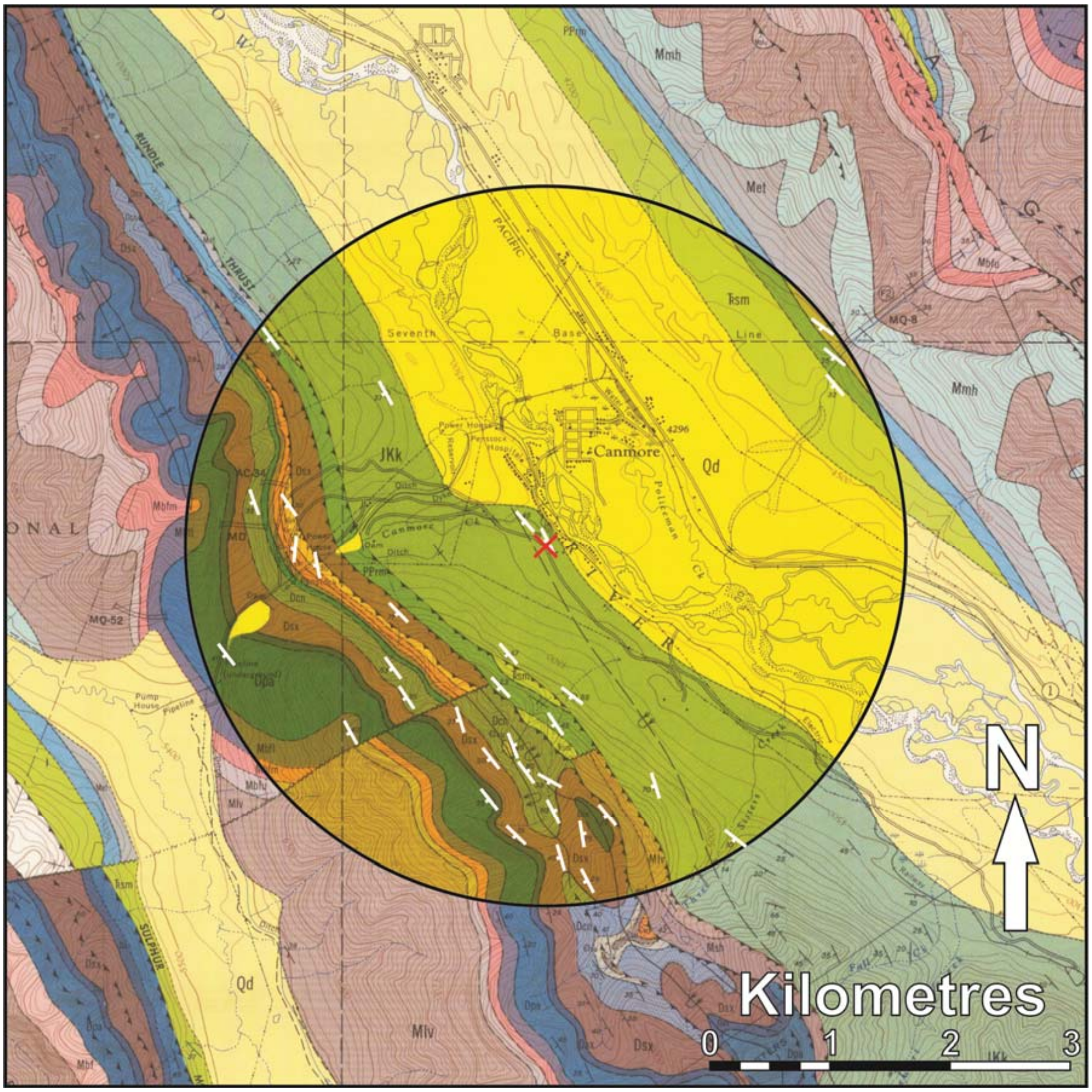

Figure 2-14: Megascopic geologic context for Canmore case study
The Canmore Nordic Centre outcrop location is marked by a red X in the centre of a yellowed 3 km radius circle at the centre of this 9x9 km geologic surface map (modified from Price, 1970). The strike symbols for the map measurements that were used for megascopic context are highlighted in white. (At this scale, all of the outcrop domains fall within the width of the X.)

The exposure could not have been easier to access. There are good viewpoints from across the road to get an overall picture and one can climb right up to the outcrop for detailed measurement of a variety of mesoscopic structures that are located atop a short scree slope above a sidewalk. Many of the features are preserved within decimetre-thick sandstone beds that stand out from the surrounding fissile shales. The shales themselves were often measurable as minor compositional differences within them caused some beds to stand proud from others but the majority of the measurements were taken on the curving sandstone beds.

Because of the excellent exposure and the size and number of measurable structures, a different approach was taken in positioning the measurements. In a preliminary outing to the outcrop, a series of photographs were taken from a stationary tripod that was positioned to the west, across the road. These photographs were then stitched together and printed out as a series of photos that were taken back to the outcrop when it came time to do the measurements. On the second outing, my field assistant and I laid out a measuring tape along the straight line of the sidewalk and placed sizable rocks along the tape at 2 metre intervals exactly. The trend and plunge of the sidewalk line as well as the approximate dip and trend of the cliff face were measured, and a number of photographs were taken with the grid apparatus laying flat against the cliff face for local scale. A second panorama was shot from a new stationary position (with fixed camera aperture and exposure time) that was positioned somewhat better for looking into the dip of the bedding rather than oblique to it like the first set.

Then, using the original panorama pictures, I took dip and dip azimuth measurements along the structures and my field assistant recorded their positions on the preliminary photographs themselves, with the plan of calculating their positions later. The computation of the true position of the measurements provided some challenge as the second panorama (with the rocks for scale, and oriented so that the camera swept around on a horizontal plane) is distorted because the distance to the outcrop changes as the camera rotates on the tripod and also because of parallax because the centre of the photograph is at a different point as the camera rotates. Fortunately, the panorama stitching software that I used (Canon Utilities PhotoStitch) includes a correction for parallax effect (it distorts the square photographs into rounded rectangles appropriately so that they are all projected as if they were taken from a single ultra-wide-angle lens). This made stitching the photographs together a trivial operation.

Taking that stitched-together panorama, I looked at the horizontal scale of the rocks on the sidewalk and in CorelDraw, drew grid lines spaced 2 decimetres apart as on the grid apparatus. These grid lines were then stretched or compressed so that they superimposed upon the scale of the reference rocks that were laid upon the sidewalk at 2 metre spacing. This gave a set of grid lines that correctly narrowed in spacing as the distance to the outcrop increased.

The next step was to determine the vertical distortion (as there is a similar narrowing of the grid lines vertically as the distance increases from the viewer). Further, the scale distortion is different vertically than the horizontal scale distortion so it wasn’t merely a question of making the gridding square. To compute how much the gridding needed to be compressed or expanded to represent 2 decimetre spacing, the new panorama was compared to the reference photographs taken with the grid apparatus. Then at each point where there was a photograph of the grid apparatus (coinciding with the most interesting structures and therefore the centres of the dip domains), the vertical compression of the reference grid was visually correlated to get a true vertical scale. Then between these points where there was a reference vertical scale photograph, the change in the vertical scale was interpolated linearly, and on the South and North ends of the outcrop was extrapolated linearly. Because the vertical scale tapers with increasing distance from the camera, the scale lines are offset at the boundaries between the reference grids. To minimize the error at the boundary between reference grids, they were aligned so that they originated relative to a single horizontal reference datum line that passed through the middle of the measurements. The outcrop is shown in Figure 2-15, with and without the scale with the dip measurement points indicated with red circles.

The superimposition of the gridding provided a vertically oriented reference plane whose gridding was square to the horizon. The measurement points were then transcribed from the field photographs to this final scaled panorama (which included a visual inspection of where a measurement would actually have been possible). The horizontal positioning relative to this reference plane was then noted. The vertical positioning was read off as well with an attempt to reconcile measurements that were near the boundaries of the reference sub-grids.

These coordinates were then taken to be on a vertical plane in a vertically oriented N-S, E-W (X-Y-Z) coordinate system. Then the X-Y positioning was corrected to account for the measured 60-degree dip of the cliff-face. There was no correction to the Z-axis

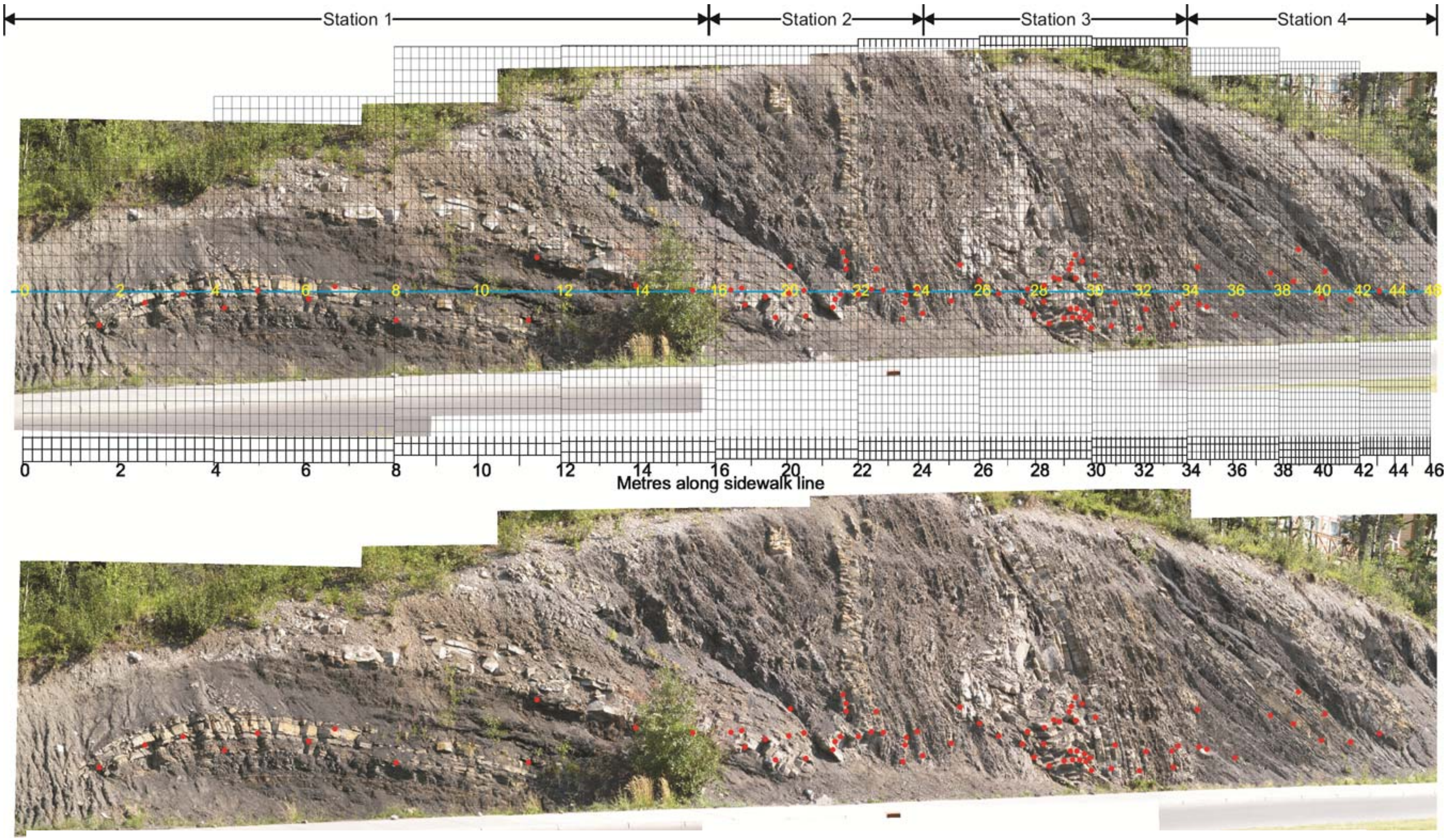

Figure 2-15: Canmore outcrop scale conversion method

The whole Canmore Nordic Centre outcrop is shown, first with the scale grid (in metres) as well as the blue reference datum line used for positioning the outcrop measurements (marked with red dots) in 3-D space. The lower image shows just the outcrop and the measurement points. Visible near the base of the image are rocks placed every 2 metres at the top edge of the white sidewalk.

positioning as the distance from the camera to the cliff face (10-30 m) was much greater than the horizontal difference between the reference datum (0-20 cm) and the measurements. Given the vertical spread of the measurements relative to the datum (+/- 1m), the projection lines from the camera to the cliff face had a maximum plunge of arctan(1 m/10 m) = 4.40°. A 4.4° error over a distance of up to 20 cm leads to a maximum vertical error of 20 cm*tan(4.4°) = 1.54 cm, which is smaller than the size of the compass itself and smaller than the errors in determining the vertical scale from the reference photographs, and was therefore considered to be acceptable.

Each dip domain's data were plotted on a stereonet (Figure 2-16A, B, C and D) and the sum of all four domains was plotted as Figure 2-16E. The megascopic map data were plotted as Figure 2-16F. The measurements are tabulated below (Table 2-4). Each domain was projected down plunge onto its own cross-section, using the same line colour conventions as outlined in the Elbow Falls outcrop.

Table 2-4: Canmore fold orientations

Location	n	Stereonet Name (Figure 2-16)	Trend (Degrees)	Plunge (Degrees)	K	C
Station 1	11	A	144.6	15.4	0.70	6.10
Station 2	26	B	162.8	13.8	0.23	3.56
Station 3	30	C	329.3	10.3	0.28	2.52
Station 4	15	D	154.9	9.5	0.44	4.65
All outcrop data	81	E	157.0	4.7	0.24	2.59
Megascopic map data	34	F	150.6	3.5	0.83	3.61

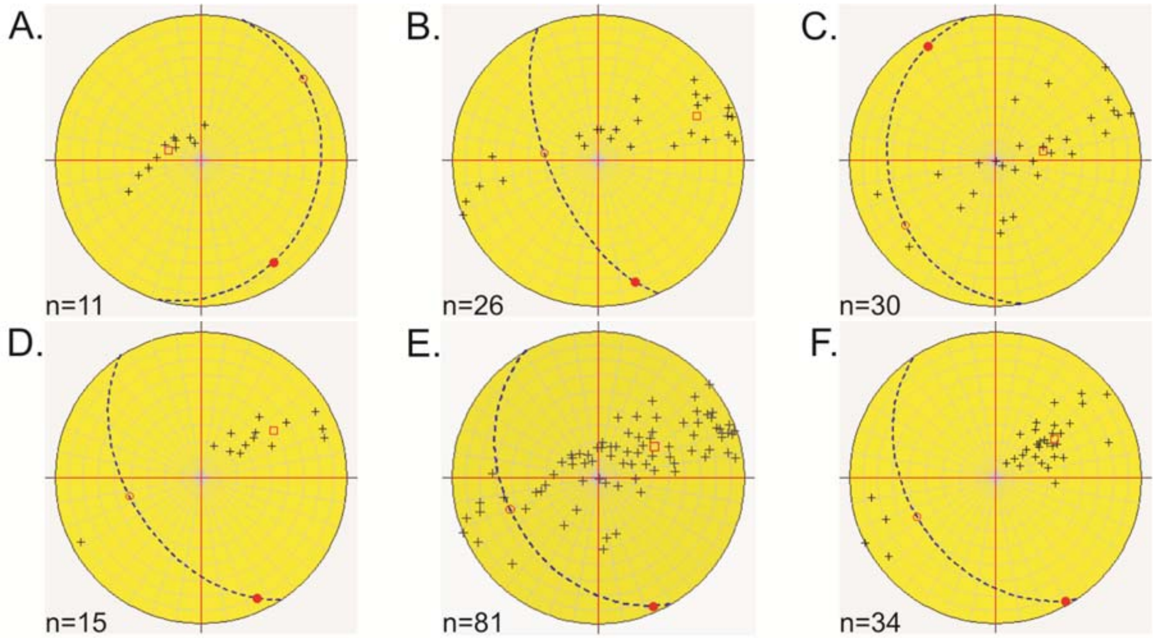

Figure 2-16: Canmore Nordic Centre stereonets
Poles to bedding are marked with black crosses in these lower hemisphere stereonets. The red dot indicates the third eigenvector-calculated fold axis and the dashed black line is the trace of the plane perpendicular to the first eigenvector. Stereonets A, B, C and D correspond to Stations 1, 2, 3 and 4. Stereonet E is the sum of all the outcrop data and Stereonet F is derived from the megascopic map data.

Station 1 (see Figure 2-17) is a gently curving open anticline with a continuous, broad hinge. The interbedded sandstones and shales have a variety of bed thicknesses from 1 mm to 15 cm. No boreholes were drawn through Station 1 because it is a simple anticline that would yield a synthetic borehole image similar to Elbow Falls Stations 1 and 2.

Station 2 (See Figure 2-18) is a close syncline with an angular hinge zone and apparent thickening in the core of the fold. The sandstone beds range in thickness from 1 to 20 cm and are interbedded by 1 mm to 5 cm shale zones. Two rectangular imaginary boreholes were drawn through Station 2 (pale grey and pale yellow) and the resulting synthetic borehole images are drawn as Figure 2-21 Boreholes A and B.

Station 3 (see Figure 2-19) is a close anticlinal structure that is bounded by a near vertical fault that truncates steeply dipping interbedded sandstones and shales on the right side and is bounded by a low-angle fault at the base on the left that juxtaposes the sandstones against thin siltstones and shales that wrap around the fold in a manner that suggests detachment between the different lithologies. Two rectangular imaginary boreholes were drawn through Station 3 (pale purple and pale green) and the resulting synthetic borehole images are drawn as Figure 2-21 Boreholes C and D.

Station 4 (see Figure 2-20) has two generations of faulting associated with subtle folding. The left half of the station has vertically dipping 1 to 5 cm sandstone and shale interbeds that are truncated by a near-vertical fault. The right half of the station has moderately dipping shale beds with a small low angle (relative to bedding) fault duplex in a 10 cm thick shale bed. Two rectangular imaginary boreholes were drawn through Station 4 (pale orange and blue-grey) and the resulting synthetic boreholes images are drawn as Figure 2-22 Boreholes E and F.

Station 1's bedding poles form a very tight stereonet girdle, while Stations 2 and 4 have a moderate spread (as evidenced by their moderately low C values in Table 2-4), all plunging towards the southeast. Station 3 has a very broad stereonet girdle ($C < 3$) because it was in this domain where there seemed to be a mismatch between the bedding on the inside and outside of an individual fold and it is in this interval where the most

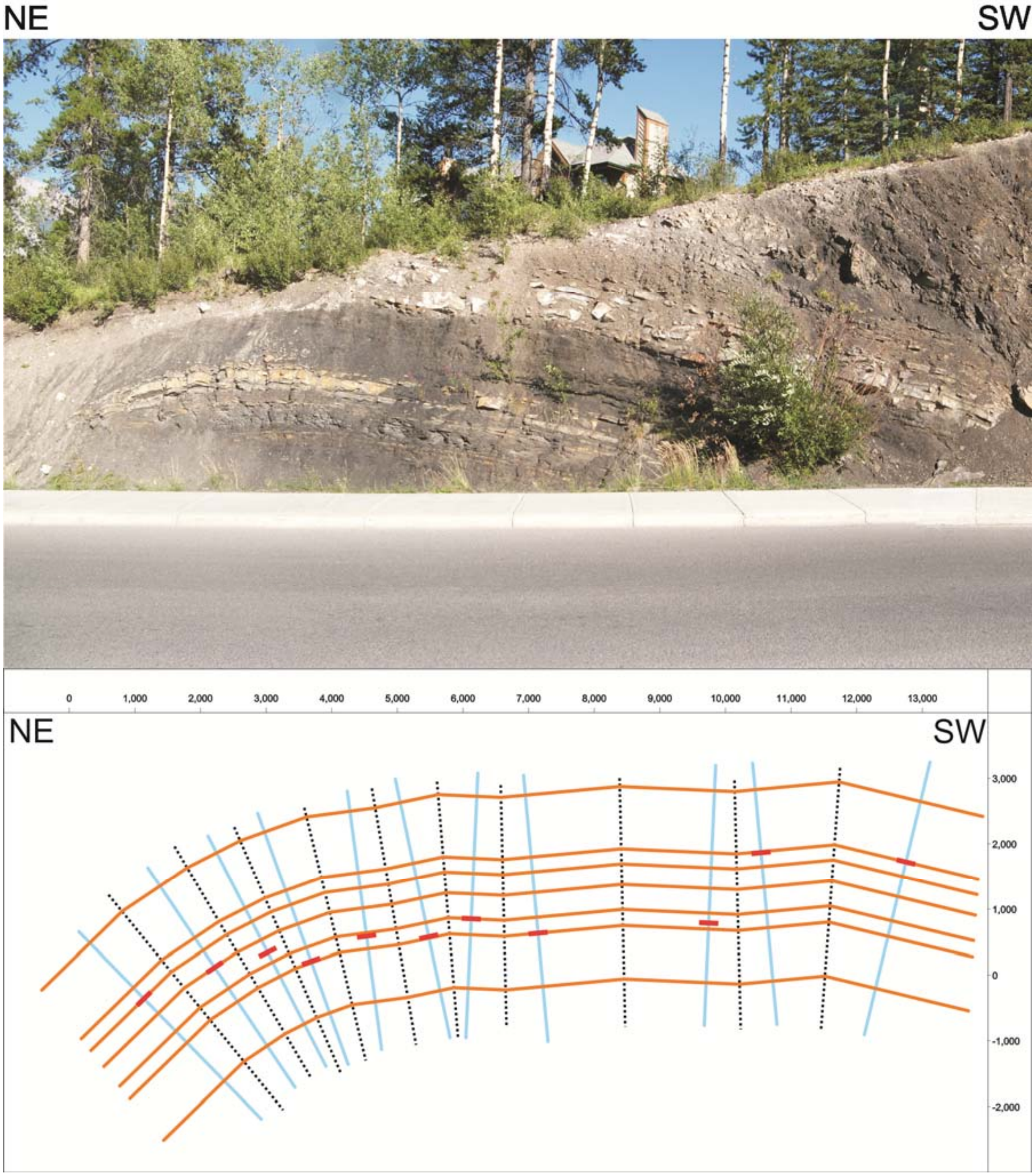

Figure 2-17: Canmore Nordic Centre Station 1
Station 1 is a gentle antiform with a broad hinge zone. Below the photograph is a down-plunge projected cross-section of the bedding measurements which are marked with red bars in the cross-section. The interpreted bedding is marked in orange, normals to bedding are marked in cyan and dip bisector isogon boundaries are dotted black. BH A and BH B (light grey and light yellow rectangles) are the synthetic boreholes that were drawn through this fold. The cross-section's scale is in millimetres.

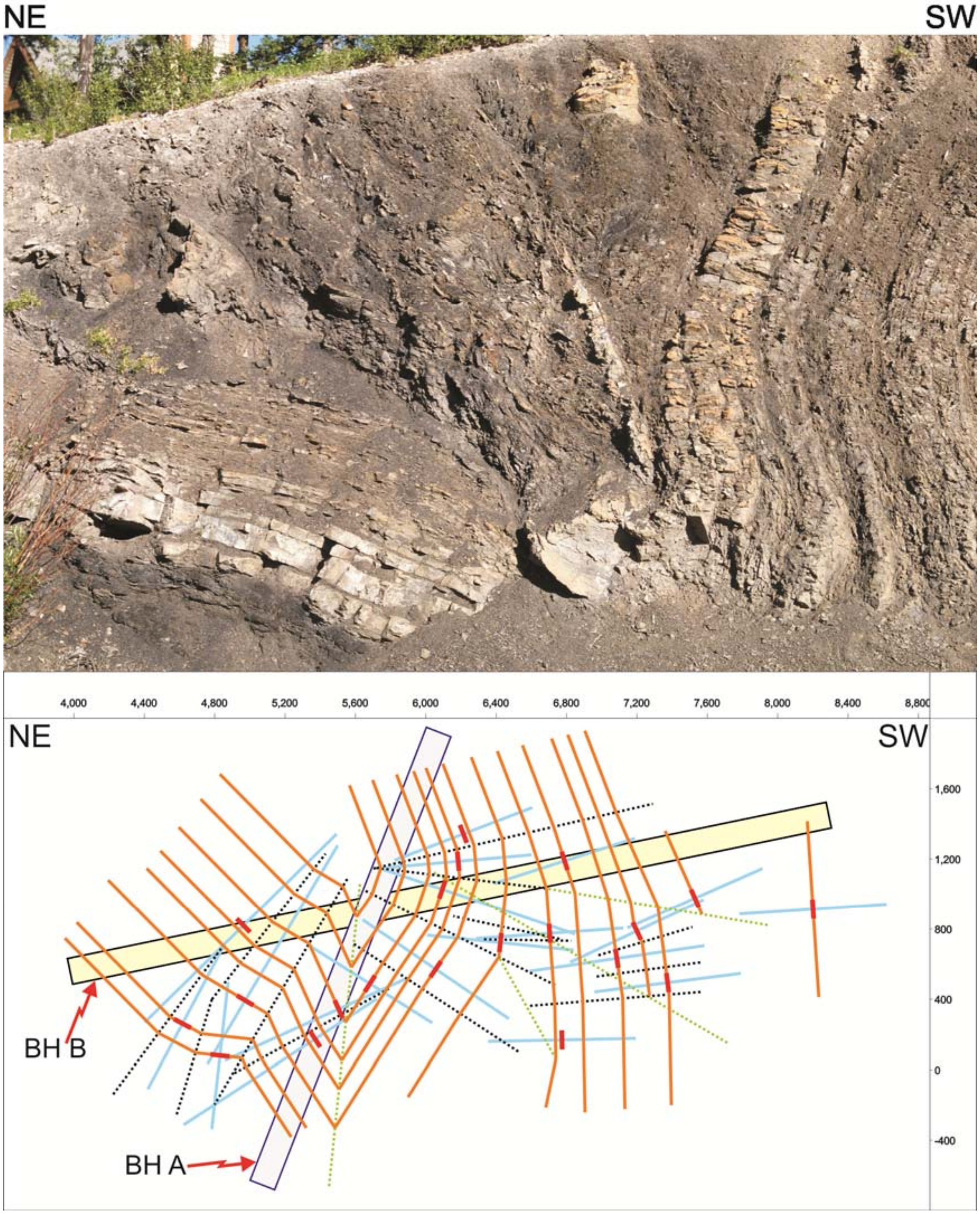

Figure 2-18: Canmore Nordic Centre Station 2
Station 2 is a close synform with a narrow hinge and gentle folding in the sub-vertical SW limb. Below the photograph is a down-plunge projected cross-section of the bedding measurements which are marked with red bars in the cross-section. The interpreted bedding is orange, normals to bedding are cyan and dip bisector isogon boundaries are dotted black. BH A and BH B (light grey and light yellow rectangles) are the synthetic boreholes that were drawn through this fold. The cross-section's scale is in millimetres.

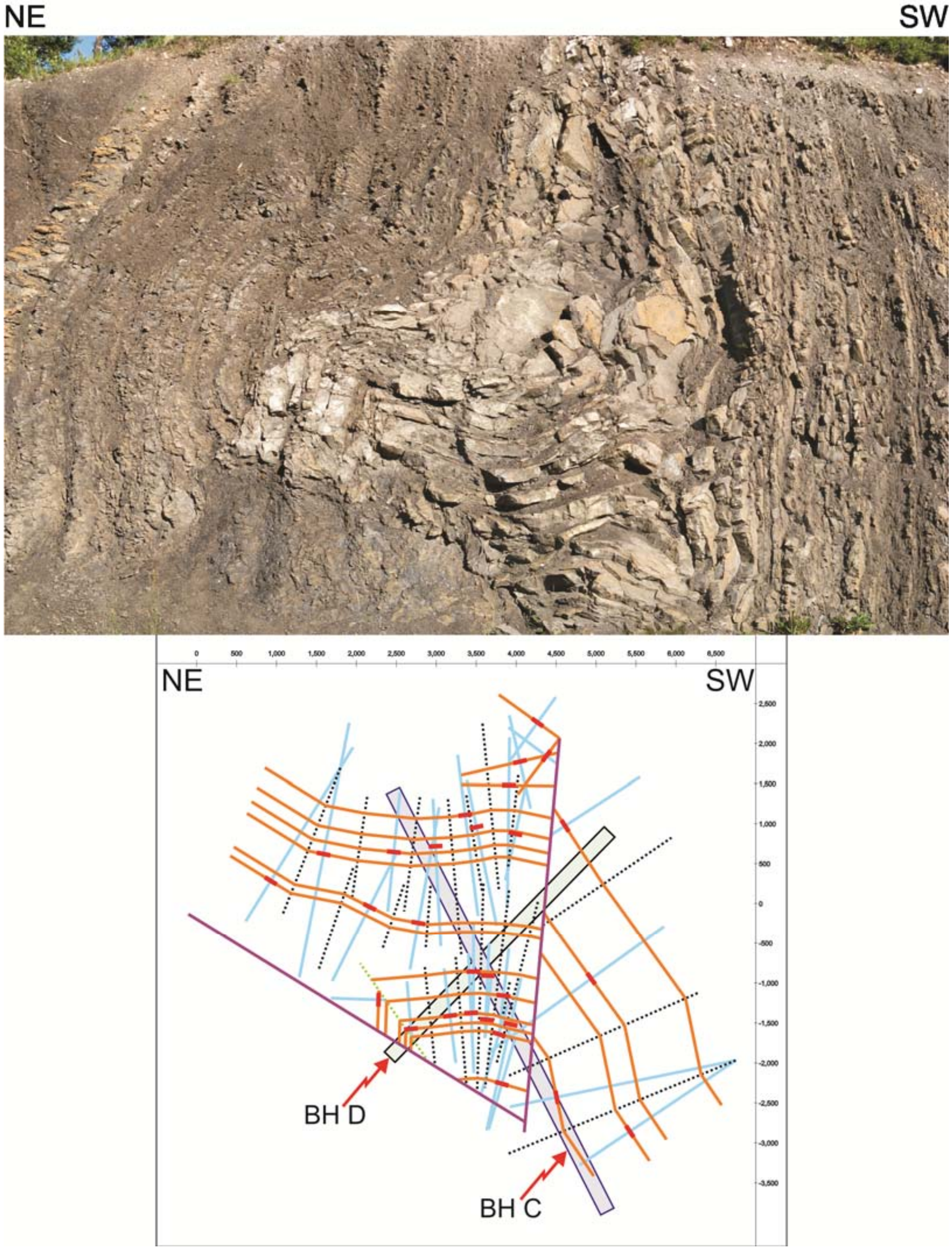

Figure 2-19: Canmore Nordic Centre Station 3
Station 3 is a fault-bounded antiform with a narrow hinge zone. Below the photograph is a down-plunge projected cross-section of the bedding measurements which are marked with red bars in the cross-section. The interpreted bedding is marked in orange, normals to bedding are marked in cyan and dip bisector isogon boundaries are dotted black. BH C and BH D (light purple and light green rectangles) are the synthetic boreholes that were drawn through this fold. The cross-section's scale is in millimetres.

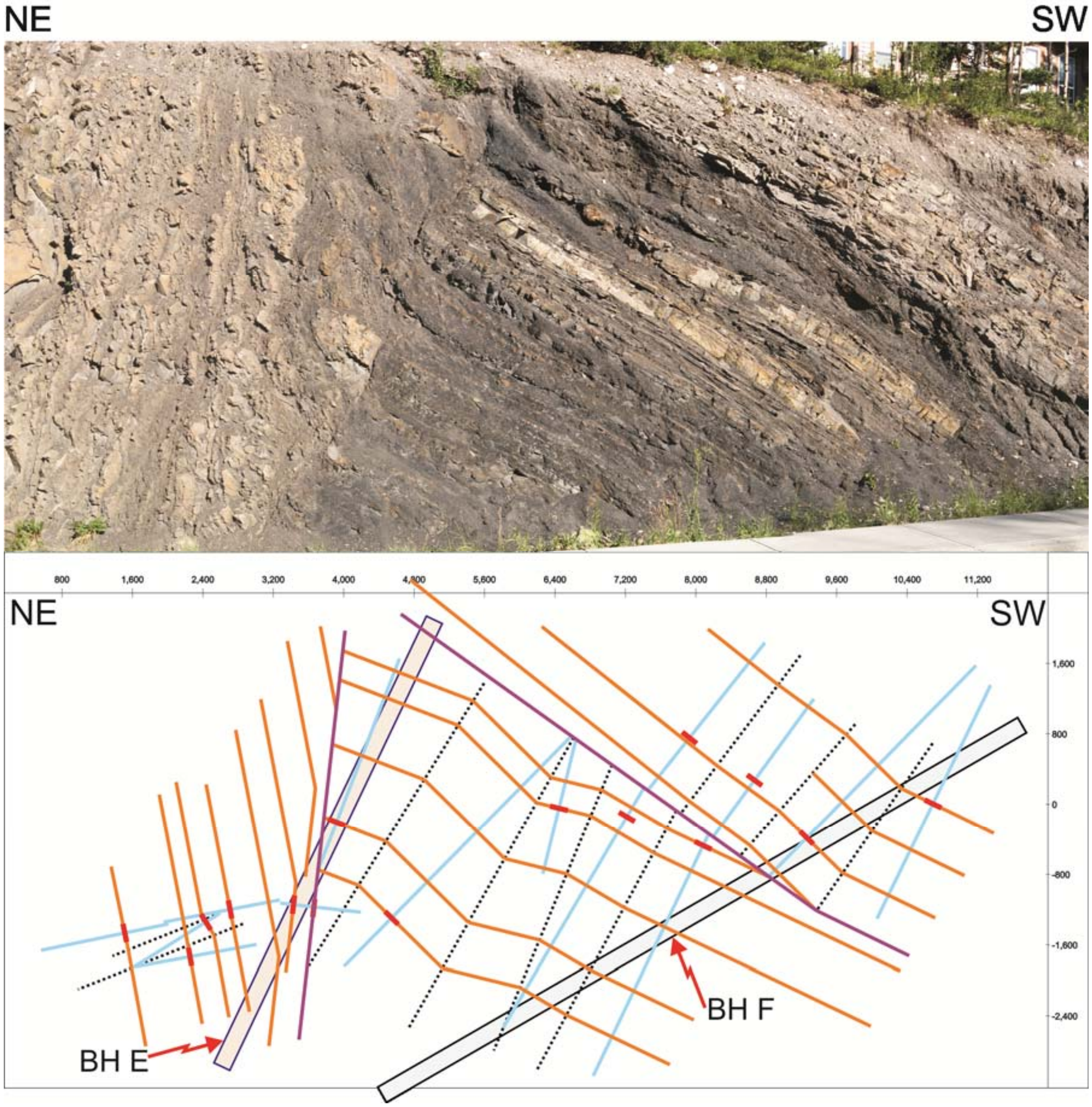

Figure 2-20: Canmore Nordic Centre Station 4
Station 4 includes a near-vertical fault on the left and a subtle, low angle thrust fault that repeats a tan coloured sandstone unit on the right with associated fault-bend folding. Below the photograph is a down-plunge projected cross-section of the bedding measurements which are marked with red bars in the cross-section. The interpreted bedding is marked in orange, normals to bedding are marked in cyan and dip bisector isogon boundaries are dotted black. BH E and BH F (light orange and light grey rectangles) are the synthetic boreholes that were drawn through this fold. The cross-section's scale is in millimetres.

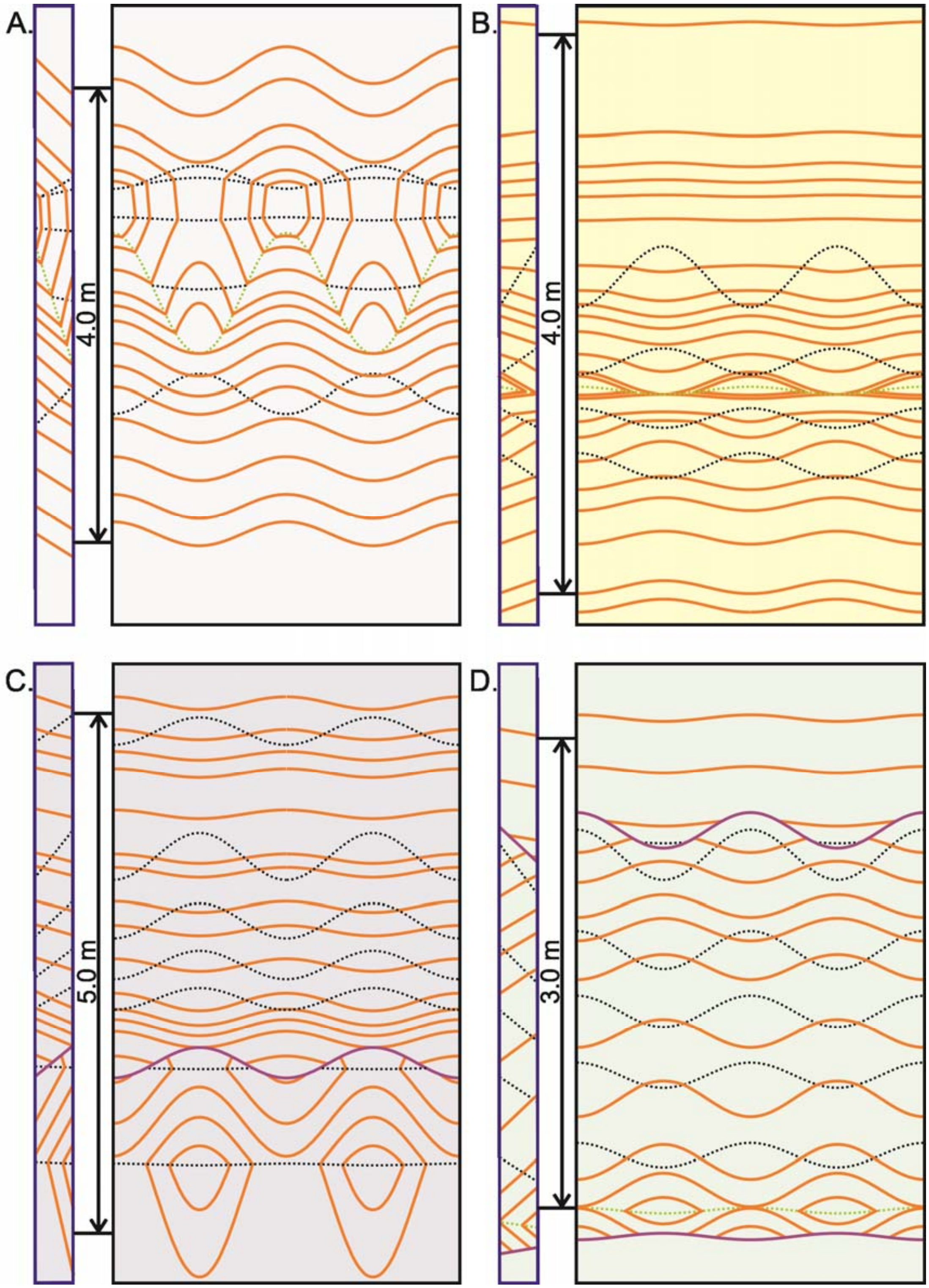

Figure 2-21: Canmore Nordic Centre synthetic borehole images, Stations 2 and 3
The first 4 synthetic borehole images (A, B, C and D) are displayed doubled (horizontal scale 0-720°) and are shown next to their corresponding slices of cross-section data. Bedding is orange, faults are purple and dip isogon boundaries are dotted black or green.

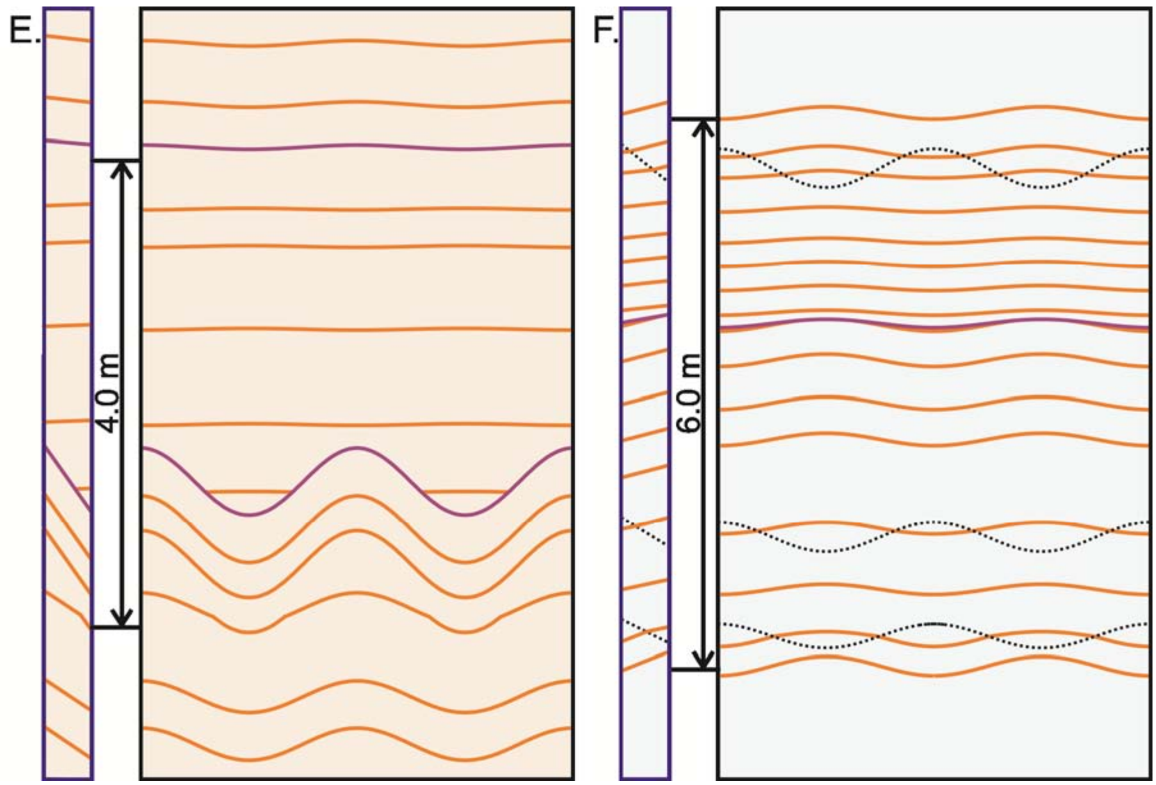

Figure 2-22: Canmore Nordic Centre synthetic borehole images, Station 4
The final two synthetic borehole images (E and F) are displayed doubled (horizontal scale 0-720°) and are shown next to their corresponding slices of cross-section data. Bedding is orange, faults are purple and dip isogon boundaries are dotted black or green.

complex structural deformation has occurred. It is not surprising then that this station's plunge direction is opposite to the other three stations as the stereonet could be thought of as an amalgam of the influence of several fold axes.

Projecting the measurements onto a common plane presented a pretty serious issue, especially for Station 3, resulting in some dispersion in the cross-sections. The basic assumption in simple geologic projections is that there is a common structural axis along which projections can be done. This was not the case. It is pretty clear that each individual fold, and even the inside versus the outside of an individual fold had different plunges and differences in their overall shape – conical versus cylindrical. Rather than try to resolve these differences, Station 3's data were projected parallel to the average structural axis for the domain and thus this cross-section is approximate.

This difference in plunges is predictable when one thinks about it. Smaller-scale folds would tend to have shorter lateral extents in the trend direction and thus would need to change laterally, either by changes in the associated fault boundary or, as is implied in this outcrop, by plunging away and transferring total compression between adjacent folds. This observation challenges whether one could use the Dale-Pumpelly Principle as a predictive tool. If smaller folds have fold axes that can plot with a significant scatter around the megascopic structural trend, one must conclude that one must use caution when using the structural scale interrelationship in industrial applications for predicting subsurface structural fold axes without a significant number of input measurements to mitigate the statistical variation.

The first borehole (Figure 2-21, A) shows a fold hinge "circle" combined with a tight angular fold hinge. The bottom portion of the fold is fairly tight as evidenced by a sharp change in sinusoid trough direction from steeply dipping in one direction to moderate in the opposite direction. If one were looking at this borehole cross-section alone, one could easily conclude incorrectly that it would most likely be due to a bedding-parallel shear event (because the bedding below and above the event are parallel) rather than a fold that results in inverted bedding. Instead, it represents a kink fold whose core is plastically deformed shale similar to that seen surrounding the Cascade outcrop.

The second image (Figure 2-21, B) shows a tight angular fold in a short and wide fold hinge "circle". To correctly interpret a borehole image that intersected this structure this way (and to correctly interpret the previous example), one would have to notice the beds folding in and out of the borehole and notice that the bedding below the structure was the inverted mirror image of the bedding above.

The third image (Figure 2-21, C) shows an open (long and narrow) fold hinge "circle" at the bottom of the image that truncates against a fault surface that also truncates the bedding above it. In this case, the dotted black dip isogon sinusoids obscure the resulting image somewhat as they reflect subtle changes in dip that would be measurable but would not be visible in a borehole image log as a kink plane per se.

The fourth image (Figure 2-21, D) shows a block of rock in the bottom three quarters that is bound by two faults with opposite dip directions. Above the lower fault, there is a tight drag fold that inverts the bedding before truncating against the fault plane. The upper fault plane just seems to truncate the bedding on both sides while at the same time being the locus for a reversal in dip direction.

The final two images show how fault intersections can be quite subtle in borehole image logs depending on the angle of intersection. The fifth image (Figure 2-22, E) has an obvious fault in the bottom half with bedding truncating at a high angle to a plane that is parallel to the underlying bedding while the fault in the top half (and the one in the last image (Figure 2-22, F)) would be difficult to discern because there is only a subtle change in dip orientation across the fault and, because bedding in both the hanging wall and footwall is flat dipping in a relative dip sense, there would be a lower likelihood of seeing clear bed truncation. Still, there would be a planar discontinuity that could have the full range of fault appearances (open, sealed with gouge or invisible) and would show a change in structural dip on the order of 10 degrees in magnitude.

CHAPTER 3: MESOSCOPIC STRUCTURES IN BOREHOLE IMAGE LOGS

Borehole image logs are almost exclusively acquired by companies conducting oil and gas exploration. A small subset of those imaged wells is in compressional structural regimes where mesoscopic folds (and other mesoscopic structures) are abundant and a very small subset of those image logs is available in the public domain for analysis. Fortunately, the British Columbia Ministry of Energy, Mines and Petroleum Resources requires oil and gas companies to submit a paper (and since 2009 a digital) copy of any borehole image log that is recorded in a well in B.C. and the Alberta Energy Resources Conservation Board has also added a similar requirement in early 2010. These paper prints are then made available upon request to the general public after the well becomes non-confidential (typically 1 to 2 years after drilling is complete) and thus can be scanned, their orientation information can be digitized and, with specialized software such as PetrisWINDS Recall, their bedding and fracture orientations can be interpreted. This process, if done correctly, yields a final product that is nearly indistinguishable from the original image processed from digital data from the field, thus it can be easier for an academic to get permission to study well data from B.C.

Case study: Image log from Talisman et al. Bullmoose D-77-D/93-P-3

This well is located at 55.06458° North Latitude, 121.451° West Longitude, about 520 km NNW of Edmonton, Alberta (Figure 3-1) and was drilled between late 1994 and early 1995 by Talisman Energy. It reached a depth of 4938 metres measured depth and has borehole images and dipmeter data from 482 to 4938 metres measured depth in the pilot hole and 4118 to 4674 metres measured depth in a sidetrack hole. Because the original image processing was done by the company I work for (HEF Petrophysical Consulting Inc.) and because the well has effectively been in the public domain for many years, I received permission from Talisman to use the original digital data rather than going through all the effort of scanning and digitizing the paper copy. This well was chosen because of the abundance and variety of different styles of mesoscopic folds, faults and foliations over a couple of kilometres of image log data from the pilot hole (the image quality in the sidetrack hole was reduced because one of the image pads was ripped off of the tool during logging and thus no examples are chosen from there).

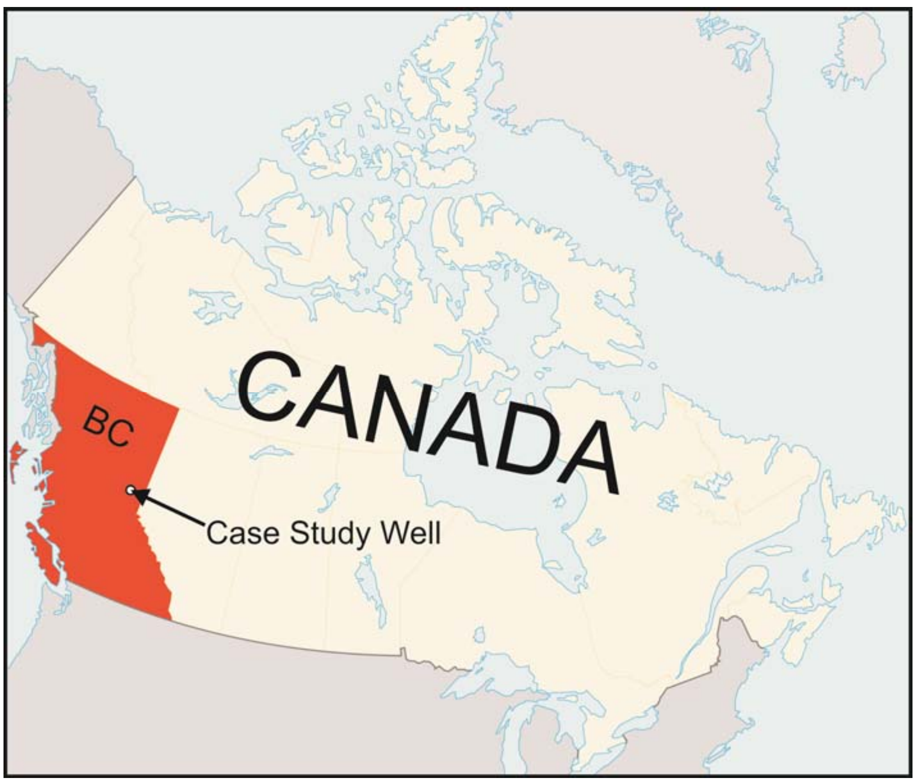

Figure 3-1: Location of case study well (modified from Wikipedia Commons).

Borehole image log interpretation issues

14 segments of image were selected to show some of the variety of fold and fault scales, styles and structural histories that are measurable in a borehole image log. For each

segment, the image data are shown twice in a double image log with the measured depth scale on the left, the interpreted sinusoidal bedding and fault segments marked in green and purple respectively, with the pair of vertical projection plane lines (see Chapter 1) superimposed on the image, near the middle. The right half of the image log is left uninterpreted so that one can see the source image data behind the sinusoids. Positioned to the right of each image log is a grey half cylinder that represents the true scale of the borehole and shows how the sinusoidal measurements project onto that plane in a cross-sectional view. Where it helps to outline how a given feature would look in a larger section (such as in an outcrop), the bedding and fault data are projected laterally from the known data using dip isogon projection. In the cross-section, any interpolated, extrapolated or inferred feature that was not directly measured in the image log is shown with a dotted line while the measured ones are shown as solid lines. As in the borehole image track, bedding planes in the cross-sections are outlined in green and faults are shown in purple. These cylinders are observed to change in width from page to page for two reasons:

The first is because there are two different bit sizes in these image log segments, which also accounts for why the image pad widths are narrower for the first seven images and wider for the last seven. The image tool's eight pads cover the same amount of borehole circumference (about 50 cm) regardless of the bit size so when the bit changed from 333 mm in the shallower images (having a hole circumference of 104.6 cm) to a bit size of 234 mm (having a hole circumference of 73.5 cm) the image pad coverage increased from about 48% to about 68%.

The second reason for the variance in the cylinder width is that the number of metres of borehole image log in each segment is not consistent. This was done because the structures have different extents and scales ranging from several centimetres to several metres. Thus, each image log is shown at a different vertical scale (marked by the depth track on the left) and each cross-section must be drawn at its own scale with no vertical to horizontal distortion to yield true dips. The horizontal axis on the borehole image log is shown in degrees, rather than in a fixed length scale as is customary for image logs. This means that there are varying levels of horizontal to vertical length proportionality in these borehole images but that is also the custom in image logs as the track widths are fixed regardless of the borehole being in gauge (i.e. equal to bit size), smaller than bit size due to hole collapse or mud filter cake or enlarged because of washout, breakout or high-side erosion in a dog leg interval. Basically, in addition to the bit size effect, the borehole width change is proportionate to the change in vertical scale of its image log.

Mesoscopic structure interpretations from borehole images

Each of the following images (Figures 3-2 to 3-15) shows an example of a mesoscopic structure from the case study well. There are a large number of image segments and interpreted borehole-derived cross-sections and to keep the text clear, each image has a caption associated with it explaining the interpreted bed forms and any special issues with that image's interpretation. These examples will be compared to the cross-section and synthetic borehole image logs from Chapter 2 to prove that features of the scale observed in the outcrop study are also seen in the subsurface (as they should be), that they are measurable and using the transformation techniques outlined in Chapter 1 they

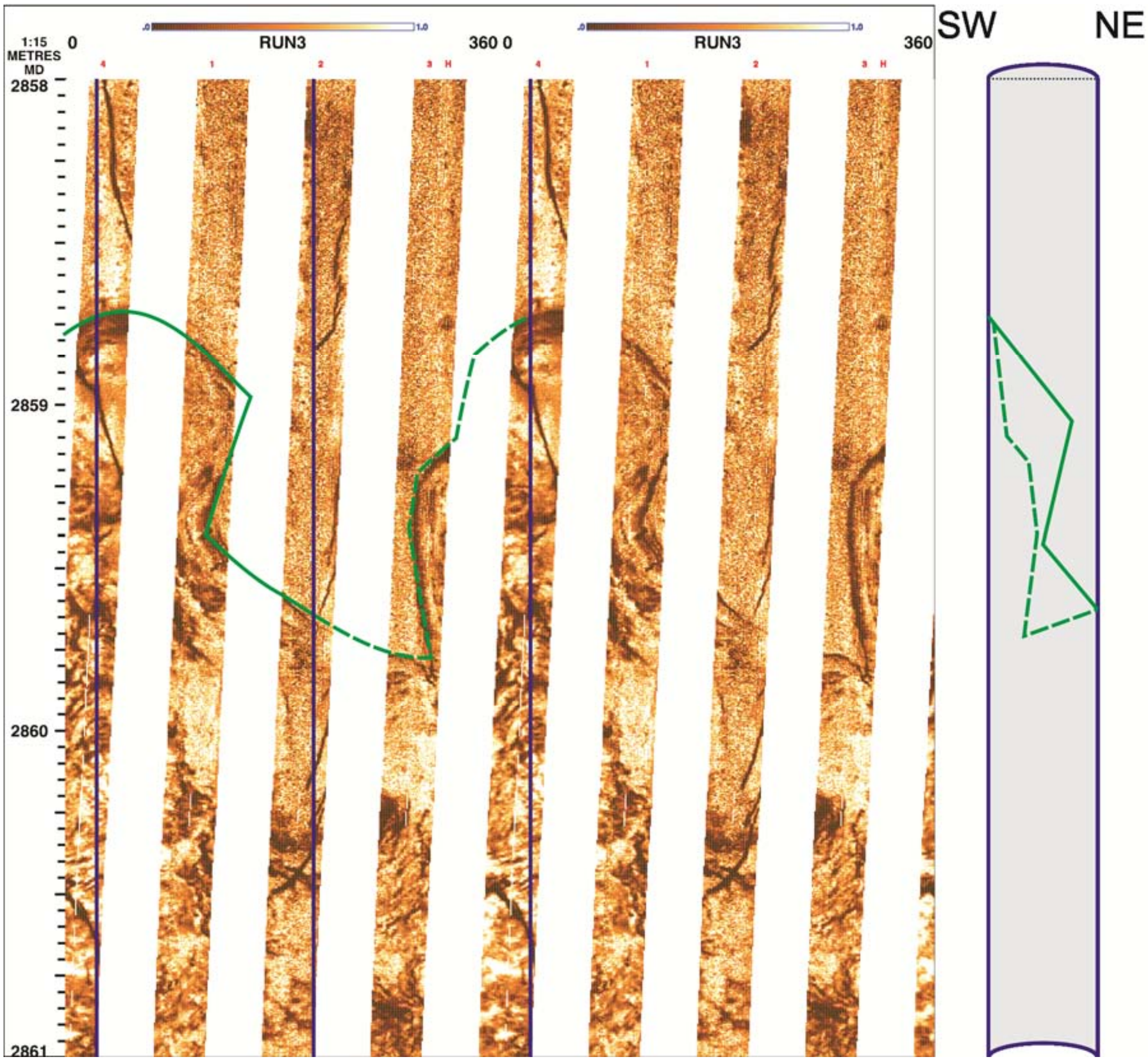

Figure 3-2: Borehole image 2858-2861 metres (A)
The interpreted bed (green) seen in this image is highly contorted such that there is no symmetry between the eastern and western intersections of the cylinder and the bed. Because of this lack of symmetry, each half of the borehole was interpreted separately (the solid green versus long dashed green lines) and requires two superimposed cross-sections. To get a structure of this sort, there must be some distortion out of the plane of the primary folding (i.e. oblique to the fold axis) so this could be considered evidence of multiple folding phases or, more likely, a rapid lateral change in fold plunge.

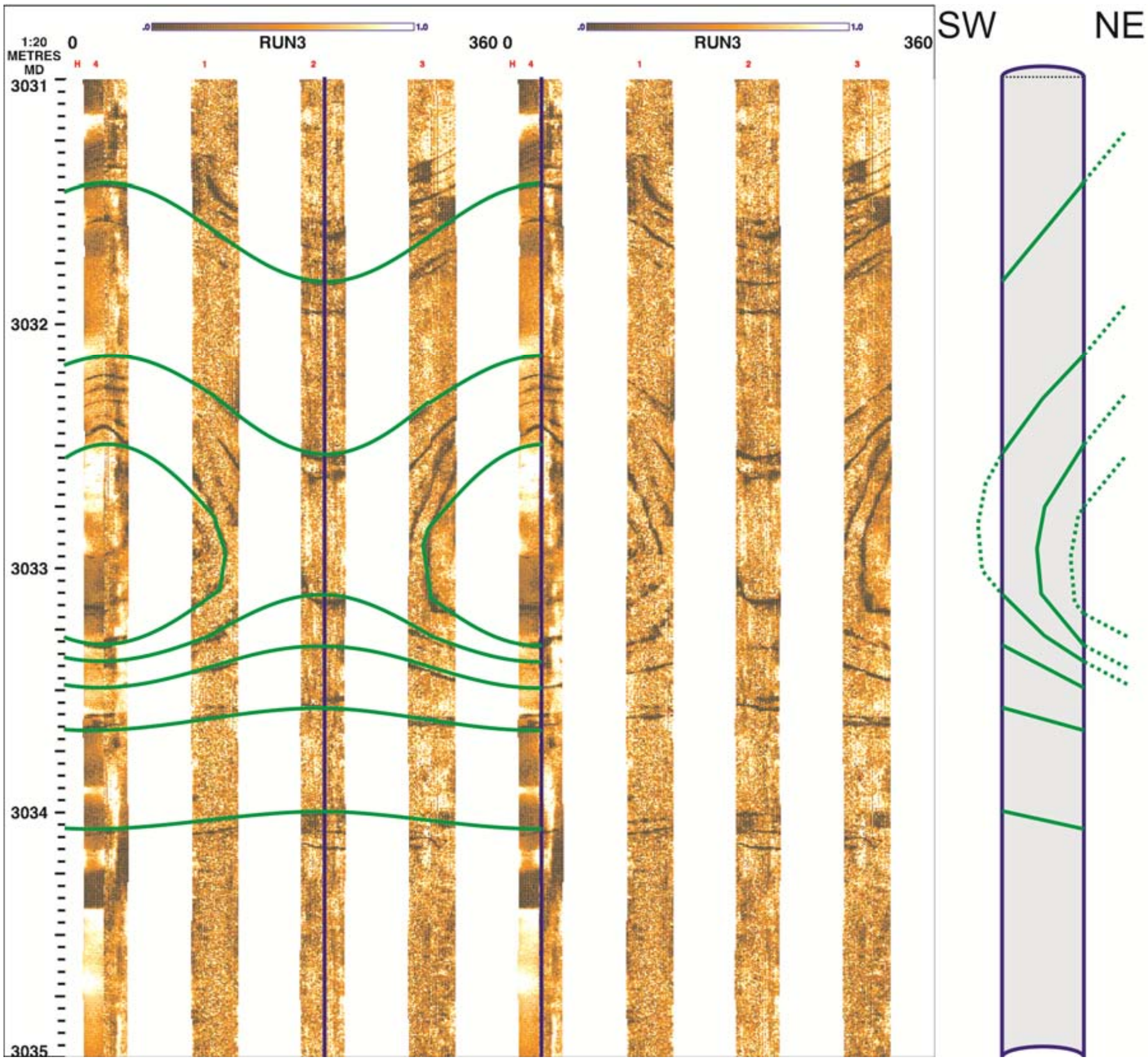

Figure 3-3: Borehole image 3031-3035 metres (B)
This interval shows thin conductive (dark coloured) beds that bend in and out of the borehole making a distorted circular shape typical of borehole images where the borehole intersects the fold hinge surface at a close to perpendicular angle. The side-on view of the borehole, on the right, clearly shows that one half of the beds here are inverted such that down-section is up in a measured depth sense. There is no faulting seen nearby and it appears that the lower limb is thinned somewhat relative to the upper limb.

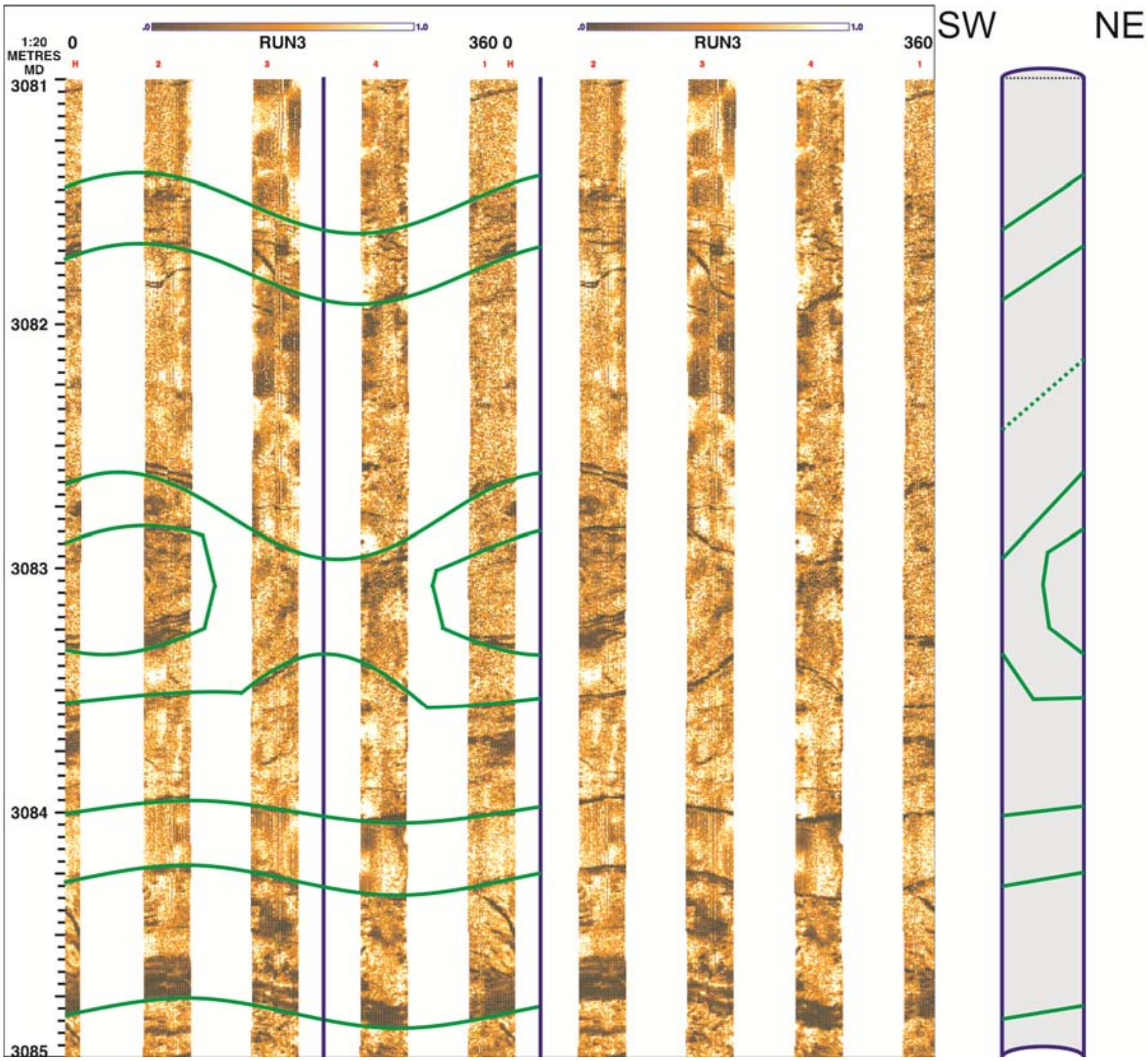

Figure 3-4: Borehole image 3081-3085 metres (C)

This interval shows thin conductive (dark coloured) beds that bend in and out of the borehole making a distorted circular shape typical of a simple fold in a borehole image. The bedding dips above and below the fold hinge are very similar in the image logs and side-on view of the borehole, and there is no apparent repetition of bedding below 3083.8 metres so there may be an unseen or bedding parallel fault (likely) below the fold hinge near 3084 metres.

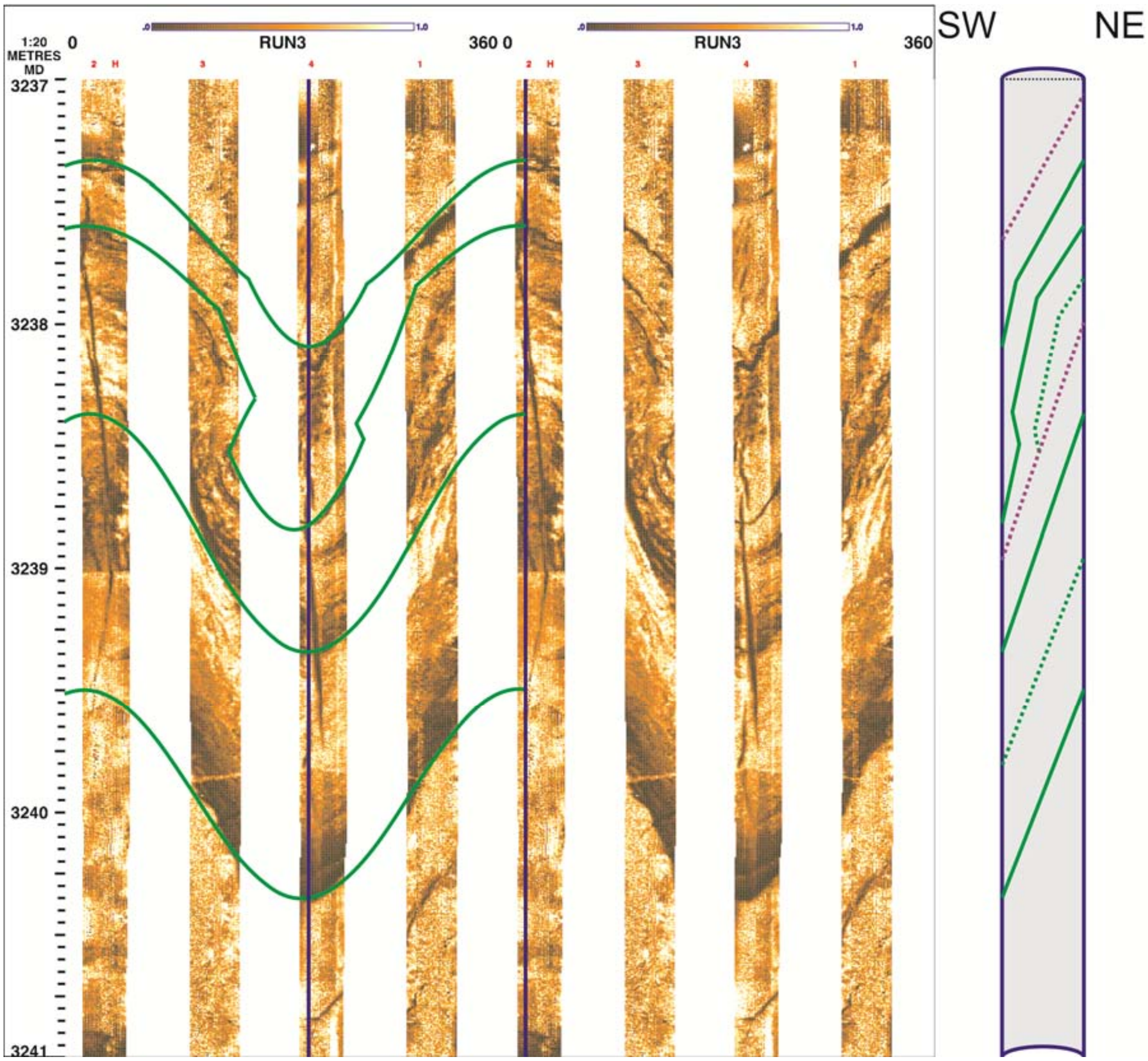

Figure 3-5: Borehole image 3237-3241 metres (D)

This interval shows a somewhat subtle low amplitude pop-up style fold that causes the thin conductive (dark) beds to fold in and out of the borehole. Because of the change in thickness between the bed whose trough is at 3239.3 metres and the folded bed whose peak is at 3237.6 metres (and whose trough is at 3238.8 metres), a dotted purple thrust fault is inferred in the borehole cross-section on the right. As drawn, this would be a fault in the upper ramp position in a ramp-flat-ramp style thrust fault.

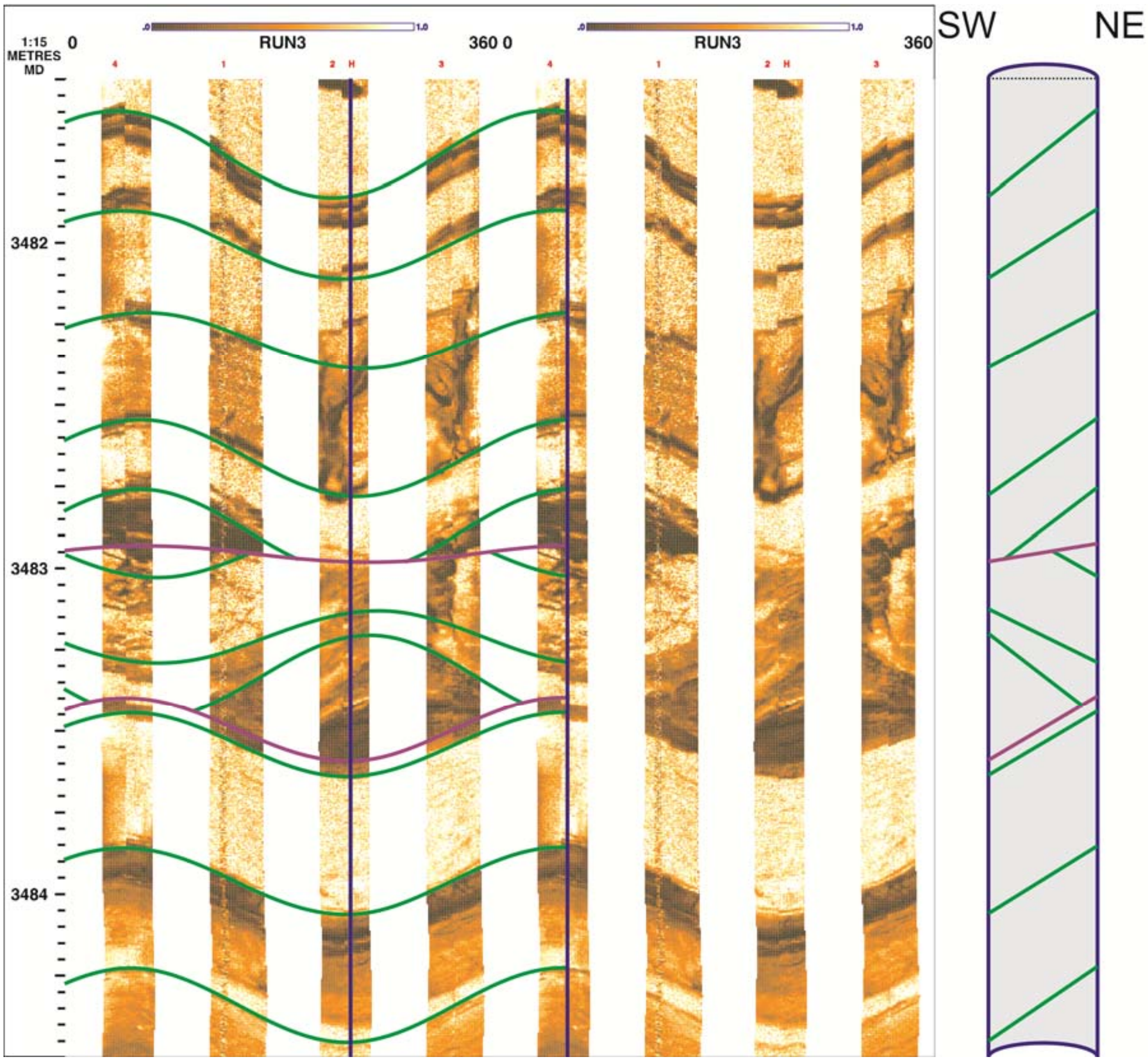

Figure 3-6: Borehole image 3481.5-3484.5 metres (E)
This interval shows a segment of bedding that is flipped over and truncated above and below by a pair of faults. The faults (purple) are inferred by the presence of truncated bedding (green), with little open aperture or gouge seen. Very little bending is seen adjacent to these faults meaning that this could have been a paired kink fold structure of some kind where the fault planes cut through the fold hinges or obliquely cut any bending zones which were left behind somewhere up or down-throw from the portion of the structure intersected by the borehole.

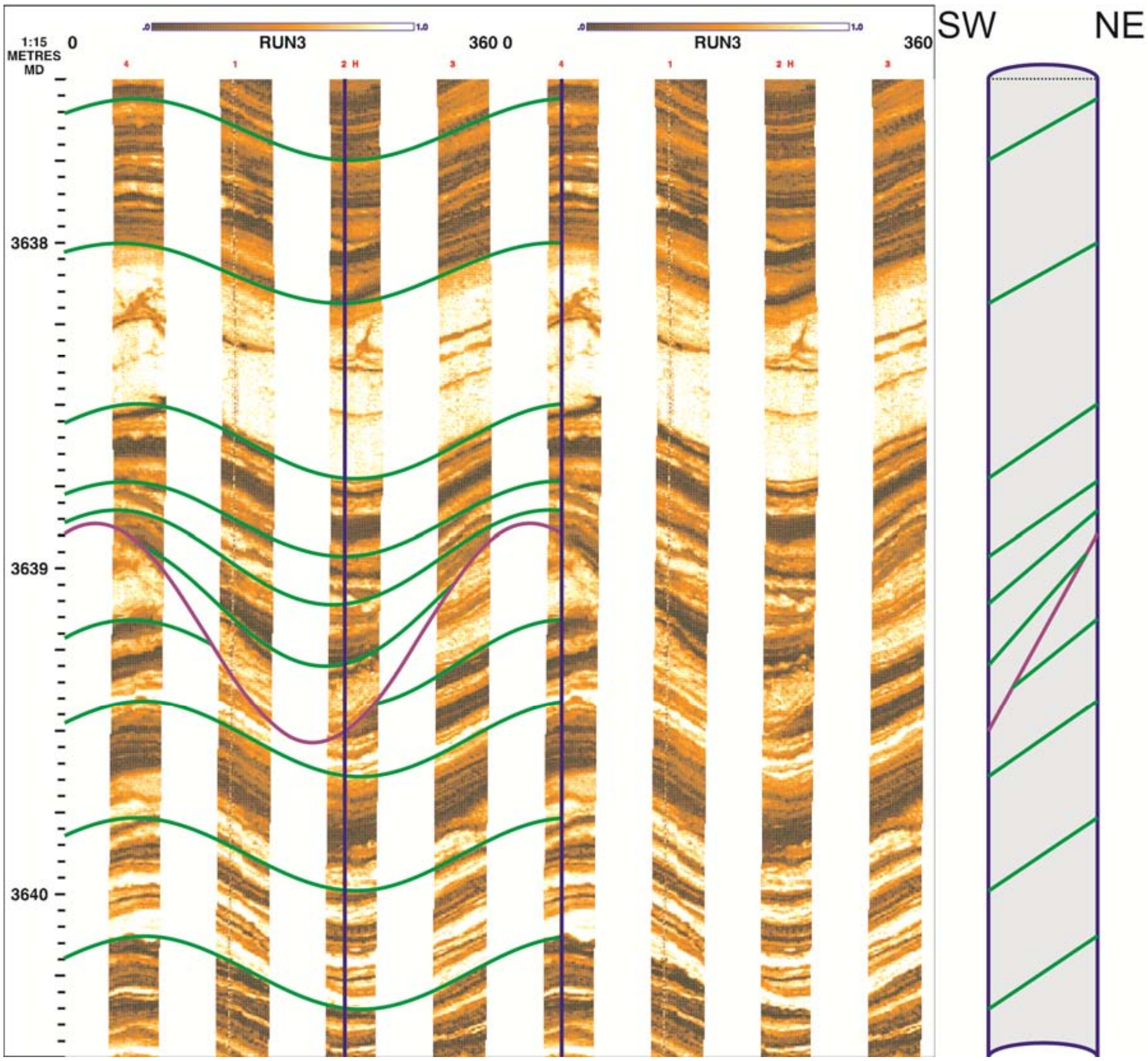

Figure 3-7: Borehole image 3637.5-3640.5 metres (F)
This interval shows a simple fault drag structure in an interbedded sequence that only disturbs the bedding (green) for less than a metre above the fault (purple). The fault plane itself is not seen as a discrete image feature (neither a conductive or resistive trace, implying that there was never open aperture or a significant interval of fault gouge) but is instead seen where the footwall bedding is truncated against a sinusoidal surface as is most clearly visible in the second image pad pair from the right (near the bottom of the fault trace). Because of a lack of bedding repetition, the fault is likely a normal fault.

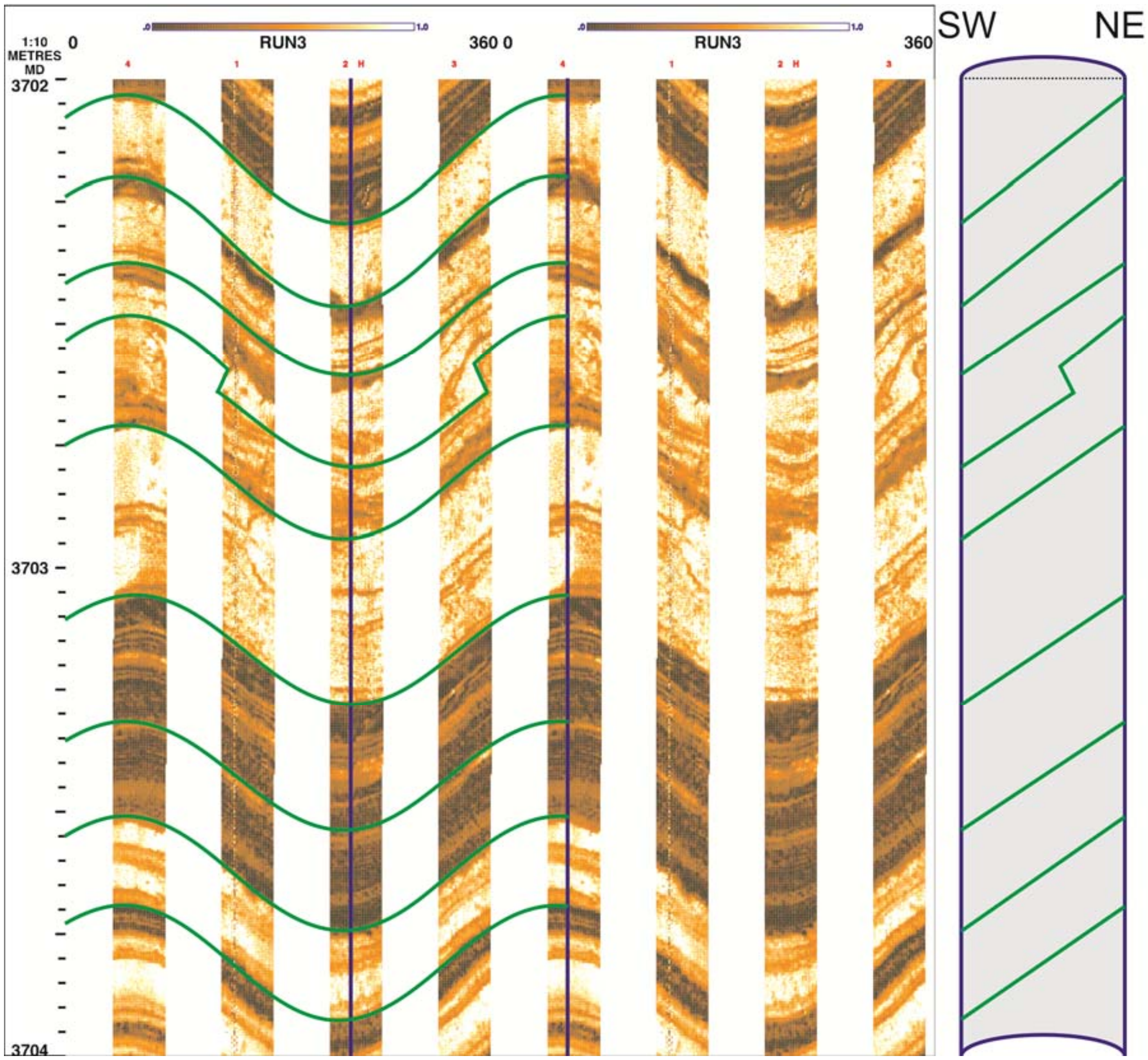

Figure 3-8: Borehole image 3702-3704 metres (G)

This interval shows a very small folded bed whose total contraction is less than 20 centimetres. There is very little disturbance above or below this fold so it could be part of a set of low amplitude crenulations whose wavelength is larger than the borehole size. There may be a second similar feature on the rightmost pads at 3703 metres, but it was difficult to trace an individual bed in that interval so it was left uninterpreted. While a feature such as this is small, it does give a sense of the bedding parallel shear direction being counterclockwise in the cross-sectional view of the borehole.

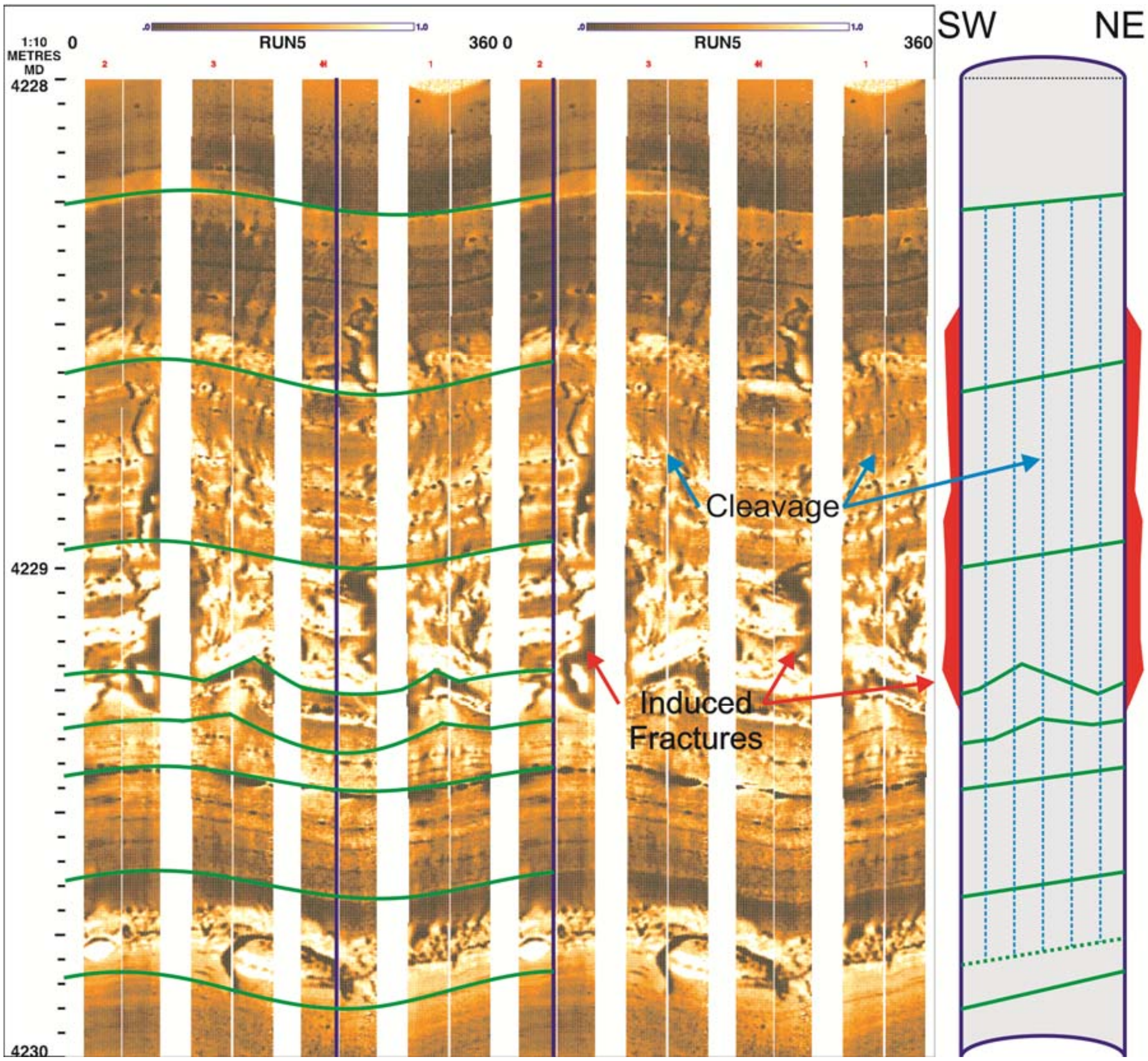

Figure 3-9: Borehole image 4228-4230 metres (H)

This is another very subtle less than 10 cm amplitude fold whose vergence is clockwise in the cross-sectional view. The borehole-parallel (vertical) dark features seen throughout this interval are likely cleavage planes due to low-grade metamorphism. They are parallel to each other within each bed and are seen to be offset across bedding planes, implying that they formed at an earlier time and then were distorted by the same sort of bedding-parallel slip that led to and accommodates the folding. The cleavage features are most easily visible in the NW-SE direction and are not to be confused with the dark (open aperture) drilling-induced fractures that are oriented parallel to the maximum horizontal stress axis, NE-SW. Dashed blue lines are added to the cross-section to represent the cleavage planes which extend perpendicular to the cross-section plane and red induced fractures are shown indicating propagation parallel to the cross-section.

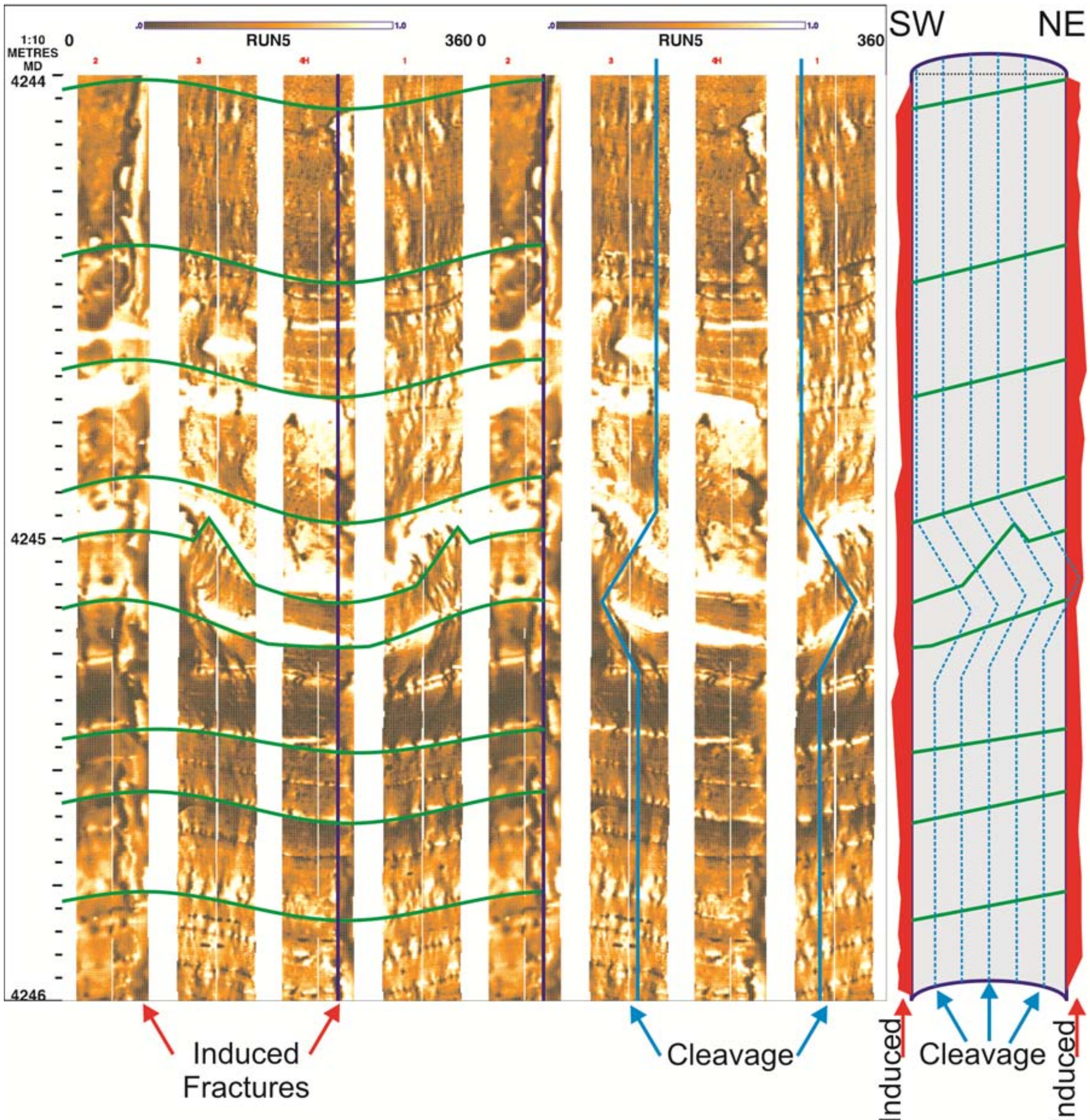

Figure 3-10: Borehole image 4244-4246 metres (I)
This interval shows another very subtle >10 cm amplitude fold whose vergence is clockwise in the cross-sectional plane. The cleavage planes (the vertical striping) are becoming dominant in this interval and the presence of resistive (light coloured) bands implies that in addition to fracture planes, there has been some remineralization at some time in the past. Note that the cleavage planes are sub-parallel to the wellbore, and at 4244.7-4245.3 metres can be seen to refract across the bedding. The cleavage features are most easily visible in the NW-SE direction and are not to be confused with the dark (open aperture) drilling-induced fractures that are oriented parallel to the maximum horizontal stress axis, NE-SW. Dashed blue lines are added to the cross-section to represent the cleavage planes which extend perpendicular to the cross-section plane and red induced fractures are shown indicating propagation parallel to the cross-section

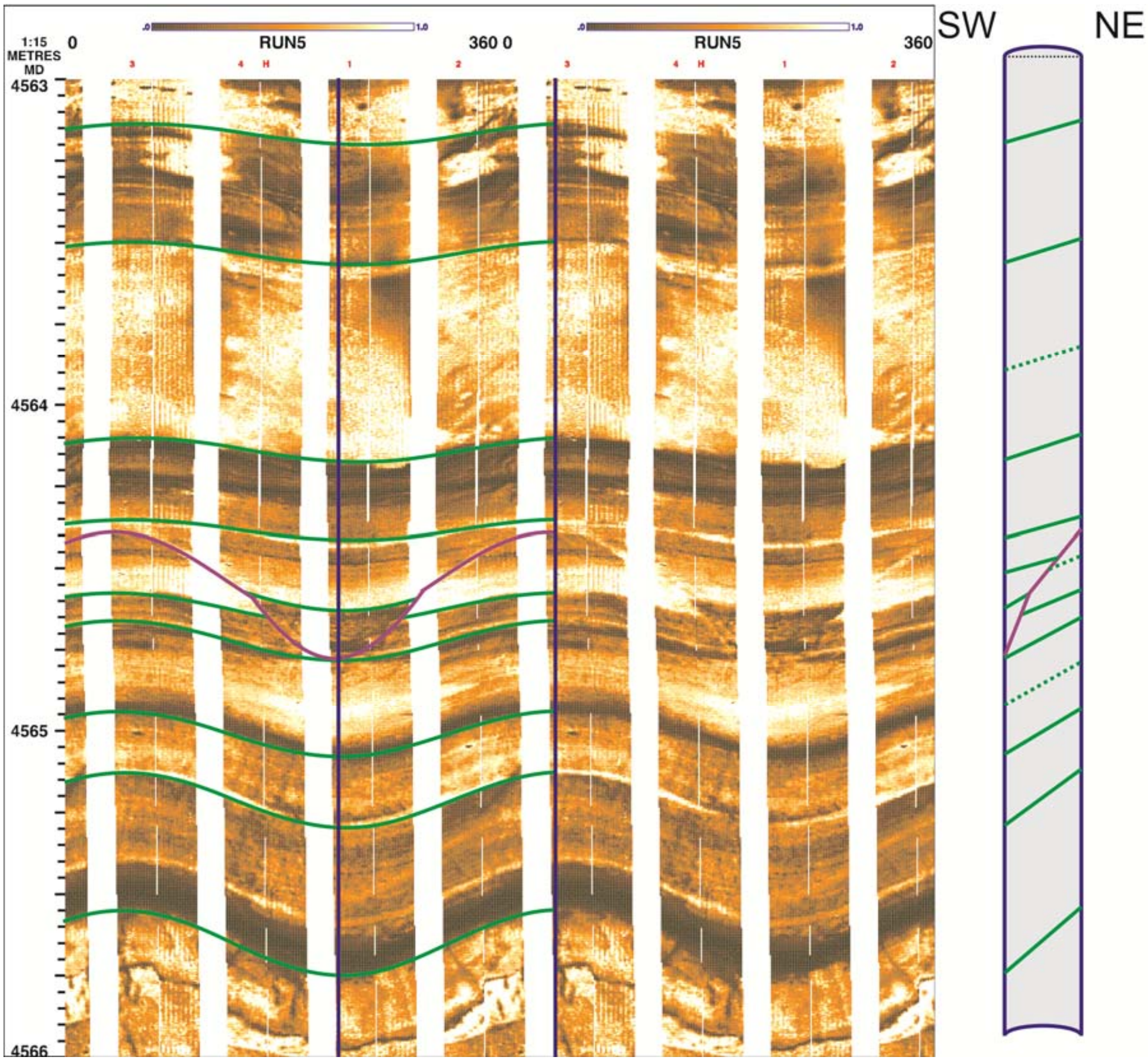

Figure 3-11: Borehole image 4563-4566 metres (J)
This interval shows a simple non-planar fault (purple) with a fault-bend-fold structure that only disturbs the interbedded stratigraphy (green) for less than a metre above it. The fault plane itself is visible as a resistive (white) trace, meaning that either the fault plane itself once had open aperture and has since been sealed shut through precipitation of a resistive mineral such as calcite or quartz or (more likely) the fault plane has a small gouge zone that is full of powdery resistive material. The bedding is seen to repeat with a displacement of about 5 cm.

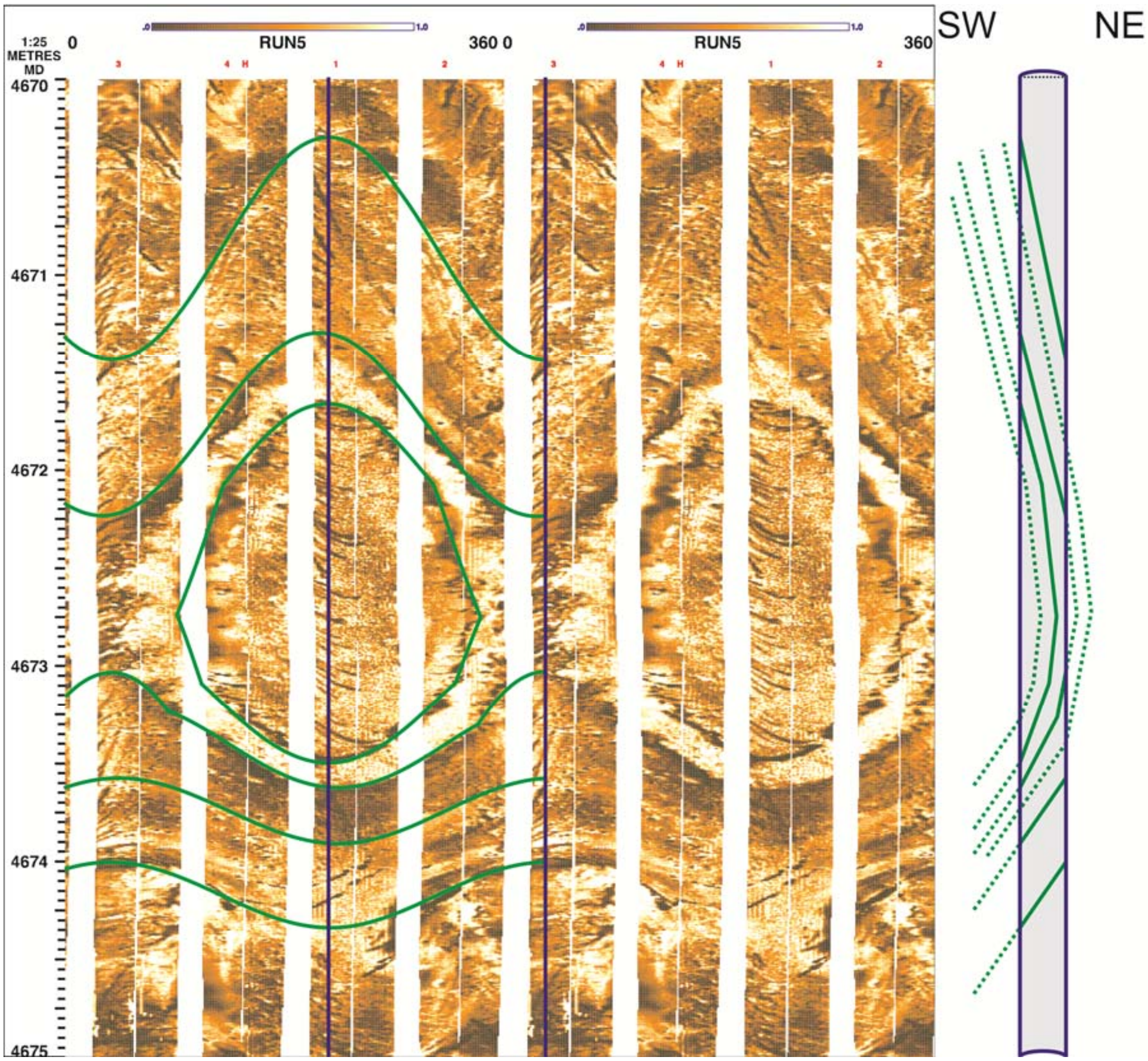

Figure 3-12: Borehole image 4670-4675 metres (K)
This interval shows an uncomplicated open fold structure with a near-horizontal fold hinge where the bedding is delineated by a pair of bedding-parallel stylolites (the dark, wavy egg-shaped features in the centre of the image) rimming a light coloured resistive bed. Because the borehole intersection is at a very small angle to bedding that is near-vertical in dip, this image is identical to how an image would look if a horizontal well intersected an open fold with a vertical hinge plane. This interval is the one used in Figures 1-7 and 1-8, providing a comparison of full versus cropped sinusoidal segments.

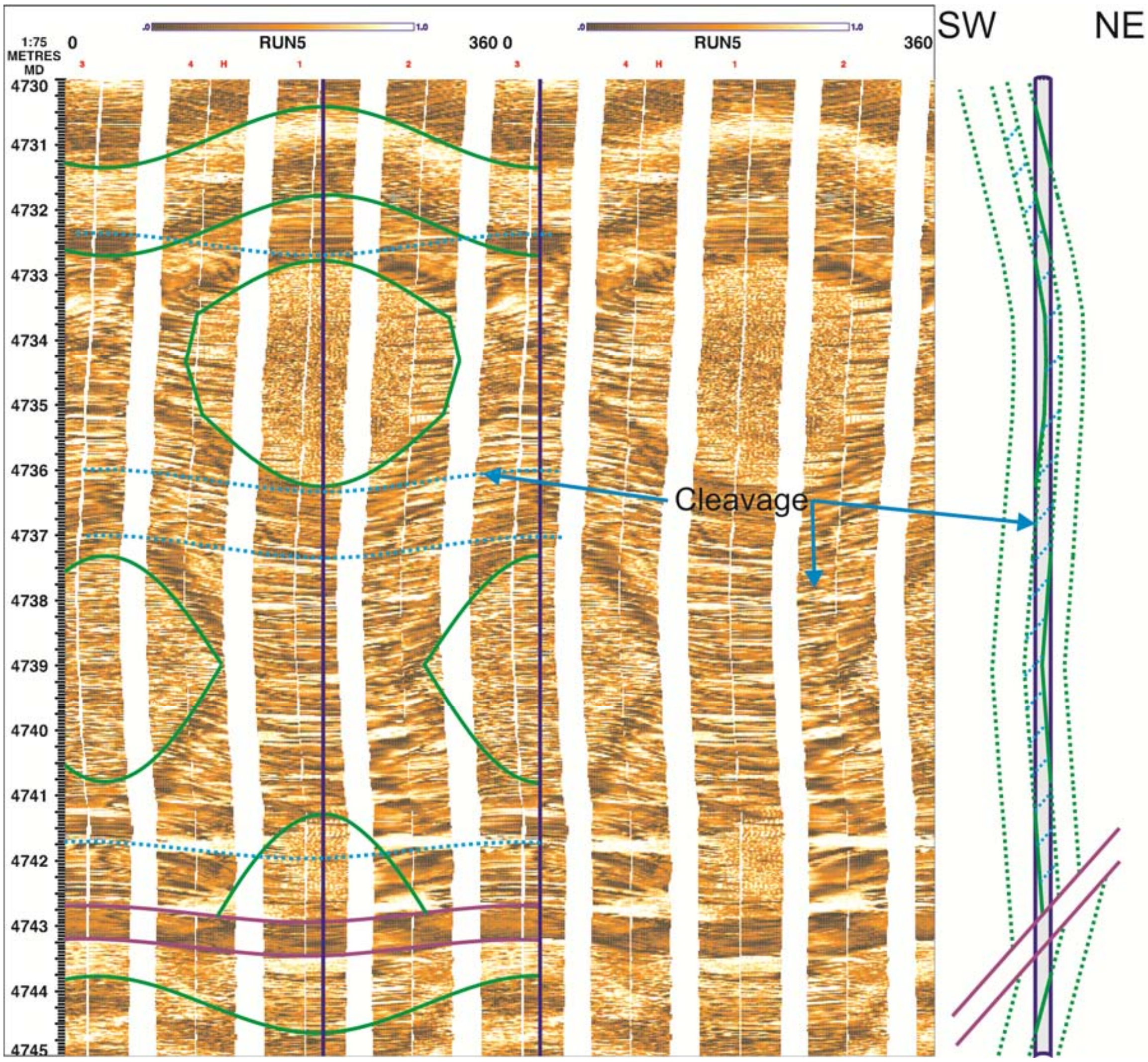

Figure 3-13: Borehole image 4730-4745 metres (L)

This interval shows another small angle intersection of a set of undulating open folds truncated at a fault plane. The bedding in the middle of this interval is quite indistinct so one has to infer the presence of bedding planes by the presence of a compositional boundary between the highly resistive (anyhydrite or limestone) beds that form the cores of these structures and the subhorizontally striped (likely foliated) and more conductive beds that form an X shape centred at 4739 metres. The cleavage planes are highlighted with a number of dashed blue sinusoids on the borehole image log and by corresponding dotted blue lines on the cross-section, indicating that the foliation is strongest within the confines of a single bed that folds in and out of the borehole. A fault zone is interpreted at 4743 metres between a pair of planar discontinuities that truncate bedding. The wellbore is not deviated to a large degree so the bedding planes are sub-vertical and the cleavage planes were likely rotated into this shallow orientation.

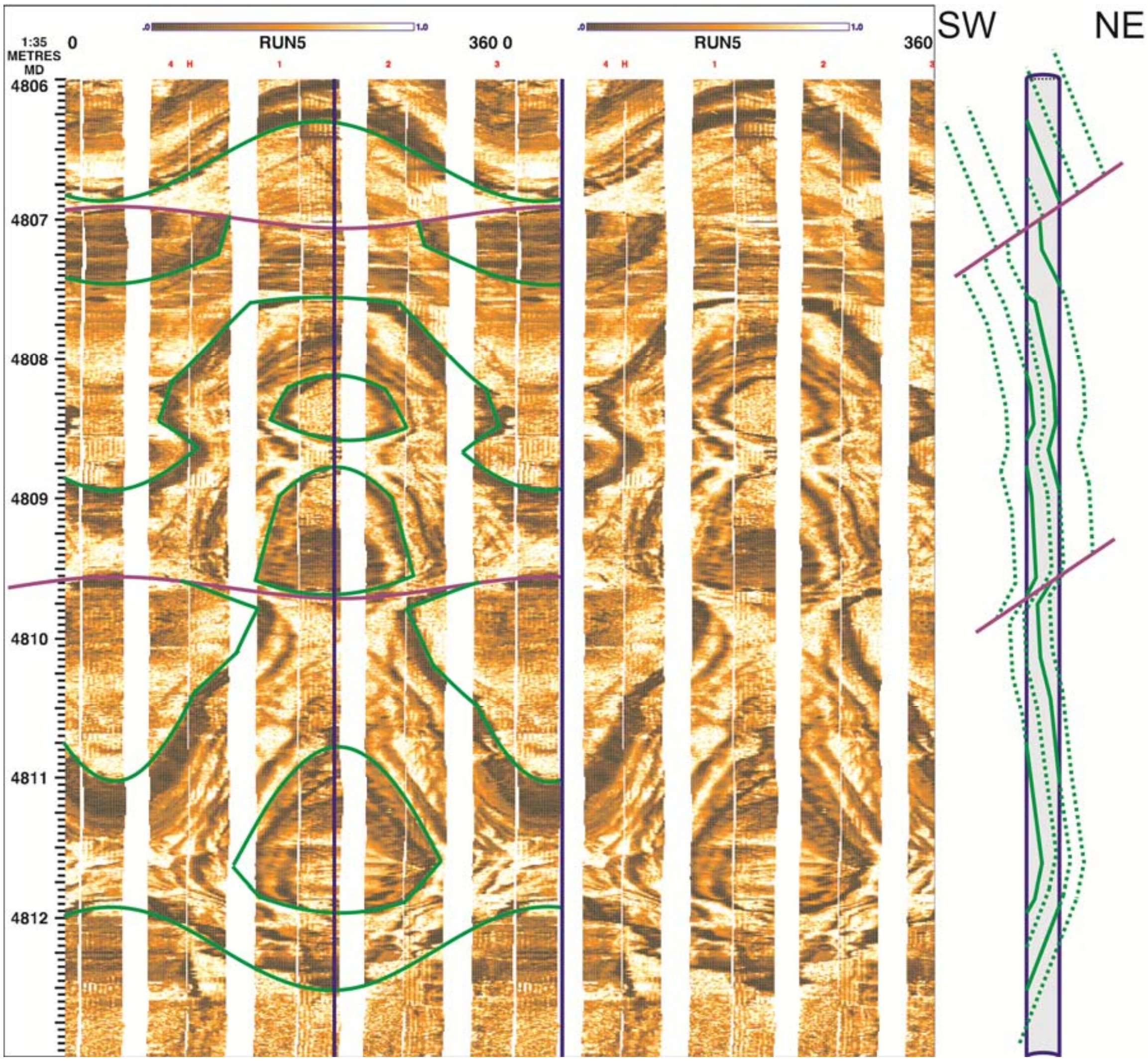

Figure 3-14: Borehole image 4806-4813 metres (M)

This interval shows a similar kind of structure as the previous figure, but compounded as a set of undulating folds and fault-bound blocks. The fault planes in this case (at 4807 and 4809.6 metres) are resistive features implying that they have been healed or are full of resistive fault gouge. While the folding in this image is not very large in scale (amplitudes in the range of 15 centimetres), the bedding drag adjacent to the faults implies that the fault plane vergence is clockwise, and we can conclude that the steeply dipping bedding panel was likely thrust into this position before the smaller faults were formed.

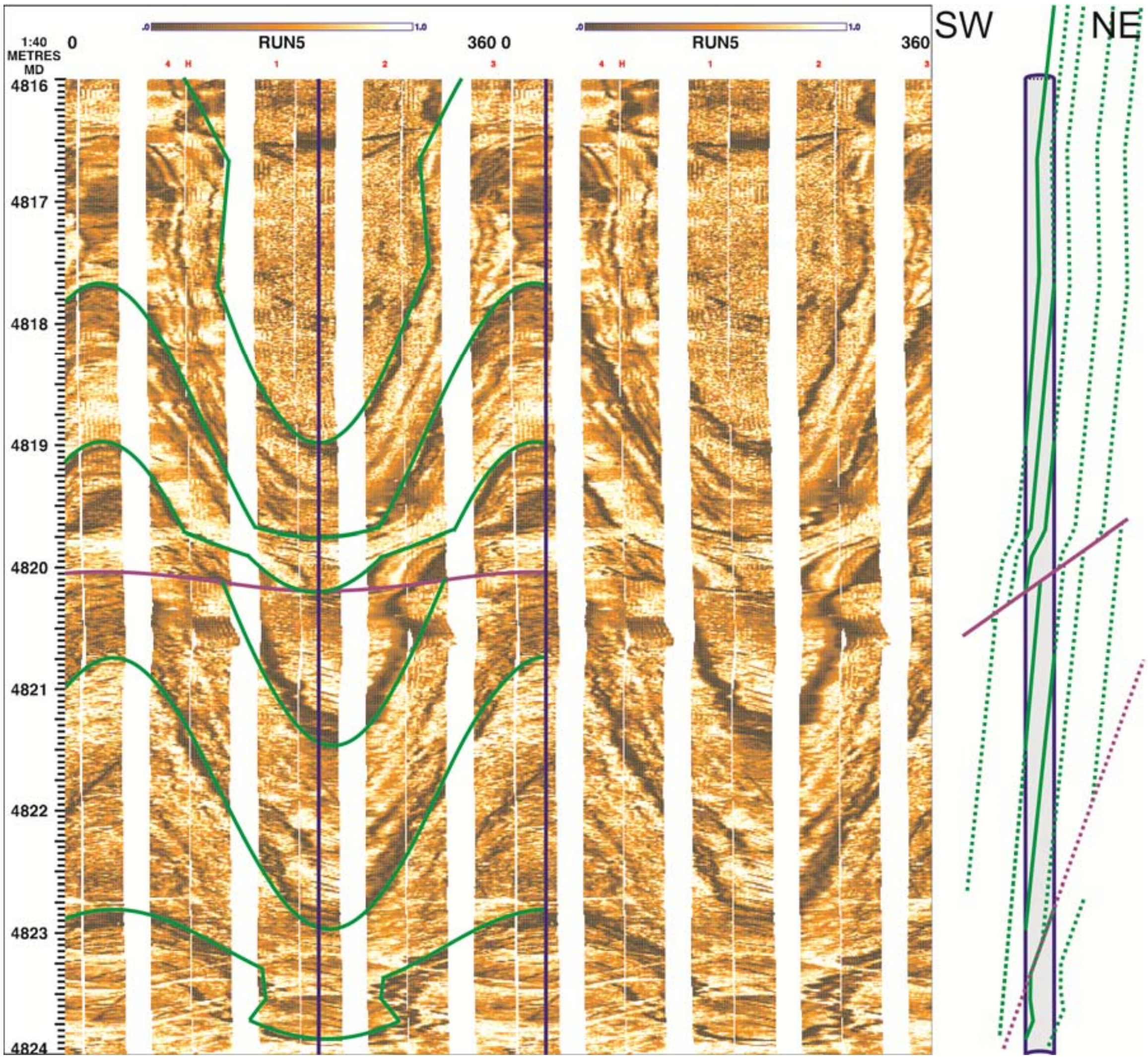

Figure 3-15: Borehole image 4816-4824 metres (N)

The final image example shows steeply dipping bedding cut by one clear fault plane at 4820 metres. The fault plane is conductive, implying that it has open aperture and the bedding gently folds in and out of the borehole in a way that is commonly seen in horizontal wells as they cross tear faults. The fold (and inferred fault structure) at the bottom of the interval is interesting because the fold vergence looks to be counterclockwise, meaning it most likely occurred as a backthrust before the bedding was rotated into this vertical position.

can be drawn in cross-sectional views so that their structural implications can be fully understood.

Three of the image intervals (Figures 3-9, 3-10 and 3-13) show cleavage planes due to low-grade metamorphism. A schematic drawing (Figure 3-16) of the wellbore in plan view is shown to help visualize the cleavage planes and drilling induced fractures.

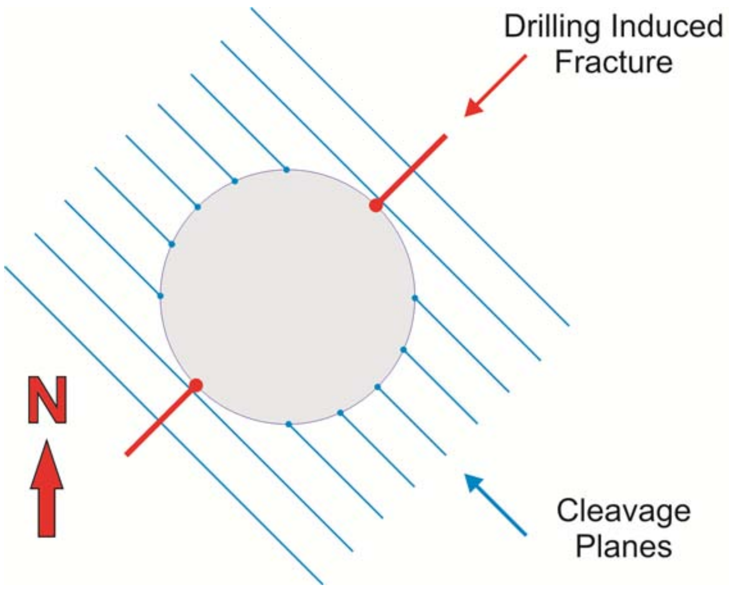

Figure 3-16: Plan view schematic of a well with cleavage and hydraulic fractures
A vertical wellbore (shown by the grey shaded circle in this plan view) preferentially intersects vertical cleavage planes (the blue lines) on the NW and SE sides of the borehole, and tends to miss them on the NE and SW sides, leading to the sampling bias seen in Figures 3-9 and 3-10. Drilling-induced hydraulic fractures (marked in red) propagate parallel to the maximum horizontal stress direction (NE-SW).

Borehole image mesoscopic data

The bedding data for each of the borehole image examples were plotted in stereonets (Figures 3-17 and 3-18), as were grouped sets of three examples (to achieve n>30), the total mesoscopic data set and the megascopic data from the dipmeter. They are listed below in Table 3-1 and will be discussed in Chapter 4.

Table 3-1: Borehole fold orientations

Measured Depth (metres)	n	Stereonet Name (Figures 3-17 and 3-18)	Trend (Degrees)	Plunge (Degrees)	K	C
2858-2861	8	A	286.7	28.3	0.46	3.89
3031-3035	12	B	303.1	3.1	0.04	6.67
3081-3085	12	C	310.6	12.5	0.17	5.10
A-C combined	32	A-C	301.1	11.0	0.13	3.24
3237-3241	8	D	286.3	6.3	1.22	2.24
3481.5-3484.5	13	E	156.0	6.4	0.44	5.41
3637.5-3640.5	11	F	281.0	20.8	1.42	5.37
D-F combined	32	D-F	297.0	6.5	1.00	2.80
3702-3704	11	G	146.8	4.5	0.72	5.52
4228-4230	13	H	314.9	8.1	0.76	6.19
4244-4246	13	I	319.8	6.4	0.45	6.75
G-I combined	37	G-I	316.3	5.9	0.65	5.08
4563-4566	12	J	311.5	9.3	0.66	6.62
4670-4675	9	K	307.9	17.7	0.45	6.43
4730-4745	12	L	121.0	6.3	1.13	4.33
J-L combined	33	J-L	304.3	11.9	0.30	4.11
4806-4812	23	M	311.8	13.7	0.49	5.02
4816-4824	13	N	306.0	8.2	11.12	4.34
M-N combined	36	M-N	309.4	12.7	0.88	12.72
All mesoscopic data	170	A-N	305.7	7.7	0.20	3.31
All dipmeter data	3828	O	303.7	10.8	0.93	4.02

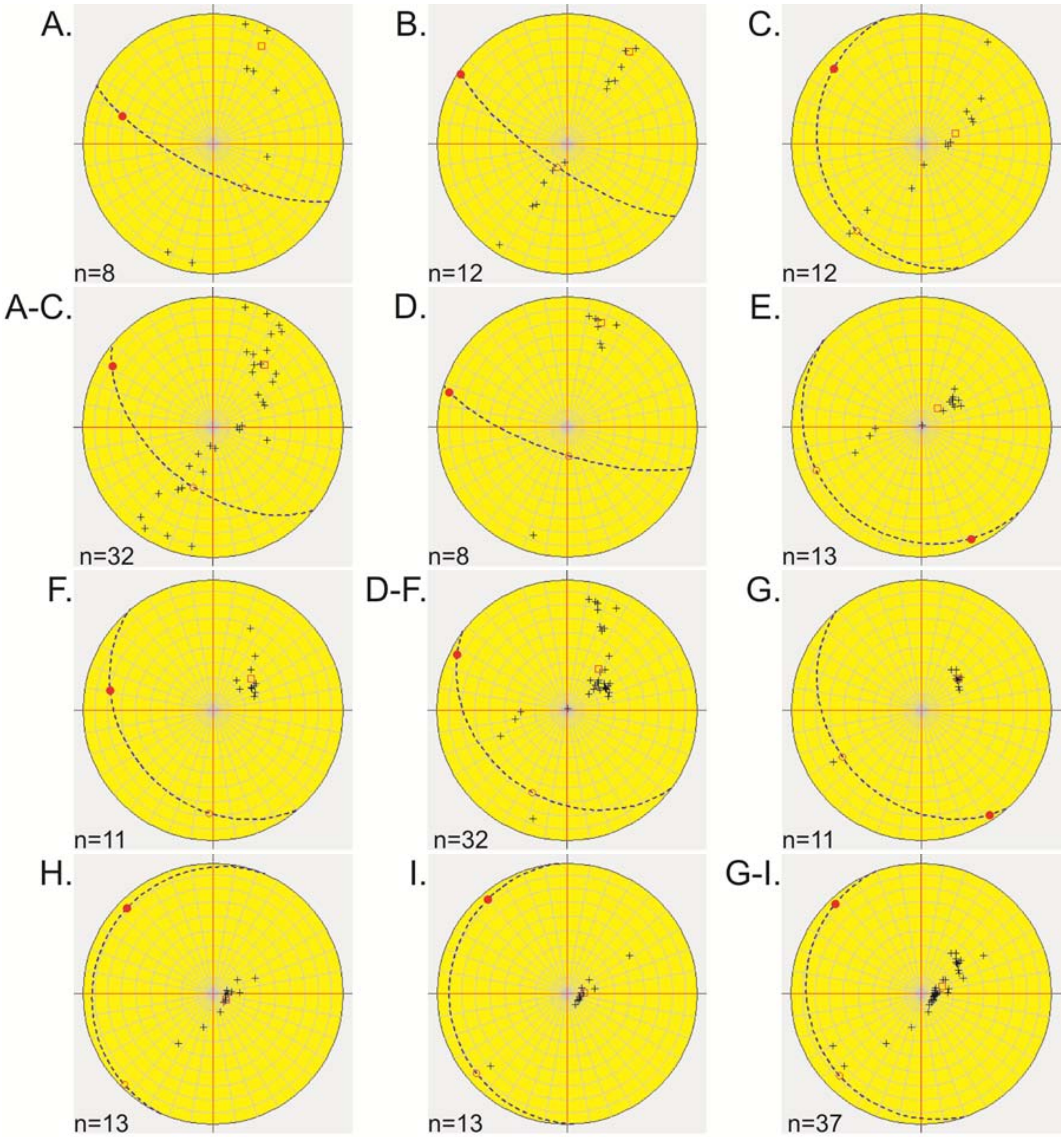

Figure 3-17: Borehole image stereonets

Poles to bedding are marked with black crosses in these lower hemisphere stereonets. The red dot indicates the third eigenvector-calculated fold axis and the dashed black line is the trace of the plane perpendicular to the first eigenvector. The stereonet numbers correspond to the depth ranges tabulated in Table 3-1 and represent either individual mesoscopic structures (Stereonets A, B, C, D, E, F, G, H, I) or the summation of adjacent structural measurements (Stereonets A-C, D-F, G-I).

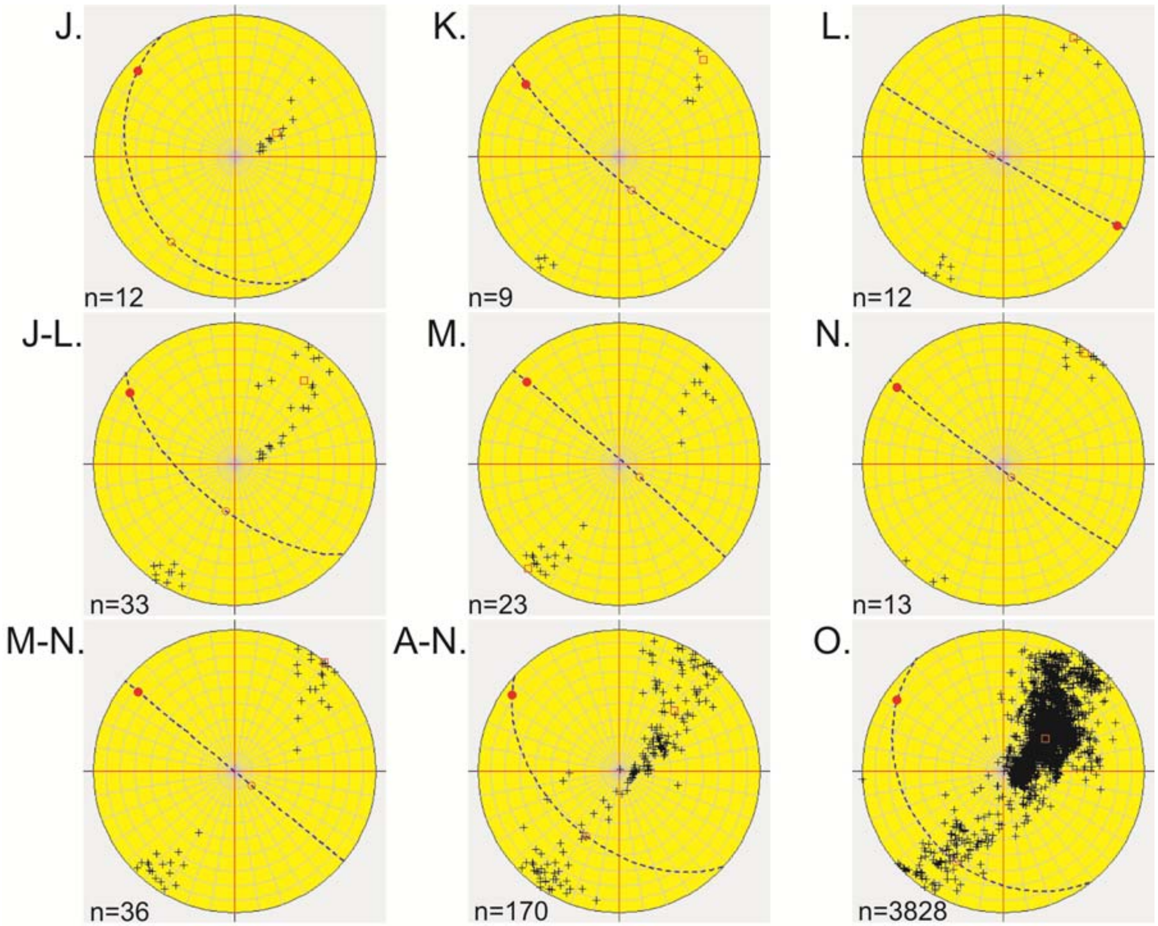

Figure 3-18: Borehole image stereonets (continued)
Poles to bedding are marked with black crosses in these lower hemisphere stereonets. The red dot indicates the third eigenvector-calculated fold axis and the dashed black line is the trace of the plane perpendicular to the first eigenvector. The stereonet numbers correspond to the depth ranges tabulated in Table 3-1 and represent either individual mesoscopic structures (Stereonets J, K, L, M, N), the summation of adjacent structure measurements (Stereonets J-L, M-N), the summation of all the mesoscopic scale measurements (Stereonets A-N) or the megascopic dipmeter data (Stereonet O).

CHAPTER 4: ON SCALE, GEOMETRY AND FRACTAL GEOLOGY

This research sought to probe a number of questions about how a geologist should best quantify and project mesoscopic structures as observed in field outcroppings and in the unrolled-cylinder view of a borehole image log. Methods were developed to transform mesoscopic structural measurements taken in one frame of reference (3-dimensional outcrop measurements) and project them to another (the sinusoidal unrolled-cylinder), and to do the inverse, taking borehole image log data and drawing to-scale cross-sections. The cross-sections drawn from image log data proved to be quite instructive because one can make detailed conclusions about valuable information like fold vergence, structural history and fault types of mesoscopic structures that otherwise would remain a mystery.

By carefully measuring a variety of structures in outcrop and in subsurface borehole image logs, I accumulated a reference database that relates the well-understood geometries of the quasi-planar outcrop surface, the projected and logical reference of the down-plunge projected cross-section to the somewhat alien world of the sinusoidal views of a cylindrical borehole. It is clear that by comparing this study's borehole-structure intersections (both from the subsurface and synthetic image logs derived from outcrop measurements) and their accompanying cross-sections that there is no difference between the scale or style of structures that are measurable in subsurface image logs and in outcrop.

For example, Elbow Falls Synthetic Borehole #1 (Figure 2-6 A) and the borehole image log segment from 3031-3035 metres (Figure 3-3) both show fold intersections where the borehole is nearly perpendicular to the fold hinge plane. Elbow Falls Borehole #2 (Figure 2-6 B) and the image log segment 4670-4675 metres (Figure 3-12) both feature intersections where the hinge plane is oblique to the borehole and thus one limb is intersected at a higher angle than the other (making for longer sinusoids on one side of the hinge "circle"). Cascade Borehole #2 (Figure 2-13 B) encounters undulating bedding in a larger fold structure as is seen in the image log segment from 4806-4813 metres (Figure 3-14). Elbow Falls Borehole #4 (Figure 2-6 D) is a fold that is a result of shearing between parallel bedding surfaces, just as are the image log segments at 3237-3241 metres (Figure 3-6), 3702-3704 metres (Figure 3-8), 4228-4230 metres (Figure 3-9) and 4244-4246 metres (Figure 3-10). Fault-bend-fold structures are seen in several of the outcrop locations including Canmore Borehole #4 (Figure 2-21 D) and #5 (Figure 2-22 E), with similar subsurface examples seen at 3481.5-3404.5 metres (Figure 3-7) and 3637.5-3440.5 metres (Figure 3-5).

Using the Dale-Pumpelly Principle in petroleum exploration

My original reason for pursuing this study was to see if the Dale-Pumpelly Principle could be used to help exploration geologists in situations where a pilot or intermediate wellbore intersected just one limb of a structure whose fold axis plunge direction and magnitude was unknown. (Knowing the plunge orientation is essential to planning horizontal wells that are usually drilled in back-limb or crestal positions, sub-parallel to the fold axis in order to make it easier to have the borehole stay within the best reservoir section by avoiding the less-fractured far back-limb or the structurally very complex fore-limb.) In the case where only one fold limb is intersected, the dipmeter or borehole image data plots as a cluster of points rather than as a girdle and I hoped that if one could somehow measure a mesoscopic structure or two (such as a small fault-bend fold or a bed-shear fold), that they would produce a meaningful prediction of the megascopic structural fold axis.

Apart from understanding the quirks of geometric reference surfaces, the structural analysis in this study served to accumulate a sizeable number of comparisons between discrete mesoscopic structures and their megascopic contexts so I could answer my original question. There were 14 borehole image segments and 10 outcrop structural domains investigated so a total of 24 comparisons between individual mesoscopic structures and megascopic structural context can be made. Further, by grouping all of the domains measured at a given outcrop together and by grouping consecutive borehole image segments into sets of at least three fold structures, an additional eight comparisons between mesoscopic structure groups and megascopic structures can be made.

Normally when comparing 3-D orientation data, the mathematically correct method is to use the 3-D minimum vector angle as a basis of comparison because there are issues of whether a difference of dip inclination is as significant as a difference in dip azimuth. This is not the case when dealing with the shallowly plunging folds or domal structures that make for viable petroleum traps (the context in which this study's questions are posed). In a shallowly-plunging fold structure, a 10 degree change in the plunge magnitude is approximately the same vector difference as a 10 degree change in the axial trend, making it seem that these two vector parameters can be treated separately.

Because all of the megascopic structures in this study have fold axes that are modestly plunging (less than 10 degrees), both the plunge and the trend measurements are significant numbers. Further, because horizontal wells are usually drilled parallel to strike and are steered in left-right and up-down direction axes that are equivalent to changes in the fold axis trend and plunge, it is appropriate to keep to those conventions when comparing the difference between mesoscopic and megascopic structures for an industrial application.

This comparison is done below in Table 4-1 for the outcrop data and Table 4-2 for the borehole data. The two tables show the absolute value of the difference in the structural trend direction (ΔTrend) and the difference in the plunge magnitude (ΔPlunge) between the mesoscopic fold axis and the megascopic fold axis. Negative plunge values indicate that the mesoscopic trend direction was opposite to the megascopic trend (i.e. plunging NW when the megascopic plunge is towards the SE). To test the sensitivity to statistical scatter, average ΔTrend and ΔPlunge were computed using just those stations whose individual statistical values indicated minimum scatter ($C>3$) and girdles rather than clusters ($K>1$); the average ΔTrend and ΔPlunge for combined structures that had more than 30 measurements ($n>30$) were also computed.

Following the tables, the individual borehole data fold axis measurements are graphically plotted on a stereonet as red dots, with the megascopic fold axis derived from all the dipmeter data plotted as the green dot (Figure 4-1A). The second stereonet (Figure 4-1B) has the grouped image segments (A-C combined, D-F combined, etc,) plotted as red dots, the average result from all of the mesoscopic data plotted as the blue dot and the megascopic fold axis plotted as the green dot.

Table 4-1: Mesoscopic-megascopic comparison for outcrop data

Location	n	Stereonet Figure Number	ΔTrend (Degrees)	ΔPlunge (Degrees)
Elbow Falls, Station 1	13	2-2, A	9.6	8.8
Elbow Falls, Station 2	12	2-2, B	11.3	2.3
Elbow Falls, Station 3	9	2-2, C	5.4	4.3
Elbow Falls, All	34	2-2, D	8.9	3.4
Powderface, Station 1	6	2-8, A	15.2	0.2
Powderface, Station 2	3	2-8, B	8.0	2.8
Powderface, All	9	2-8, C	9.3	0.3
Cascade (without SE dip)	8	2-11, A	44.3	7.6
Canmore, Station 1	11	2-16, A	6.0	11.9
Canmore, Station 2	26	2-16, B	12.2	10.3
Canmore, Station 3	30	2-16, C	1.3	-13.8
Canmore, Station 4	15	2-16, D	4.3	6.0
Canmore, All	81	2-16, E	2.2	1.2
Average difference for individual structures:			12.3	8.0
Avg. difference for individual structures K<1, C>3			7.2	8.2
Average difference for combined sets of structures:			6.8	1.6
Average difference for combined sets where n>30			5.6	2.3

Table 4-2: Mesoscopic-megascopic comparison for borehole data

Measured Depth	n	Stereonet Number (Figure 3-16)	ΔTrend (Degrees)	ΔPlunge (Degrees)
2858-2861	8	A	17.0	17.5
3031-3035	12	B	0.6	7.7
3081-3085	12	C	6.9	1.7
A-C combined	32	A-C	2.6	0.2
3237-3241	8	D	17.4	4.5
3481.5-3484.5	13	E	32.3	-17.2
3637.5-3640.5	11	F	22.7	10
D-F combined	32	D-F	6.7	4.3
3702-3704	111	G	23.1	-15.3
4228-4230	13	H	11.2	2.7
4244-4246	13	I	16.1	4.4
G-I combined	37	G-I	12.6	4.9
4563-4566	12	J	7.8	1.5
4670-4675	9	K	4.2	6.9
4730-4745	12	L	2.7	-17.1
J-L combined	33	J-L	0.6	1.1
4806-4812	23	M	8.1	2.9
4816-4824	13	N	2.3	2.6
M-N combined	36	M-N	5.7	1.9
All mesoscopic data	170	A-N	2.0	3.1
Average difference for individual structures:			12.3	8
Average difference for combined sets of structures:			5.6	2.5
Average difference for individual structures with K<1, C>3			12.7	8.8
Average difference for combined sets with K<1, C>3			5.4	2.0

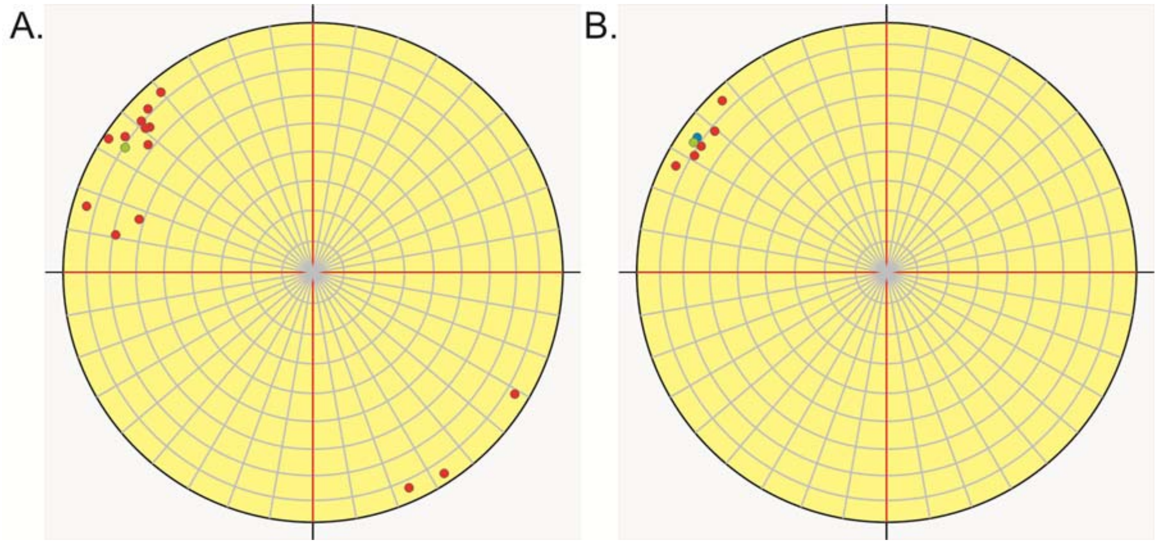

Figure 4-1: Borehole mesoscopic structure summary stereonets
Stereonet A (lower hemisphere) shows the calculated fold axes for the individual borehole image segments plotted as red dots compared to the megascopic fold axis (green dot) calculated from the dipmeter data. Stereonet B shows the grouped borehole image fold axes plotted as red dots and the total fold axis from all mesoscopic structures plotted as the dark blue dot compared to the megascopic fold axis plotted as the green dot.

The ΔTrend and ΔPlunge results could be considered to be a measure of the error that one would expect if one were to use an individual mesoscopic structure to predict the associated megascopic structure. Because these "errors" are similar in magnitude for the borehole and for the outcrop measurements (and because the scales and morphologies are also similar), all 24 individual fold axis observations are combined into a single data set to compute an average "error" value. The average error in structural strike direction (ΔTrend) as predicted by a single mesoscopic structure is +/-12.1 degrees with a standard deviation of 10.4 degrees and the average error in plunge is +/-7.4 degrees with a standard deviation of 9.2 degrees. By averaging just those individual structures that had $C<1$ and $K>3$, the average error in trend direction is +/- 10.4 degrees with a standard deviation of 8.1 degrees and the average error in plunge magnitude is 8.5 degrees with a standard deviation of 5.3 degrees. There is not a large difference between the individual structure results with or without C and K values that indicate a strong girdle.

This magnitude of prediction error means that in petroleum exploration applications, a single mesoscopic event could be used fairly reliably to predict the megascopic structural trend. Unfortunately, megascopic structural trend directions are almost always known in advance through well control, parallel seismic dip lines and geologic surface maps, so this prediction does not help much. The plunge magnitude (and exact direction) is of much greater interest but a single-feature error of +/-7.4 degrees is much too large to use to steer a (multi) million dollar horizontal well.

The comparison between grouped measurements (all the domains at a given outcrop location and adjacent sets of at least three mesoscopic structures in a borehole image log) is much more favourable for a drilling application. The average error in structural strike direction (ΔTrend) as predicted by the eight groups of mesoscopic structures is +/-6.1 degrees with a standard deviation of 4.1 degrees and the average error in plunge was +/-2.1 degrees with a standard deviation of 1.8 degrees. By averaging just those grouped measurements that have $C<1$ and $K>3$, the average error in trend direction is +/- 5.4 degrees with a standard deviation of 4.5 degrees and the average error in plunge magnitude is +/-2.1 degrees with a standard deviation of 1.7 degrees, a marginal improvement.

My conclusion from seeing this magnitude of dispersion in individual mesoscopic structures is that they must be arranged in sets similar to how megascopic structures are arranged, that is in en échelon arrangements where regional structural compression magnitude remains stable across a deformation belt but where that compression is taken up locally by structures that vary in three dimensions between folds that plunge in opposite directions and by faults that die out along strike.

In megascopic Foothills structures, folds are typically at least 10 times longer along strike than they are wide (in terms of fold wavelength). It is reasonable to assume that mesoscopic structures would tend to have similar proportions but where a megascopic fold might be 1 km wide by 10 km long, the mesoscopic fold would be 1 m wide by 10 m long or likely smaller because at a smaller scale, beds can deform in a more ductile manner than they do at larger scales. This would mean that the likelihood of encountering transition zones (i.e. non-cylindrical structures with changing plunge magnitudes along strike) in a 10 m wide set of folds with opposing and alternating plunges in an outcrop (like the Canmore outcrop) would be at least as likely as encountering transition zones along any arbitrary 10 km line in a fold and thrust belt, so quite likely. This variability also occurs along strike so the dispersion in fold axes seen in the mesoscopic structures can be considered to be an analogue for the variability in the megascopic trend that would be expected in a horizontal well.

Sedimentological implications

While this study focused exclusively on structures generated in a compressional structural setting, the method for analysing mesoscopic folds in borehole image logs could just as easily be used in analyzing soft sedimentary slump structures. The folds and shear displacements that result from soft sedimentary deformation are of a similar scale as the structures studied here so cross-sections could be drawn to determine vergence direction and stereonets could be generated to determine the fold axes. This information could be used to infer the transport direction as these structures form in a down-slope direction.

Fractal structural geology

After completing this study and concluding that mesoscopic faults typically splay into mesoscopic folds, and that mesoscopic folds typically plunge in both directions transferring deformation laterally on a mesoscopic scale, I would add to the Dale-Pumpelly Principle by saying that the sets of geometries are fractal not just in two dimensions (i.e. lower order fold axes are similar to higher order ones), but are volumetrically fractal in three dimensions where mesoscopic structures can and must display at least as much variance as megascopic structures show, on a scale proportionally relative to fold amplitudes and fault throw magnitude.

Summary

The key novel results of this study are:

- The development of a repeatable method to translate cross-section data into a synthetic borehole image.
- The development of a method to convert a borehole image log to a cross-section, revealing important details like the vergence direction of mesoscopic folds and faults.
- The production of a catalogue of mesoscopic structures in real and synthetic borehole images to help visualize these complex structures in the strange cylindrical geometry of the borehole.
- A careful test of the Dale-Pumpelly Principle, confirming the correlation between mesoscopic and megascopic structures while outlining the statistical sensitivity in predicting megascopic trends from mesoscopic data.
- An understanding of the magnitude of the variation in mesoscopic structures leading to the idea that the fractal nature of geologic structures occurs in a three-dimensional sense instead of the two-dimensional sense inferred in standard presentations of the Dale-Pumpelly Principle.

References

Alekseyev, V.B., 1989, Accuracy of the Dale-Pumpelly principle in light of discoveries of folds shaped like tongues, Doklady Akademii Nauk SSSR, 305; 6, p. 1430–1432.

Barton, C., Moos, D., Peska, P, Zoback, M.D., 1997, Utilizing wellbore image data to determine the complete stress tensor: application to permeability anisotropy and wellbore stability, The Log Analyst, November-December 1997, p. 21–33.

Beach, H. H., 1942a, Bragg Creek Alberta, 1:63360 Scale, Geological Survey of Canada, Map 654a.

Beach, H. H., 1942b, Map Moose Mountain Alberta, 1:63360 Scale, Geological Survey of Canada, Map 688a.

Borehole Image Data presented in this study are available as paper prints from the British Columbia Ministry of Energy, Mines and Petroleum Resources upon request and the megascopic dip data can be digitized from that print or are available for sale from www.hef.com.

British Columbia, Canada.svg, From Wikipedia Commons (http://commons.wikimedia.org/wiki/File:British_Columbia,_Canada.svg).

Cant, D.J., Stockmal, G.S., 1997, A field guide to portions of the Jurassic Fernie-Kootenay Trans-Canada Highway section, Banff, Alberta: new sedimentological and structural observations and interpretations, Bulletin of Canadian Petroleum Geology; 47; 1, p. 1-18.

Cant, D.J., Stockmal, G.S., 2000, Reply to Discussion - A field guide to portions of the Jurassic Fernie-Kootenay Trans-Canada Highway section, Banff, Alberta: new sedimentological and structural observations and interpretations, Bulletin of Canadian Petroleum Geology; 48; 1, p. 90-93.

Cheung, P.S., 1999, Microresistivity and ultrasonic imagers: tool operations and processing principles with reference to commonly encountered image artifacts, Borehole Imaging: Applications and Case Histories, Geological Society, London, Special Publications, 159, p. 45–57.

Ekstrom, M.P., Dahan, C.A., Chen, M., Lloyd, P.M., Rossi, D.J., 1986, Formation imaging with microelectrical scanning arrays, SPWLA 27th Annual Logging Symposium, June 16-19, 1986.

Fam, M.Y., Haugland, M. Chemali, R., Seiler, D., Stewart, W.F., 1996, Integrating imaging logs in formation evaluation, SPWLA 37th Annual Logging Symposium, June 16-19, 1996.

fractal. (2010). In Merriam-Webster Online Dictionary. Accessed May 8, 2010, from http://www.merriam-webster.com/dictionary/fractal.

Hamblin, A.P., Walker, R.G., 2000, Discussion - A field guide to portions of the Jurassic Fernie-Kootenay Trans-Canada Highway section, Banff, Alberta: new sedimentological and structural observations and interpretations, Bulletin of Canadian Petroleum Geology; 48; 1, p. 84-89.

Lofts, J.C., Bedford, J., Boulton, H., Van Doorn, J.A., Jeffreys, P., 1997, Feature recognition and the interpretation of images acquired from horizontal wellbores, *in* Borehole Imaging: Applications and Case Histories, Geological Society, London, Special Publications, 159, p. 345–365.

Lofts, J.C., Bourke, L.T., 1999, The recognition of artefacts (sic) from acoustic and resistivity borehole imaging devices, *in* Borehole Imaging: Applications and Case Histories, Geological Society, London, Special Publications, 159, p. 59–76.

Lovell, M.A., Harvey, P.K., Williams, C.G., Jackson, P.D., Flint, R.C., Gunn, D.A., 1997, Electrical resistivity core imaging: A Petrophysical link to borehole images, The Log Analyst, November-December 1997, p. 45–53.

Mandelbrot, B, 1977, Fractals: Form, Chance and Dimension; W H Freeman and Co, 365 pp.

Prensky, S.E., 1999, Advances in borehole imaging technology and applications, *in* Borehole Imaging: Applications and Case Histories, Geological Society, London, Special Publications, 159, p. 1–43.

Price, R. A., Mountjoy, E.W., 1970, Geology Canmore Alberta (West Half), 1:50000 Scale, Geological Survey of Canada, Map 1266a.

Price, R. A., Mountjoy, E.W., 1972, Geology Banff Alberta (East Half), 1:50000 Scale, Geological Survey of Canada, Map 1294a.

Pumpelly, R., Wolff, J.E. Dale T.N., 1894, Geology of the Green Mountains of Massachusetts, *in* Monographs of the United States Geological Survey, Volume 23, p. 125-202.

Schlumberger, 1986, Dipmeter Interpretation; Fundamentals Series, 76 pp.

Trice, R., 1999, A methodology for applying a non unique, morphological classification to sine wave events picked from borehole image log data, *in* Borehole Imaging:

Applications and Case Histories, Geological Society, London, Special Publications, 159, p. 77–90.

Weller, G., el-Halawani, T., Tribe, I., Webb, K., Stoller, C., Galvin, S., Scott, G., 2005, A new integrated LWD platform delivers improved drilling, well placement, and formation evaluation services, *in* Offshore Europe, 6-9 September 2005, SPE Paper 96652-MS, p. 1-11

Woodcock, N.H., Naylor, M.A., 1983, Randomness testing in three-dimensional orientation data, Journal of Structural Geology, 5, 5, p. 539-548.

Zemanek, J., Glenn, E.E., Norton, L.J., Caldwell, R.L., 1970, Formation evaluation by inspection with the borehole televiewer, Geophysics, 35, 2, p. 254–269.